Dottorato di Ricerca in Neuroscienze
Curriculum Neuroscienze e Neurotecnologie
Ciclo XXXII

Coordinatore Prof. Angelo Schenone

Extended field-of-view ultrathin microendoscopes with built-in aberration correction for high-resolution functional imaging with minimal invasiveness

Autore: **Andrea Sattin**

Supervisor: **Tommaso Fellin**

The highest happiness of man
is to have probed what is knowable
and quietly to revere what is unknowable

Johann Wolfgang von Goethe

Contents

List of Figures

List of abbreviations

2P	two-photon
AA	adeno-associated
AAV	adeno-associated viral vector
AO	adaptive optics
AP	action potential
Arch	archeorhodopsin
BR	bacteriorhodopsin
CA	cornu ammonis
Cdf	calcium-delta fluorescence
CGH	computer-generated holography
ChR	channelrhodopsin
CMOS	complementary metal-oxide semiconductor
CNS	central nervous system
cpGFP	circularly permuted green fluorescent protein
CT	corticothalamic
DM	deformable mirror
dmVPM	dorsomedial part of the VPM
DMD	digital micromirror devices
DNA	deoxyribonucleic acid
EEG	electroencephalogram
eFOV	enlarged field of view
e.g.	exempli gratia, meaning "for example"
eGFP	enhanced green fluorescent protein
EMG	electromyogram
et al.	et alii, meaning “and others”
fMRI	functional magnetic resonance imaging
FOV	field of view
FWHM	full width at half maximum
GDD	group delay dispersion
GECI	genetically encoded calcium indicator
GFP	green fluorescent protein
GMM	Gaussian mixture model
GRIN	gradient index
GUI	graphical user interface

Halo	halorhodopsin
KAUST	King Abdullah University of Science and Technology
ICA	independent component analysis
LIV	layer IV of the neocortex. Analogous abbreviations are used for other layers (LV, LVI)
LA	longitudinal aberration
LDA	linear discriminant analysis
LFP	local field potential
LSM	laser scanning microscopy
M1	primary motor area of the neocortex
NA	numerical aperture
NIR	near infrared radiation
NMF	non-negative matrix factorization
NOA	Norland optical adhesive
NpHR	halorhodopsin
OPD	optical path difference
PBS	phosphate-buffered saline
PCA	principal component analysis
PDMS	polydimethylsiloxane
PMT	photomultiplier tube
POm	posterior medial nucleus of the thalamus
PSF	point spread function
PrV	principal trigeminal nucleus in the brainstem trigeminal complex
P-V	peak to valley
RF	receptive field
ROI	region of interest
RTN	reticular thalamic nucleus
SEM	scanning electron microscope
SH	Shack Hartmann
SLM	spatial light modulator
SNR	signal to noise ratio
SpV	spinal trigeminal nucleus in the brainstem trigeminal complex
std	standard deviation
SVM	support vector machine
TA	transverse aberration
TC	thalamocortical
TPE	two-photon excitation

TPP	two-photon photopolimerization
UV	ultraviolet
VIS	visible radiation
vlVPM	ventrolateral part of the VPM
VPM	ventral posterior medial nucleus of the thalamus
WMI	whisking modulation index
wS1	primary whisker somatosensory area of the neocortex
wS2	secondary whisker somatosensory area of the neocortex

1 Introduction

Understanding how behavior or cognitive states stem from brain activity is one of the main challenges in current neuroscience. Indeed, many experimental and theoretical efforts in the field are directed to reveal how sensory perception, motor schemes, and memories emerge from the coordinated activity of neurons.

Neurons form an intricate network within the brain. Both their anatomical organization and their activity are believed to underlie the computations that enable living beings to perceive, act, learn, and remember [1]–[3]. Neural circuits have been proposed as functional building blocks of the brain [4]. In this framework, it is important to investigate how spatio-temporal activity patterns in neuronal circuits control brain function and behavior [5]–[9]. The first step to address this question is to efficiently record neuronal activity with high spatial and temporal resolution over large field-of-view. Moreover, recordings of neuronal activity should be performed in living organisms (*in vivo*) to correlate neural activation with specific brain functions, limiting as much as possible damage to neuronal tissue. This is however a challenging task. Neurons generate fast (on the millisecond time scale) electrical signals (action potentials, APs) that are propagated along neural processes to reach many other neuronal cells. Moreover, the mammalian brain is composed of billions of neurons and the smallest sensory stimulus evokes responses in tens of thousands of neurons. Thus, a preferred technique for efficiently measure neuronal circuit activity should be minimally invasive, allow the monitoring of large regions of brain tissue, and achieve high spatial and temporal resolution.

Because of its high temporal resolution, high signal-to-noise ratio, and the ability to measure neuronal activity over many temporal scales (from single APs to network oscillations [10]), electrophysiology has been (and still is) considered a preferred technique for investigating the brain. For decades, intracellular [11] and extracellular electrical measurements have been the prevalent recording method in systems neuroscience [12]. However, despite tremendous improvements in the fabrication of multielectrode arrays, in terms of sampling density and biocompatibility, electrophysiological approaches suffer from various limitations, such as the lack of genetic cell specificity, the limited structure-function correlation [13], and a general bias, in unit recordings, towards sorting cells with high-frequency spiking.

Alternative approaches have been introduced in the last decades. For example, imaging techniques, such as fMRI, had great impact in neuroscience, allowing the investigation of spatially distributed neuronal circuits which are involved in response to external stimuli, under normal and pathological conditions [14]–[16]. However, fMRI has limited temporal resolution and cannot register brain dynamics at cellular or subcellular level. To this aim, the development of optical imaging methods based on nonlinear excitation (namely *two-photon fluorescence functional imaging*) and the engineering of fluorescent activity reporters (fluorescent calcium indicators) have provided a tremendous boost to the study of the cellular determinants of brain function, thanks to the high spatial resolution of these non-linear approaches [17]–[21].

1.1 Two-photon fluorescence functional imaging of neural activity

1.1.1 Fluorescence and multiphoton excitation

Fluorescence is the spontaneous emission of one photon by a molecule (called a fluorophore) during its relaxation from an excited state to the ground state and fluorescence microscopy, that relies on the detection of light emitted by fluorophores, is one of the most popular imaging techniques in neuroscience, because it allows the generation of high contrast images.

A molecule can only take discrete values of energy (called energy levels) that are determined both by potential and kinetic components. Indeed molecular energy can be stored in a variety of ways including electronic, vibrational, rotational and translational energy, that respectively refer to the potential energy stored in the electronic charge configuration, and the kinetic energy associated either with the motion of atoms within the molecule or with the rotation and motion of the molecule itself. Various electronic configurations can be achieved and each one is compatible with different vibrational oscillations, with the result that many possible discrete molecular excited states can be classified, each characterized by a specific probability of relaxing toward other lower energy levels (usually expressed as rates k, measured in s^{-1}) and hence a lifetime (τ, that describe the average time spent in the particular excited state). Jablonski diagrams are graphical representations illustrating the molecular energy levels as well as the transitions between them, and an example is reported in Fig. 1A. The ground state (S_0) is the lowest-energy level and corresponds to a vibrationally relaxed molecule with a stable spatial distribution of the electronic charge. However this condition can be altered by the absorption of a photon (a process that is extremely rapid, in the order of one femtosecond, 10^{-15} s), that brings the molecule into a higher-energy level, characterized by a displacement of electrons and some vibrational energy. Nevertheless, after photon absorption, vibrational energy is quickly dispersed through radiationless mechanisms, such as vibrational

relaxation and internal conversion (taking place in about one picosecond, 10^{-12} s), that bring the molecule at the lowest vibrational level of the excited electronic state.

The excited electronic states meaningful in the context of fluorescence are those closer to S_0, namely S_1 and T_0, as represented in Fig. 1A. S_1 is a singlet state that can decay to the ground state S_0 either by the emission of one photon (*fluorescence*, $\tau \approx 10^{-10}–10^{-7}$ s) or via non-radiative processes. From S_1, the molecule can also make a transition, called intersystem crossing, to T_0, the lowest triplet state and in this case, relaxation from T_0 to S_0 also produces one photon, but it takes much longer (*phosphorescence*, $\tau \approx 10^{-6}–10^{4}$ s). The quantum efficiency (yield) of a fluorophore is defined as the probability of emitting a fluorescence photon after the excitation into S_1. Note that relaxation transitions, like those happening during excitation, usually end up in vibrationally excited states that rapidly relax to the lowest vibrational level of the electronic state.

Once back in the ground state, the molecule can absorb another photon, reach the excited state S_1, and restart the excitation-relaxation cycle. Fluorophores potentially could undergo infinite fluorescence cycles, but in fact they have limited stability, indeed in each cycle, there is the possibility that they reach a dark state. For example, photobleaching is an irreversible process that brings a fluorophore into a non-fluorescent state. This phenomenon has been attributed to transitions from excited states (S_1 or T_0) to higher energy levels due to the absorption of a second photon; given the longer lifetimes characterizing the triplet state, photobleaching from T_0 rather than S_1 is more probable [22]. Photobleaching can be reduced by controlling the light source used for excitation or by the introduction of triplet-state quenchers [23].

The energy of photons absorbed or emitted by fluorophores equals the gap between the molecular energy levels involved in the transitions. Therefore, given that each molecule has particular energy levels, fluorophores are characterized by specific fluorescence excitation and emission spectra, that report the absorbed or emitted light intensity as a function of photon energy and, once normalized, represent probability densities of the excitation and emission processes to occur. In the description above, only electronic and vibrational energies were taken into account. However, the energy gaps between different vibrational levels, are in fact populated by different rotational and translational molecular states (see Fig. 1A). Therefore when considering also rotational and translational energy levels for an ensemble of molecules at room temperature, the results are spectra that are continuous over a broad range of energies rather than sharp lines. Depicted, for example, in Fig. 1B are the spectra of enhanced Green Fluorescent Protein (eGFP), one of the most used fluorophores in molecular biology. Note that often excitation spectra show a shoulder at shorter wavelengths with respect to the peak (see Fig. 1B), due to transitions to energy states higher than S_1.

Because of vibrational energy losses happening while the molecule is in the excited state, emitted photons have a reduced energy compared to the absorbed ones, hence emission spectra are shifted toward longer wavelengths relative to absorption spectra: this phenomenon is called Stokes shift

and it is fundamental for microscopy applications. Indeed, in fluorescence microscopy, fluorescent dyes are used to label specific structures in the sample, which is then illuminated by light in the absorption spectrum of the fluorophore. Emitted fluorescence photons are collected and images are generated by taking advantage of the Stokes shift, which allows, through the use of a dichroic mirror and chromatic filters, the separation of the emitted photons from contamination of reflected excitation light and spectrally separated autofluorescence. In this way, fluorescence light can be selectively guided to the detector (Fig. 1C) to be measured.

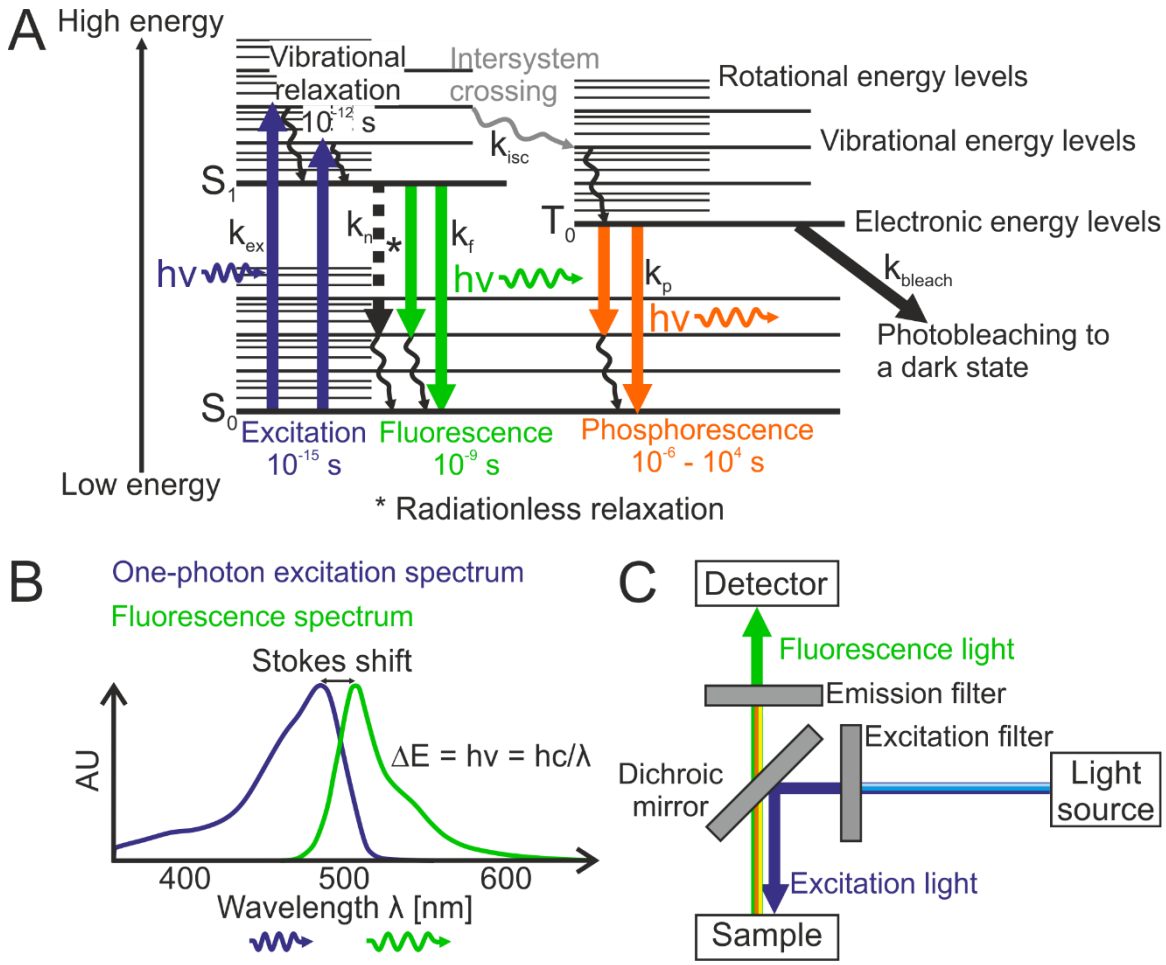

Fig. 1: Fluorescence

A) Jablonski diagram with transition rates between the molecular states involved in fluorescence. k_f: fluorescence rate, k_{ex}: excitation rate, k_n: non-radiative decay rate, k_{isc}: intersystem crossing rate, k_p: phosphorescence rate, k_{bleach}: bleaching rate. [24] *B) Excitation (light blue) and emission (light green) spectra for eGFP protein (modified from https://www.fpbase.org/). C) Scheme of the functioning of an epifluorescence microscope: the filter cube is the element in which fluorescence photons are filtered and selectively directed toward the detector. It contains chromatic filters and a dichroic mirror, that is used to separate excitation and emission photons. While excitation light is reflected by the dichroic mirror toward the sample, fluorescence photons, emitted isotropically from the sample, pass through the dichroic mirror and reach the detector* [24].

The absorption of a single photon is not the only way to excite a molecule with light, indeed the $S_0 \rightarrow S_1$ transition can also be induced by a multiphoton process, in which multiple photons are absorbed sequentially within a time interval of $\sim 10^{-17}$ s [25]. The excitation rate k_{ex} (considering the $S_0 \rightarrow S_1$ transition) due to the interaction of the fluorophore with N photons is related to the excitation light intensity I by the absorption cross-section coefficient σ according to the equation

$$k_{ex}^{(N)} = \sigma^{(N)} \cdot I^N \qquad (1)$$

where N is the number of absorbed photons, $[I]$ = photons s^{-1} cm^{-2} and $[\sigma^{(N)}]$ = photons^{-N} cm^{2N} s^{N-1} [25]. The absorption cross-section $\sigma^{(N)}$ is a measure of the likelihood of the interaction of N exciting photons and the fluorophore. Its value is very low for multiphoton processes and it decreases with the probability of having more particles interacting, that means having them close enough, both in space and in time. Because of the small cross section and of the non-linearity in *(1)*, due to the exponential relation between the excitation rate k_{ex} and light intensity I, spontaneous multiphoton absorption is negligible in nature. Nonetheless, this process can be artificially induced using high power laser sources. Two-photon absorption was indeed first postulated in 1931 by Marie Goeppert-Mayer [26], but experimental evidence for it only came with the introduction of pulsed lasers in 1961 [27] and in 1990 it was first applied for fluorescence microscopy [28], becoming to date the most widely used multiphoton excitation process.

In two-photon fluorescence excitation, the $S_0 \rightarrow S_1$ transition is due to the absorption of two photons (Fig. 2A). Compared to single photon excitation, in which the molecular energy gap $\Delta E = E_{S1} - E_{S0}$ involved in the transition is due to the absorption of a single photon and therefore $\Delta E = h\nu$ (where $h\nu$ is the energy of a photon with frequency ν and h is the Planck constant), in the case of two photon excitation the same energy gap ΔE is covered by the absorption of two photons, hence $\Delta E = h\nu_1 + h\nu_2$. This process can be triggered by two photons with different energies, but in the particular case in which $\nu_1 = \nu_2$, the two-photon absorption excitation is said *degenerate*. In any case the energy of the two photons absorbed is lower than their single-photon counterpart, therefore two-photon excitation spectra result red shifted compared to those regarding single-photon absorption. Note that the emission spectra do not depend on the excitation process involved. Fig. 2B shows one- and two-photon spectra for the eGFP dye. This fluorophore can be efficiently excited by single-photon absorption at 470 nm and its two-photon excitation spectrum peaks around 920 nm [29], which is approximately double the wavelength for single-photon excitation. However, this rule is not valid for all fluorescent dyes and some exhibit unpredictable two-photon excitation spectra. For example red-shifted dyes, like tdTomato and DsRed2, have single-photon absorption peaks near 560 nm and two-photon absorption spectra characterized by two relevant maxima, around 730 nm and 1040 nm [29].

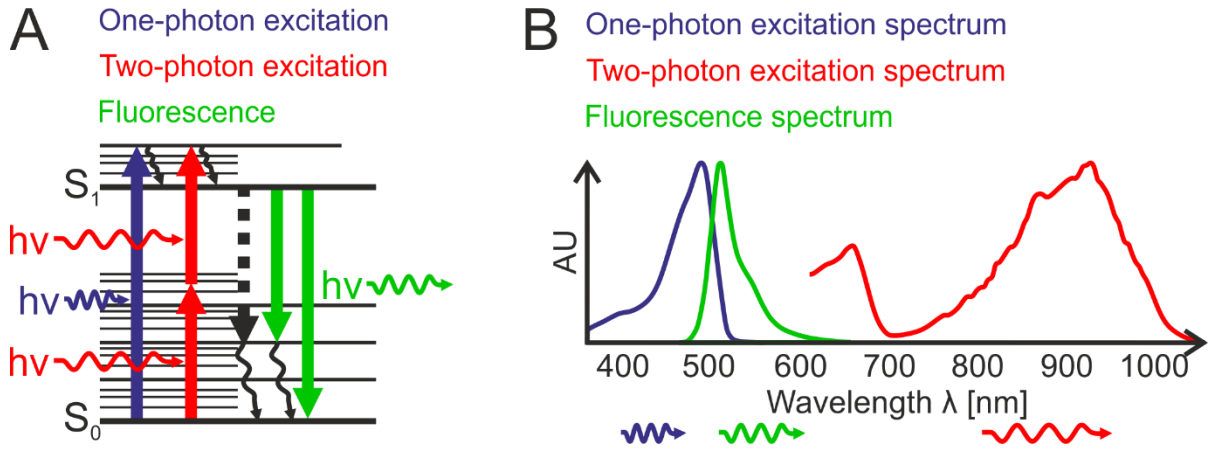

Fig. 2: Two-photon absorption process

A) Jablonski diagram illustrating the transitions between the molecular energy levels S_0 and S_1 occurring for one- and two-photon excited fluorescence. Each arrow represents an energy transition induced by a single photon. The blue arrow represents the transition due to one-photon absorption, while the two red arrows depict the two-step process underlying two-photon excitation. A single fluorescence photon is emitted during the relaxation to the ground state (green). B) The extension of Fig. 1B with the two photon excitation spectrum (red) for eGFP dye (modified from https://www.fpbase.org/).

To overcome the low excitation rate probability and achieve efficient two-photon excitation of fluorophores, the exciting photons must be well confined both in space and time. In two-photon microscopy, spatial and temporal confinement of the exciting photons are obtained with high numerical aperture objective lenses and high power (pulsed) lasers, respectively (Fig. 3A).

1.1.2 Two-photon laser scanning fluorescence microscopy

Multiphoton microscopy has become the preferred technique for high resolution, deep tissue in vivo fluorescence imaging. The major advantage of using multiphoton excitation in fluorescence microscopy comes from the non-linear relation expressed in *(1)*. Indeed, considering that the excitation intensity of a Gaussian beam focused by an objective lens varies as the square of the distance from the focal plane, the result is that, for multiphoton absorption of N photons, the transition rate k_{ex} falls off with the $2N$-th power of the distance along the optical axis z. This axial confinement (called *optical sectioning*) of the focal volume provides intrinsic 3D resolution, in contrast to single-photon excitation (Fig. 3B).

Considering two-photon fluorescence microscopy, the number of fluorescent photons generated per unit time per fluorophore can be written as [30]

$$F_{gen}^{(2)} = \eta \frac{\sigma^{(2)}}{f^2 \tau_P} \left(\frac{\pi (NA)^2}{h c \lambda}\right)^2 < P >^2 e^{-\frac{2z}{l_S^{exc}}} \qquad (2)$$

where $<P>$ is the average excitation power, η, σ, τ_P, and f, are the fluorophore quantum efficiency, two-photon absorption cross-section, laser pulse duration and pulse repetition rate, respectively, NA is the objective numerical aperture, h is Planck's constant, and l_s^{exc} is the tissue scattering length at the excitation wavelength, $\lambda = c/\nu$.

From *(2)* it is evident that higher NA values generate higher fluorescence signals at the focal plane, but for the particular case of two-photon excitation of a thick sample, the time-averaged fluorescence photon flux generated by the entire excited volume does not depend on NA [31]. High values of this parameter are still relevant for a better 3D spatial resolution and for the optimization of photon collection efficiency φ, which scales as NA^2, indeed the total collected fluorescence can be calculated in fact by multiplication of F_{gen} and φ [30]. Moreover from *(2)*, for an average excitation power $<P>$, it is clear that short laser pulses τ, which restrict the generation of photons to small time windows, are needed to maximize F_{gen}.

Regarding biological applications, the main advantages of two-photon microscopy compared to single-photon wide-field imaging are the followings:

- intrinsic 3D spatial confinement of the excitation volume, and therefore reduced photobleaching [32]–[36] and photodamage from out-of-focus planes [37].
- use of longer wavelength excitation, and therefore increased l_s^{exc}, leading to longer penetration depths in scattering tissues, and reduced tissue photodamage [38].

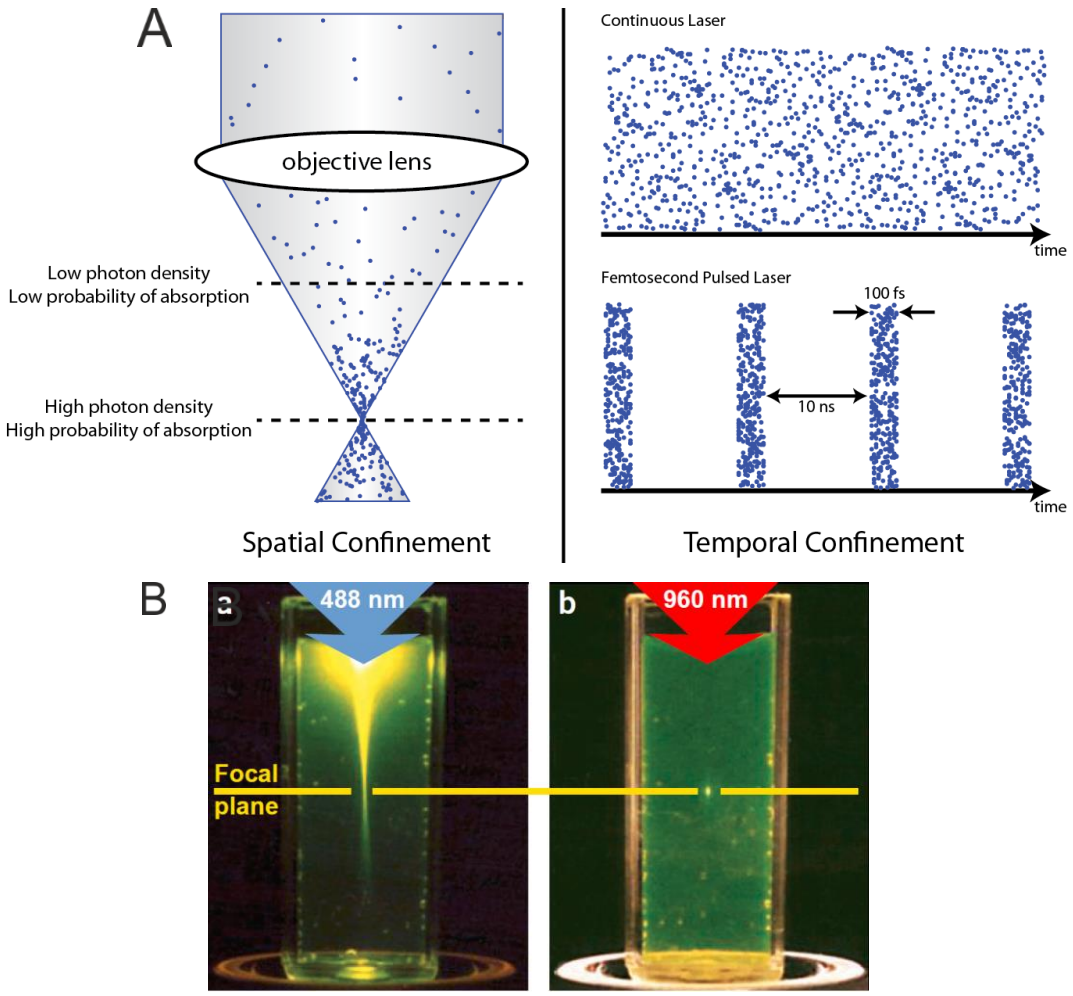

Fig. 3: Two-photon excitation through focusing of femtosecond pulsed laser

A) Spatial and temporal confinement of exciting photons (represented by dots) obtained by focusing a pulsed laser source. Combining an objective lens, that can confine photons in space (left), with a pulsed laser souce, in which photons are intrinsically confined in small temporal windows (typical temporal scales are reported in the figure), it is possible to induce the two-photon excitation process. Multiphoton excited fluorescence is generated efficiently solely at the focal plane. The lack of out-of-focus multiphoton absorption reduces overall phototoxicity in the sample and enhances contrast in deep-tissue imaging. Image taken from http://sites.middlebury.edu/durst/research/. B) Localization of the excitation volume in fluorescin with single-photon (left) and two-photon excitation using the same objective lens. [39]

Laser scanning microscopy (LSM) is required to perform two-photon fluorescence imaging. In this configuration, a pair of galvanometric mirrors is used to pivot the collimated excitation light around the back focal aperture of the objective, thereby obtaining a sequential scan of the focal spot over the 2D focal plane. Raster (line-by-line) scanning (Fig. 4A) is the standard modality for the generation of an image by point-scanning illumination and its major drawback is the limited scanning rate (a few Hz for a 512x512 pixels image). Indeed, the value of each pixel within an LSM

image is proportional to the fluorescence signal collected when illuminating a single point on the sample and images are generated pixel by pixel, with the spatial resolution of the system given by the dimension of the focal spot that is illuminating the sample point-by-point in a sequential manner. Each pixel corresponds to a position of the scanned focal spot on the sample and the frame period can be calculated multiplicating the number of pixels constituting the image by the dwell time, which is the time spent illuminating each scanned position and is usually set in the order of a few μs.

The schematic of a two-photon microscope is shown in Fig. 4B. The laser beam comes from a broadband femtosecond pulsed source. At first, scanning mirrors and a scan lens create a scanned point at the scan lens focal plane, that passing through the tube lens and objective, is then de-magnified at the sample. Sequentially, for each position of the scanning focal spot, emitted fluorescence is collected by the same objective, spectrally separated with a dichroic mirror and filtered towards a single-element light detector (e.g., a multi-alkali PMT or GaAsP PMT). For each scanned position, fluorescence is indeed generated only inside the excited focal volume, therefore all the collected fluorescent photons, scattered or not by the tissue, represent a useful signal reflecting the sample's fluorescent properties at that focal position. Light detectors are usually placed close to the back aperture of the microscope objective in order to improve the collection efficiency.

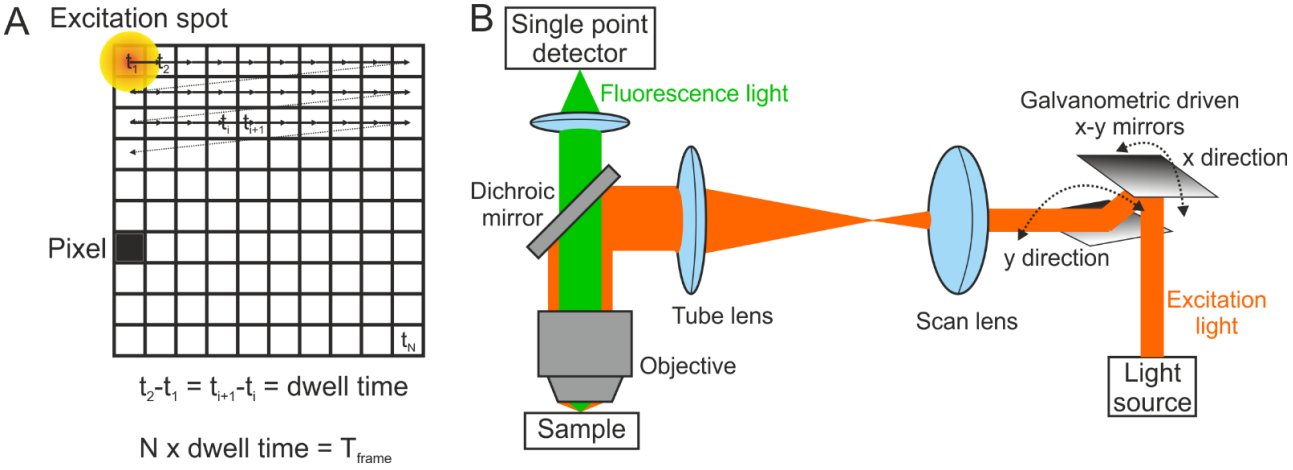

Fig. 4: Two-photon scanning fluorescence microscopy set up

A) Representation of the trajectory followed by the scanned focal spot during image acquisition in raster scanning modality. The fluorescent signal is acquired point by point (each point representing one pixel) along adjacent lines before the full image can be reconstructed [40]*. B) Scheme of a two-photon light scanning microscope. Laser light is steered by a couple of galvo mirrors and passed through scan lens and tube lens to obtain a collimated beam, fitting and pivoting around the back entrance pupil of the objective. This results in the scanning of the focal point on the objective focal*

plane. Fluorescence light is then collected by the same objective and transmitted by the dichroic mirror toward the photon sensor [41].

The most popular type of laser source for two-photon fluorescence LSM (2P-LSM) applications is Ti:Sapphire. These lasers typically run at repetition rates f of approximately 80 MHz, resulting in pulses separated by 12.5 ns, that is a sufficient interpulse period for fluorescent dyes commonly used in biological research. Indeed, the fluorescence decay times are shorter than 10 ns [42], and therefore 80 MHz repetition rate allows the efficient collection of all photons emitted by fluorophores.

Ti:Sapphire sources for this application are designed with a pulse duration τ_P of approximately 150 fs, which corresponds to a spectral bandwidth of about 10 nm. This choice is made to limit pulse broadening along the excitation pathway. Indeed, in typical microscopes, the group delay dispersion (GDD) is about 10.000 fs^2 at worst, therefore the duration of the pulse at the sample plane results usually < 250 fs.

Ti:Sapphire crystals, with a peak at 800 nm and a gain window between 650 nm and 1100 nm, are tunable over a relatively large spectral range [43] and this is a considerable advantage, given that most common fluorophores have broad two-photon absorption spectra (see Fig. 2B).

As already mentioned, the use of longer excitation wavelengths makes two-photon microscopy less sensitive to scattering compared to single-photon and this is relevant because in many biological tissues, for excitation wavelengths of interest, scattering is dominant over absorption. Light scattering in mammalian brain tissue, for example, is almost ten-fold smaller in the near-infrared (NIR) band compared to the visible (VIS) portion [44]. 2P-LSM can thus reach deeper regions compared to single-photon excitation and for example, while two-photon fluorescence microscopy can image 800 μm deep in rodent cortical tissue [45], single-photon imaging is limited to the superficial 100 μm.

Keeping the same average laser power, but reducing the pulse repetition rate (from 80 MHz to 1 kHz for example) and hence increasing the pulse peak energy, it is possible to increase the maximal two-photon imaging depth [46]. With this approach, using a regenerative amplifier with λ = 925 nm, imaging can be performed 1000 μm deep in the mouse brain and using more red-shifted excitation light (λ = 1280 nm), two-photon excitation has reached even deeper regions (down to 1600 μm) [47]. Alternatively, three-photon excitation can be used and with λ = 1700 nm, it is possible to image rodent hippocampus (at a depth of 1400 μm) without the removal of the overlying tissue [48]. Nevertheless, three-photon excitation wavelengths are less affected by tissue scattering but are more absorbed by water molecules and moreover, decreasing the laser repetition rate or using three-photon excitation, significantly reduces the frame rate of acquisitions, because in both cases a longer dwell time is required.

1.1.3 Functional imaging through fluorescent indicators of neural activity

Brain fluorescence functional imaging is the study of neuronal activity through fluorescence. This is possible thanks to fluorescent functional indicators, that are fluorophores characterized by a fluorescence probability that is dynamically modulated by neuronal activity [49], [50]. Coupled with multiphoton imaging, fluorescent functional indicators allow unprecedented opportunities to assess the spatiotemporal dynamics of well-defined neuronal populations (see section 1.6) with cellular resolution in living animals.

Sub- and supra-threshold membrane potential changes are among the most relevant features of neural physiology to extract. However, direct sensing of membrane potential with optical indicators that change their emitted fluorescence according to voltage variations has been challenging and just a few fluorescent voltage indicators have been effectively applied *in vivo* [51]–[53].

Nonetheless, action potentials cause the net influx of Ca^{2+} ions into the cell cytoplasm following the opening of voltage sensitive Ca^{2+} channels.. Intracellular calcium concentration hence increases during spikes (typically from 50–100 nM to 5–10 μM) and then returns to baseline conditions in 100-500 ms through mechanisms of calcium extrusion and internal buffering [19]. Therefore, neuronal electrical activity can be measured indirectly through changes in intracellular calcium concentrations. One possibility to optically measure these variations is by means of molecules with optical properties, such as fluorescence, that change upon calcium binding [19], [54], [55]. The response of fluorescent functional indicators, including their affinity, selectivity, dynamic range and kinetic properties, is determined by conformational changes due to calcium binding as well as by the biophysical properties of these molecules [56]. Neurons loaded with these compounds display fluorescence changes synchronously with AP firing. Functional imaging moreover, can be efficiently applied not only for the indirect investigation of suprathreshold electrical activity in neuronal cells, but also to study the excitability of glial cells, which modulate many brain functions [57]–[59] and display intracellular calcium variations that correlate with neuronal signals [60].

Fluorescence neuronal dynamics are commonly measured calculating the $\Delta F/F = (F-F_0)/F_0$, where F is the fluorescence signal obtained by averaging over the pixels corresponding to a neuron and F_0 is the baseline of this signal, usually expressed as a percentage, as shown in Fig. 5.

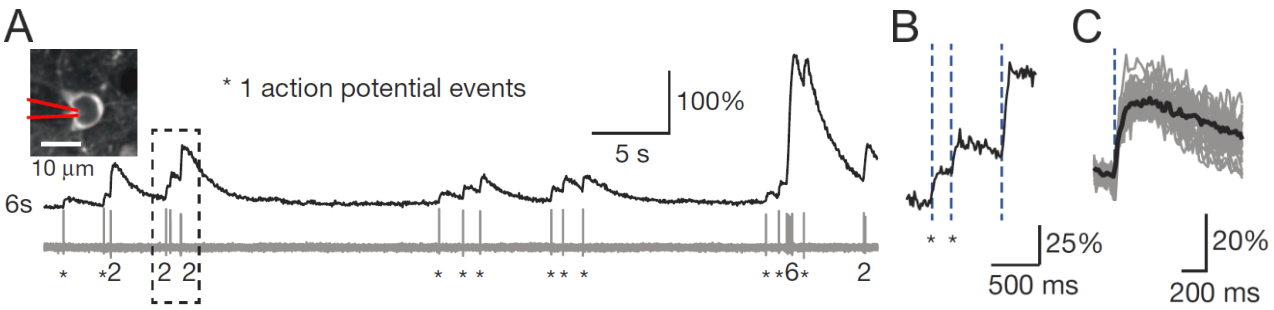

Fig. 5: Neuronal activity indirectly measured with calcium-dependent fluorescent molecules

A) Corresponding fluorescent dynamics (top trace) and spiking activity (bottom trace, also indicating the exact number of action potentials fired) simultaneously recorded from a GCaMP6s expressing neuron, depicted with the recording pipette in the left inset. On the right, zoomed-in views of fluorescence responses respectively to three temporally close action potentials (single recording, B), or to a single action potential (averaged response from multiple recordings, C), showing single spike detectability [61].

At first, bioluminescent calcium-binding proteins, such as aequorins, were used [62], [63], but chemists then developed a wide range of synthetic calcium indicators with optimized functional properties. Most of these fluorophores were obtained through the combination of a fluorescent chromophore (responsible for its spectra) and a highly sensitive calcium chelators (e.g., EGTA and BAPTA) that binds very tightly to calcium ions [64]–[66]. Examples of these calcium dyes are Oregon Green BAPTA-1 (OGB-1) and Fluo-4, and their ease of implementation, large signal-to-noise-ratio, affinity to Ca^{2+} and photostability helped their spread in neuroscience applications [19], [67]–[69]. However, synthetic calcium indicators suffer from some limitations for certain uses, indeed it is difficult to selectively label specific neuronal subpopulations and they are not suitable for long-term, repeated measurements because of their limited lifespan in cells.

A great innovation came from the Nobel Prize awardee Roger Tsien [70], who, after the discovery of GFP, introduced a new generation of protein-based fluorescent dyes, *genetically encoded calcium indicators* (GECIs). These compounds, that are obtained by the fusion of a calcium binding molecule (calmodulin for example) and a fluorophore, can be expressed in specific neuronal subpopulations for long time periods thanks to transgenic technologies that combine the use of cell-specific promoters (see section 1.6) and subcellular targeting sequences [19], [61], [71]–[73], thus partially circumventing the pitfalls of synthetic dyes.

In the beginning GECIs were characterized by small signal-to-noise ratios and slow response kinetics and because of this, they were restricted to only a few applications [74]–[76]. However, over the last 15 years, efforts have been made to develop variants with greater brightness and sensitivity, in some cases showing performances comparable to their synthetic counterparts [77]–[79]. At present, GECIs and the family of GCaMPs in particular are sensitive enough to report, under

optimized experimental conditions, calcium transients associated with single AP firing *in vivo* (see Fig. 5) [61], [79], [80]. GCaMP proteins are composed by three subunits: a circularly permuted GFP (cpGFP) [81], a calmodulin moiety and the M13 domain of myosin light-chain kinase. Normally, there is no interaction between calmodulin and M13, but in the presence of calcium binding, their interaction induces a conformational change in the cpGFP that leads to a substantial enhancement of the emitted fluorescence [82], [83].

Several GECIs with different spectral properties have been developed and characterized [80], [84], [85], and although to date GFP-based GCaMPs usually have been preferred, the future implementation of probes with shifted absorption spectra promises to facilitate simultaneous functional imaging from different neuronal subpopulations and its combination with optogenetics (see section 1.5), thus enabling real-time manipulation and readout of neuronal activity. Moreover, fluorescent calcium indicators, coupled with fundamental advances in optical imaging (discussed in the previous section) are leading to new interest in the optical dissection of neuronal circuits with high spatiotemporal resolution [19]–[21], [86]. The combination of 2P-LSM with fluorescent functional indicators is today among the most powerful approaches to explore brain function with cellular resolution. It allows a broad range of neuroscience investigations in different organisms, for example mapping sensory information encoding in selected neuronal populations, in vivo connectivity measurements, correlations between structure and function, analysis of anatomical and functional plasticity and neurovascular coupling [17], [45], [86]–[90].

In conclusion, thanks to several innovations in the last 20 years, namely optical design of multiphoton systems, computational microscopy methods and protein engineering, it is to date possible to visualize the synchronized activity of thousands of neurons with subcellular spatial resolution in behaving mammals. Also, future developments in the field are promising, because experimental parameters such as signal-to-noise-ratio, temporal resolution, field of view dimensions, accessible volume and penetration depth are improving year by year [21], [91].

1.2 Optical aberrations

As discussed in section 1.1.2, the spatial resolution in two-photon scanning microscopy is determined by the extension of the excitation volume obtained by the focusing power of the objective lens proximal to the sample. The ability of an optical system to focus light efficiently in a small focal volume is measured through its Point Spread Function (PSF), defined as the image obtained from an ideal point source object. Therefore, the PSF determines the quality of an imaging system and indeed, images are generated by a convolution between the real light source and the PSF of the optical system.

Aberrations degrade the spatial confinement of the focal spot, enlarging the PSF and hence reducing both the spatial resolution of the imaging system and the probability of the two-photon absorption process. It is thus of fundamental importance to perform imaging with a system in which the PSF is not affected by aberrations. Such a system is termed diffraction-limited and its resolution performance is determined by the theoretical limit imposed by the physics of diffraction. The PSF of a diffraction-limited system is not an ideal point, but it is actually an Airy pattern (a bright central area surrounded by dark and bright rings), which is mathematically expressed in term of a Bessel function of the first order [92]. With *NA* (the numerical aperture of the optical system) defined as $NA = n\ sen\vartheta$, where *n* is the refractive index of the imaging medium and ϑ the aperture angle (the half angle from which the optical system can gather light), according to the Rayleigh criterion, two distinct points can be resolved within an image until the lateral distance ΔX between the two corresponding Airy disc patterns is greater than $\lambda/2NA$. This is therefore the lateral spatial resolution of a diffraction-limited imaging system and it is a function of both wavelength and numerical aperture. PSFs in general result elongate in the axial direction, hence the axial resolution is worse, resulting in $\Delta Z = \lambda/NA^2$.

More precisely, for a diffraction-limited two-photon fluorescence microscopy, the focal spot can be considered as a 3D Gaussian shaped region with an effective volume [39]:

$$V_{TPE} = \pi^{3/2}\omega_{xy}^2\omega_z \qquad (3)$$

where

$$\omega_{xy} = \begin{cases} \frac{0.320\,\lambda}{\sqrt{2}\,NA} & if\ NA \leq 0.7 \\ \frac{0.325\,\lambda}{\sqrt{2}\,NA^{0.91}} & if\ NA > 0.7 \end{cases} \qquad (4)$$

$$\omega_z = \frac{0.532\,\lambda}{\sqrt{2}}\left[\frac{1}{n-\sqrt{n^2-NA^2}}\right] \qquad (5)$$

are the transverse (xy) and axial (z) dimensions of the Gaussian curves fitting the sections of this volume. V_{TPE}, like spatial resolution, is a function of both wavelength and NA, and it is degraded by aberrations, which indeed reduce light confinement.

1.2.1 Optical aberrations in imaging systems

An optical imaging system is a sequence of optical elements that generate the image of an object. In order to model the performance of optical systems, the concept of light rays is convenient: light rays are the trajectories followed by points on a light wavefront (surface of constant phase). They are collinear with wave vectors, which are defined as those vectors normal to the wavefront, and indicate the direction of energy propagation.

Ray (also called geometrical) optics makes use of Snell's law and Fermat's principle to determine trigonometrical relations that describe how light rays behave while passing through an optical

system. It is an approximation in which light propagates along straight lines in homogeneous media, bends (or may split) at the interface between optically different materials and may be absorbed or reflected. Scattering and interference (which are wave properties of light) are not considered in this approximation, and therefore it is a good estimate only when light interacts with structures much bigger than its wavelength.

A further simplification is applied in Gaussian optics, in which the paraxial (small-angles) approximation is adopted to calculate the trajectories of rays. In this case, only paraxial rays, those which intersect with the optical axis of the system with small angles, are considered. Gaussian optics is also called first-order optics because the trigonometric relations are substituted with the first term of their Taylor series: $sen\theta \sim \theta$, $tan\theta \sim \theta$, $cos\theta \sim 1$, with the result that it becomes much easier to determine height and slope of light rays for each position along the optical axis. Gaussian optics is largely applied in the modeling and design of imaging systems to calculate optical performance such as image position, size and orientation, but given that it is a strong approximation, only optical systems accurately fabricated will meet the predicted performances. Gaussian optics indeed simulates the performance of perfect optical systems.

Nonetheless, Gaussian rays provide useful references to evaluate deviations from perfection, namely to evaluate optical aberrations. In a perfect optical system (as simulated by Gaussian optics) indeed, all wavefronts are spherical (converging on or diverging from a point) or planar (collimated light) and incident spherical waves are mapped to a perfectly spherical wavefront in the exit pupil, generating a perfect point-to-point conjugation between object and image planes (Fig. 6A). But this is not what happens in reality, and large amount of aberrations can be estimated by comparing paraxial ray trajectories with those obtained using the exact trigonometrical ray-tracing equations [93]. Nonetheless, geometrical optics loses its validity as aberrations become small. This is evident if we consider that, as we mentioned before, the PSF is never a perfect point, even in the case of an imaging system that, unaffected by aberrations, is able to generate light perfectly focused after its circular aperture. Indeed, while the approximated geometrical approach predicts a perfect image point (with infinite intensity at the focal spot and zero elsewhere), when diffraction effects are considered, the real image consists of an Airy pattern. It is thus evident that small amount of aberrations, which cause little deviation from the ideal case, are better described on the basis of diffraction theory, considering the wave nature of light (wave optics).

As already indicated, light rays are in fact trajectories followed by points on the wavefront and result normal to the wavefront itself, therefore a bundle of light rays converging to form a perfect unaberrated image point corresponds to spherical wavefronts centered on the focal point. In this picture, aberrations result in deformations of the wavefronts respect to the ideal spherical shape, and can be evaluated by measuring either the wavefront aberration function W, which is the optical path difference (OPD, commonly expressed in units of wavelength), along rays, between the

aberrated wavefront and the reference spherical wavefront (usually calculated at the exit pupil plane) (Fig. 6B) or equivalently, by the transverse ray error ε, which is the lateral distance between aberrated rays and the ideal image point, on the image plane (Fig. 6B).

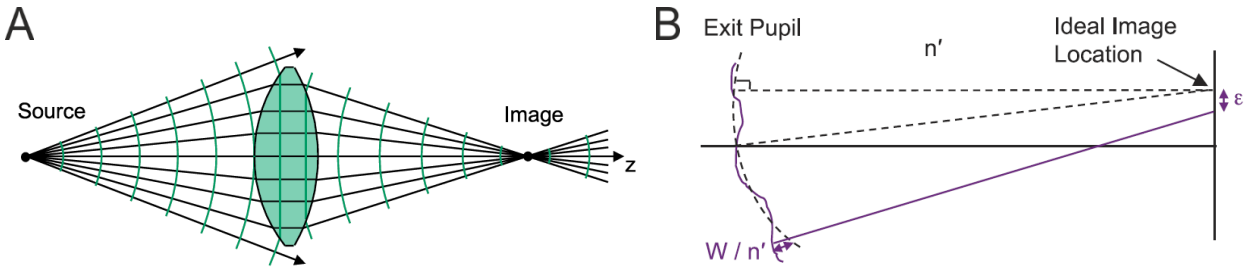

Fig. 6: Gaussian approximation is used to evaluate ideal optical performances, then used as reference for the evaluation of aberrations

A) In Gaussian optics approximation, there is a perfect correspondence between points in the object and image planes. No aberrations are considered [94]. *B) Representation of the wavefront aberration W determined as the OPD between the aberrated wavefront and the ideal spherical one, for the ray described as a solid line. W is usually calculated at the exit pupil plane, that is the image of the system stop aperture in the image space The transverse ray error is also shown for the same ray, and it is calculated on the image plane* [95].

The calculation of the aberrated wavefront function *W(x,y)* is a complex problem, but the evaluation of aberrations has been highly simplified by Seidel. Indeed he understood that the common faults affecting imaging systems (and therefore wavefront shape) could be classified into a handful of types. He codified the primary (Seidel) aberrations (spherical aberration, coma, astigmatism, field and Petzval curvature and distortion) and derived their analytical expressions.

The usual procedure to describe wavefront aberrations is to write *W(x,y)* as a polynomial expansion in which each term represents a particular type of aberration and is associated with a coefficient that indicates how much that type of aberration affects the imaging performance of the optical system. Traditionally, two sets of such polynomials have been used to fit *W(x,y)*: Seidel and Zernike polynomials. Seidel polynomials are typically used during optical system design and cannot take into account aberrations induced by decentralization and tilt. Zernike polynomials, which form a complete set of orthonormal functions inside the unit circle domain, and thus guarantee the possibility to fit any continuous surface, are considered for optical testing and measurements. Once the aberrated wavefront has been fitted, it is possible to quantify the overall faults of the imaging system by measuring the *peak-to-valley* (*P-V*) wavefront aberration, which is the maximum difference between the actual and spherical reference wavefronts. Another approach, in general more meaningful, is to specify imaging quality by using the *RMS wavefront error*, which is not a local measurement like *P-V*, but also considers the area over which aberrations occur.

Considering an imaging system that is circularly symmetric around the optical axis, it is possible to specify any ray with only three coordinates: its 1D position in the object (or image) plane (namely field coordinate H, typically along y and normalized to the maximum field position) and its 2D position in the exit pupil plane (aperture, expressed in polar coordinates ρ and φ, usually normalized to have an amplitude of 1 at the edge of the pupil). Therefore, given that these three coordinates are sufficient to describe the trajectories followed by rays, and the corresponding propagating wavefronts passing through the optical system [92], [96] and that monochromatic aberrations (those that do not depend on λ) are described by evaluating the power series expansion of the wave aberration function *W*, it is possible to use ρ (the normalized exit-pupil radius), φ (the exit-pupil angle from the meridional plane) and H (the normalized height of the intersection with the image plane), as shown in Fig. 7A, as variables to expand the wavefront aberration function W as a power series. In order to satisfy rotational symmetry requirements, the terms of the expansion are composed by factors in the form of H^2, ρ^2, or $H\rho cos\vartheta$:

$$W(H^2, \rho^2, \rho H cos\theta) = \sum_{m,n,k} W_{m,n,k} \rho^{2m} H^{2n} (\rho H \cos\theta)^k = \sum_{m,n,k} W_{m,n,k} \rho^{2m+k} H^{2n+k} (\cos\theta)^k \quad (6)$$

This can be rewritten with the indices $i = 2n+k$, j = 2m+k, and k = 0,1,2,...

$$W(H, \rho, cos\theta) = \sum_{i,j,k} W_{i,j,k} H^i \rho^j (\cos\theta)^k \quad (7)$$

In this way, the wavefront aberration function is expressed as a sum of different polynomials (with a characteristic shape for each type of aberration) weighted with the coefficients $W_{i,j,k}$.

The first terms of this series are related to the Seidel expansion, which is in the form

$$W(H, \rho, cos\theta) = \frac{1}{8} S_1 \rho^4 + \frac{1}{2} S_2 H \rho^3 cos\theta + \frac{1}{2} S_3 H^2 \rho^2 (cos\theta)^2 + \frac{1}{4} (S_3 + S_4) H^2 \rho^2 + \frac{1}{2} S_5 H^3 \rho cos\theta \quad (8)$$

as reported in Table 1, in which the different types of aberration are listed.

Wavefront aberration coefficient	Seidel aberration coefficient	Functional form	Aberration name
W_{200}		H^2	Piston
W_{111}		$H\rho cos\vartheta$	Tilt
W_{020}		ρ^2	Focus
W_{040}	$1/8\ S_1$	ρ^4	Spherical
W_{131}	$1/2\ S_2$	$H\rho^3 cos\vartheta$	Coma
W_{222}	$1/2\ S_3$	$H^2\rho^2(cos\vartheta)^2$	Astigmatism
W_{220}	$1/4\ (S_3 + S_4)$	$H^2\rho^2$	Field curvature
W_{311}	$1/2\ S_5$	$H^3\rho cos\vartheta$	Distortion

Table 1: Seidel aberrations and their functional forms.

W and ε are related by a partial derivative with respect to the pupil coordinate ρ ($\varepsilon \propto \partial W/\partial\rho$), and therefore n^{th} order transverse aberrations correspond to $n+1^{th}$ order wavefront aberrations. Based on the order of transverse aberrations, first order terms in the expansion are those considered in the Gaussian approximation (piston, tilt and focus in Table 1), while higher order terms (3^{rd}, 5^{th}, 7^{th}, etc.) represent aberrations and quantify the difference with respect to the ideal image point obtained with paraxial equations. Third-order terms are five and correspond to Seidel aberrations, also called primary aberrations (Table 1).

The description of the wavefront aberrations can be also performed with Zernike polynomials, which are defined as

$$Z_n^m(\rho,\theta) = N_m^n R_m^n(\rho)\Theta(\theta) \qquad (9)$$

where N is the normalization factor, R the radial function and Θ the azimuthal component [97]. The first Zernike polynomials are depicted in Fig. 7B.

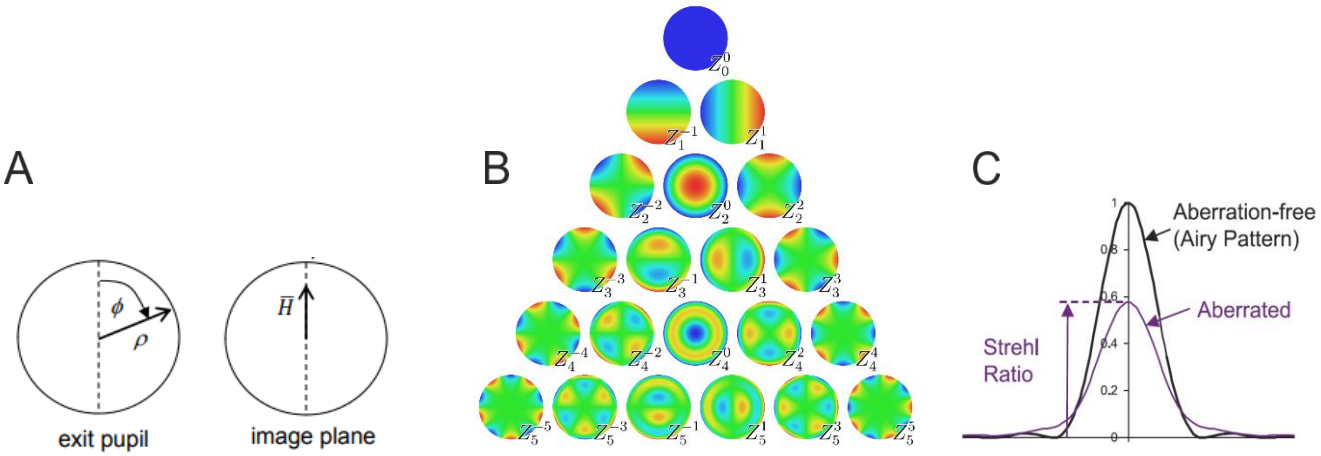

Fig. 7: Circular symmetry ray variables, Zernike polynomials and strehl ratio

A) The three variables used for the polynomial expansion of the wavefront aberration function are depicted in the planes in which they are defined. B) Zernike polynomials are used in optics to measure wavefront aberrations and to model surface smoothness. Each Zernike polynomial is composed of three terms: a normalization factor (usually to have a RMS = 1), a radial-dependent part (polynomial), and an azimuthal-dependent component (sinusoidal). Different polynomials correspond to different aberrations: (n=2,m=0) is defocus, (4,0) is spherical, (3, ±1) is coma and (2, ±2) is astigmatism. C) Strehl ratio, as discussed in the text [95]

If aberrations are affecting imaging performance, the image point of maximum intensity (called aberrated focus) in general will not coincide with the aberration-free Airy pattern and will be less bright. Another way to quantify the imaging performance of an optical system is to specify the ratio of the intensities of the aberrated focus and the diffraction limited Airy pattern. This quantity is called the *Strehl ratio* and can be determined from the *RMS wavefront error*. The *Marechal criterion* then states that an optical system can be regarded as well-corrected if the Strehl ratio is greater than or equal to 0.8, which corresponds to an *RMS wavefront error* less than or equal to *λ/14*.

What follows is a description of how the imaging performance of an optical system is affected by the main types of aberrations.

Spherical aberration is the variation of focus position with aperture: light rays close to the optical axis are focused near the paraxial focus, but as long as the ray height on the lens increases, its focal position is moved away from the paraxial focus (Fig. 8A). For rays of different height, *longitudinal* spherical aberration (LA) is measured along the optical axis while *transverse* spherical aberration (TA) is evaluated in the perpendicular direction, along the *paraxial focal plane*.

A point imaged through a system affected by spherical aberration is a bright spot with a halo of light all around (see Fig. 8B) and this results in images with lower contrast and blurred details. Spherical

aberration can be corrected by using a cascade of optical elements, in order to distribute rays bending on several surfaces, or by changing the angle of peripheral rays with respect to axial rays.

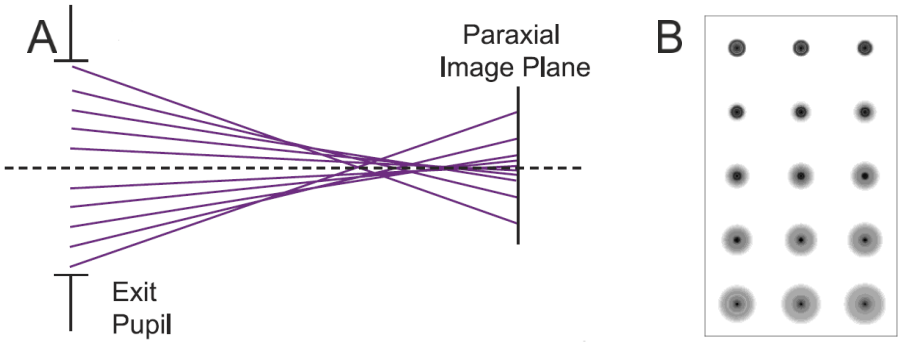

Fig. 8: Spherical aberration

A) Raytracing showing that rays from different heights are focused at different axial positions [95]. *B) Sequence of acquisitions (line by line) at different axial position for an image point* [98].

Coma is the change in magnification with aperture: oblique rays passing at different distances from the optical axis are imaged at different heights. Identified the transverse plane perpendicular to the optical axis in which rays passing at the edges of the lens intersect, the tangential coma is measured as the distance between the height H_{AB} of the intersection of the rays, and the height H_P where the ray passing through the center of the lens intersect the same plane, as depicted in *Fig.* 9A. The name is due to the comet shape (see Fig. 9B) characterizing the point image obtained when this type of aberration is present. Its effect is very detrimental for image quality because of the pronounced asymmetry of the point image shape, especially towards the edges of the images, infact there is no coma on the optical axis if the system is axially symmetric. For a single lens, coma can be corrected by optimizing the bending parameter of the lens: this means choosing the best surface shapes of the lens, keeping its index of refraction and focal length fixed. As depicted in Fig. 9C, there is a particular lens shape that gives zero coma, while spherical aberration cannot be completely corrected in this way. For multiple optical elements, poor alignment increases coma.

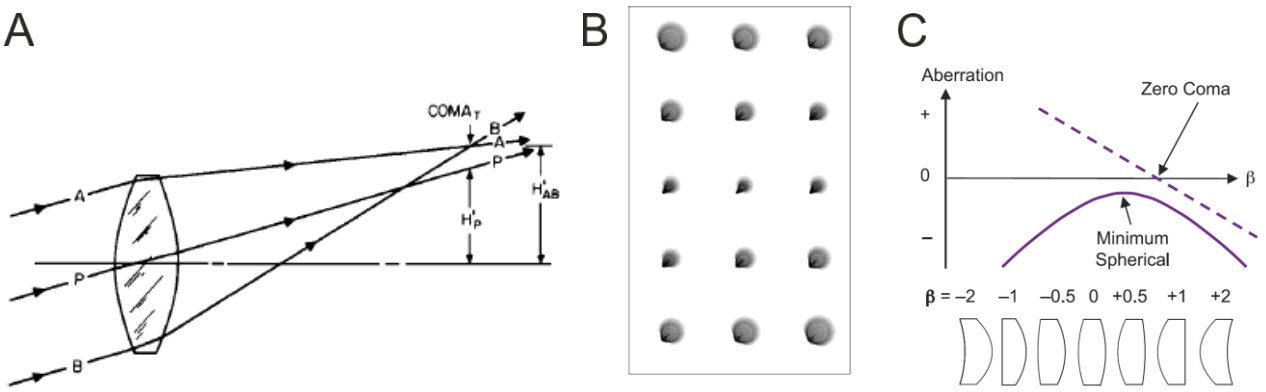

Fig. 9: Coma

A) Raytracing representation of coma. B) Sequence of acquisitions (line by line) at different axial position for an image point [98]. *C) Plots showing how aberrations are affected by the bending factor β of a single lens.*

Astigmatism is when tangential and sagittal images do not coincide (see Fig. 10A). Tangential (also called meridional) planes are those containing the optical axis of the imaging system. An object point therefore defines a tangential plane and rays passing through this point and laying on the tangential plane are called tangential rays. In particular, the tangential ray passing through the center of the system aperture is called the principal (or chief) ray. Skew rays instead are those that do not lie in a tangential plane. The sagittal plane is that perpendicular to the tangential plane and which contains the principal ray and skew rays laying in the sagittal plane are called sagittal rays. Oblique tangential and sagittal fans of rays coming from a point object generate line images (tangential and sagittal images respectively) lying in perpendicular planes (sagittal and tangential planes respectively). When astigmatism occurs, tangential and sagittal images do not coincide and the image of a point source appears as two lines separated by elliptical or circular blur (see Fig. 10B). Like for coma, in general, astigmatism is not present when a point on-axis is imaged, so image formation is particularly degraded toward the edges. Misalignments between optical elements increase this type of aberration. Astigmatic images are formed on separated curved surfaces that are paraboloid in shape and do not coincide with the Petzval surface (see Fig. 11). If there is no astigmatism, tangential and sagittal images instead coincide on the Petzval surface.

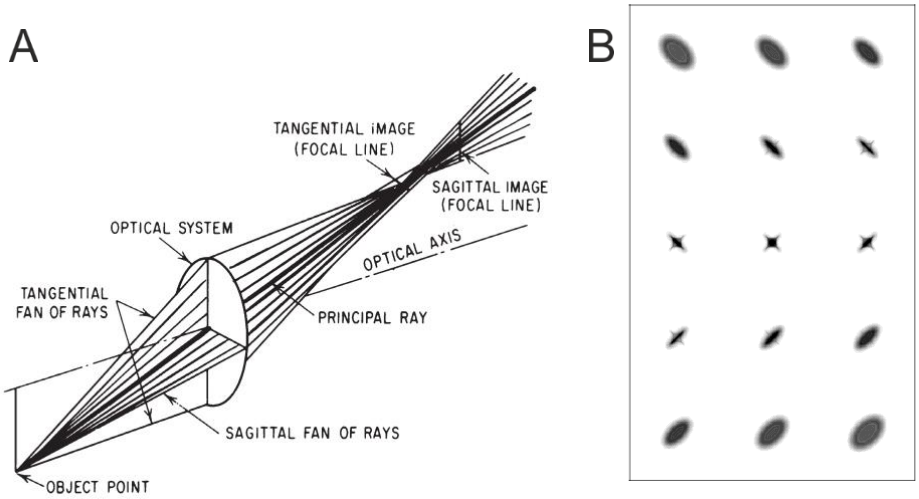

Fig. 10: Astigmatism

A) Raytracing representation of astigmatism. B) Sequence of acquisitions (line by line) at different axial position for an image point [98].

Any symmetrical optical system with spherical surfaces form images on curved surfaces. The Petzval surface is the natural *field curvature* that is associated with an imaging system. The longitudinal distance from the ideal flat paraxial image plane to the Petzval surface is called the Petzval curvature, while the distance to the real focal surface is called field curvature. Field curvature is usually corrected with a negative lens (called field flattener) placed in proximity of the image plane.

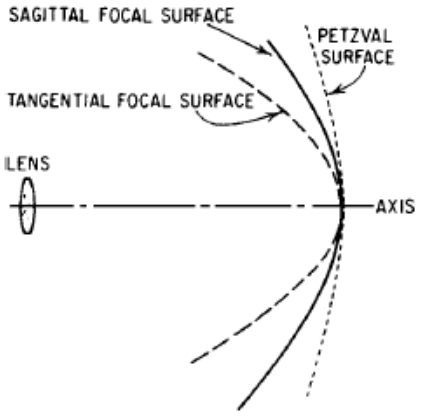

Fig. 11: Field curvature

Image showing the curvature of Petzval surface. Also are reported the surfaces where images are formed in the case of astigmatism. Proportions compared to the lens are respected.

Distortion is a variation of the magnification over image height and results in a displacement of extended images respect to their paraxial position. It appears when off-axis point images are

formed farther from or closer to the axis relative to their paraxial height and the amount of distortion is proportional to the image height, resulting particularly evident at the edges in images of reticles. When images are displaced outwards compared to their paraxial position, it is called *pincushion* distortion, while if they are pulled inwards, it is called *barrel* distortion. Distortion does not actually reduce the information in the image, as for example happens in blurred images, but just misplaces information geometrically. This means that distortion can be calculated or mapped out a posteriori.

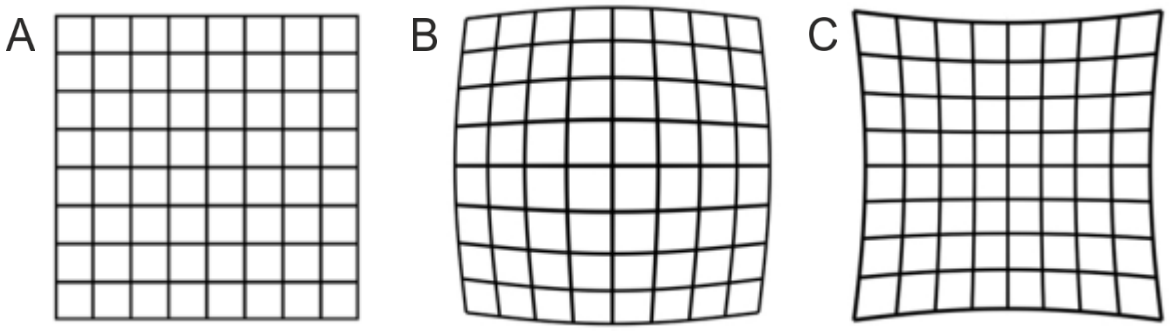

Fig. 12: Distortion

Images of an undistorted (A), a barrel distorted (B) and a pincushion distorted (C) reticle.

Chromatic aberrations take into account the fact that the performance of an optical system varies as a function of the wavelength of light λ. Indeed the index of refraction is a function of λ, resulting in higher values for shorter wavelengths. Different colors are therefore refracted differently through an optical system and they may end up focused in different positions on the image surface, both in the longitudinal and lateral directions, resulting in *longitudinal* and *lateral* chromatic aberrations.

1.2.2 Aberration correction in imaging systems

In the previous section, the different types of aberrations were treated one at a time, but it is common to have them simultaneously affect the imaging performance of an optical system. Moreover, image quality degradation can be due both to aberrations that are intrinsic to the imaging system or to aberrations coming from the interaction of light with the sample, for example, wavefront distortions induced by inhomogeneities in brain tissue while performing functional imaging or distortions induced by Earth's turbulent atmosphere while observing celestial objects through ground-based telescopes. For both categories of aberrations, intrinsic or sample-induced, different strategies have been developed to restore image quality.

Regarding intrinsic aberrations, imaging faults in complex optical configurations are reduced by combining elements with aberrations of opposite signs so that their different contributions cancel

out or correct each other, to generate overall acceptable performance. A typical example is the achromatic doublet, an optical compound element with corrected axial chromatic aberration for two different wavelengths. This correction is obtained by combining two lenses affected by opposite axial chromatic aberrations that compensate for each other. Another memorable example, on a completely different scale, is how the imaging performance of the Hubble Space Telescope improved after the correct compensation for spherical aberration [99]. Thus, it is possible to design complex imaging systems with optimized performance for specific applications by carefully combining different optical elements with specific refractive indices, surface shapes, etc. that together minimize the amount of aberrations affecting the optical system.

Accurate lens design, optimization of parameters, evaluation of aberrations and tolerances are possible today for complex optical systems, thanks to powerful optical software programs, like Zemax, Oslo or CodeV. Nevertheless, aberrations are usually only corrected in a restricted range of operation, for example, just in one zone of the aperture or, as in the case of the achromatic doublet, just for two specific wavelengths. More robust aberration corrections require complex compound systems.

Sample-induced aberrations are those in which focusing light rays are distorted by structures in the sample with different indices of refraction, thus generating an enlarged focus with reduced intensity. They are not completely predictable during the optical system design and are usually analyzed and compensated for while imaging is performed. Their correction will be considered in the next section, focusing in particular on methods developed to perform imaging in brain tissue with long penetration depth.

1.3 Deep brain imaging

As mentioned in section 1.1.2, wavelengths typically used in multiphoton microscopy allow in vivo recording of neuronal activity up to approximately 1 - 1.6 mm deep in brain tissue [47]. Imaging depth is limited by two factors: optical aberrations and attenuation, which refers to light absorption and scattering [100] due to the optical inhomogeneity of brain medium.

One of the approaches used to overcome sample-induced aberrations is Adaptive Optics (AO) [101]–[103], in which a wavefront-shaping device, such as a deformable mirror (DM) or a liquid-crystal spatial light modulator (SLM), is used to compensate for the measured wavefront deformations induced by the sample, as shown in Fig. 13. This is a powerful approach, because while restoring the PSF, it is at the same time compensating for both sample-induced aberrations and potential intrinsic aberrations (for example, due to misalignment in the optical system).

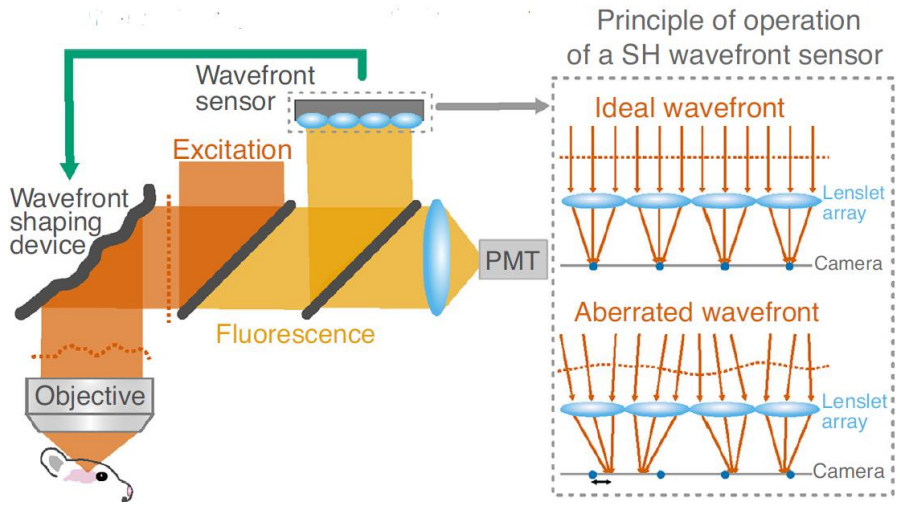

Fig. 13: Adaptive optics setup

Scheme a two-photon fluorescence microscope provided with a wavefront shaping device and a wavefront sensor. In this configuration, aberrations are compensated by shaping the wavefront of the excitation beam according to the aberrations-induced distortions measured with the wavefront sensor, a Shack Hartmann (SH) sensor. On the right it is depicted the working principle of SH sensors [103]*. These sensors are constituted of a 2D array of small focusing lenses in front of a camera. The wavefront shape can be reconstructed considering the positions of the focal spots generated by the lenses when illuminated with a light wavefront. Indeed, while a flat ideal wavefront would generate a 2D array of equally spaced focal spots on the camera, wavefront distortions results in displacements of the focal spots.*

With AO, Ji et al. could resolve synaptic structures down to 760 μm and perform functional imaging of axonal boutons in Layer IV of cortical mouse brain in vivo, while Matsumoto et al. succeded in compensating for aberrations induced by curved sample surfaces [104]. However, choosing the best AO method to use, is complicated by several factors, including spatial and temporal variabilities of aberrations requiring compensation, sample scattering properties, together with the available budget and expertise [103]: this technique indeed requires a substantial upgrade of the experimental setup compared to a standard 2P-LSM, in terms of both hardware and software.
Nevertheless, the correction of sample-induced aberrations can extend imaging penetration depth by enhancing in-focus excited fluorescence, but out-of-focus background signal generated by scattering still sets the ultimate depth limit. Indeed, rather than being absorbed, photons in the visible and near-infrared regime interact with brain tissue mainly through elastic scattering, which is primarily due to interactions with mitochondrial-sized organelles [106]. Novel techniques try to tackle the scattering problem in different ways in order to overcome the imaging depth limitation, for example by reducing it, as in functional photoacoustic microscopy, where optical absorption is measured using ultrasonic waves [107] or by making use of the elastic scattered light and exploit

its deterministic nature [108]. However, these approaches are not yet optimized for fast functional fluorescence imaging. A complementary approach to increase two-photon imaging depth in tissue involves the enhancement of the collection efficiency of fluorescence emission by increasing the objective collection *NA* with non-imaging custom mirrors [109]. On the other hand, almost scattering-free techniques, such as fMRI [110], still do not allow the investigation of brain dynamics at cellular-resolutions, neither in time nor space.

To date, most of the strategies employed to overcome scattering problems and reach deeper regions have focused on the use of longer wavelengths [47], red-shifted fluorescent indicators [105] and/or high peak power laser pulses in order to exploit three-photon excitation [48]. However, these approaches are subject to limitations, such as:

- the chosen wavelength is constrained by the absorption spectra of the fluorescent probe and the properties of the tissue (indeed, for example, for wavelengths beyond 1 μm, the water absorption spectrum becomes relevant);
- higher peak powers aggravate the potential for photodamage in tissue surrounding the focal plane;
- light collection efficiency decreases with imaging depth because of the short mean free path of the fluorescence photons emitted (VIS) in brain tissue. This leads to a reduced SNR and therefore longer acquisition times.

Moreover, scattering and absorption reduce light intensity exponentially with depth, hence attenuation of the exciting beam ultimately prevents imaging in regions deeper than about 1.5 mm. Because of all the abovementioned limitations, micro-endoscopy is a common solution for performing deep (> 2mm) brain imaging with high spatial resolution [111]–[113].

1.3.1 Micro-endoscopy for deep brain imaging

In micro-endoscopy, a thin cylindrical lightguide is used to conduct photons to and from deep tissue regions. Micro-endoscopes are used to transport, at their distal end, the objective focal plane, therefore when inserted into brain tissue and coupled with a microscope (wide-field, confocal or multiphoton), the resulting optical system can provide high-resolution 3D imaging from any deep brain location [114], [115]. Invasiveness is the main drawback of any endoscopic approach, because the solid (and usually rigid) body of the lightguide must be directly inserted into the tissue and may induce relevant damage in the extremely interconnected brain network.

Micro-endoscopes commonly used in rodents for neuroscience applications have small dimensions, with typical diameters in the range of 0.350 – 1.5 mm [116]–[118]. There is a tradeoff in choosing the probe size, indeed endoscopes with a smaller lateral size are less invasive, therefore reducing the damage caused by their insertion, but they also may have significantly decreased optical performance (*e.g.*, lower *NA*, smaller field of view, etc.). However, extremely high *NA* values are not

always needed, and thus simple glass chunks [119], microprisms [120], fiber bundles [121] or phase-conjugated multimode fibers [122] have been efficiently applied. Nonetheless, the use of gradient index (GRIN) optics allows the fabrication of small probes with diameters down to 350 μm [118] while maintaining good imaging performance [123], [124]. Because of their good optical properties and small size, GRIN lens-based microendoscopes are currectly the preferred choice to perform high resolution optical imaging in deep brain structures. GRIN micro-optics is also used in integrated devices such as miniaturized microscopes [125] for the investigation of brain activity in freely behaving animals [117], [126], [127].

1.3.2 Gradient index optics

Gradient index (GRIN) elements are components made of optically inhomogeneous materials, where the refractive index varies continuously from point to point within their volume. While in homogeneous optical elements, light is bent by curved surfaces, the optical performance of GRIN elements is determined by volumetric refractive index properties rather than surface curvature, therefore plane (instead of curved) shaped facets are used.

GRIN optics with rotationally symmetric variations of the refractive index retain most of the imaging properties characterizing homogeneous optical systems (aberration types for example). Among them, two types of GRIN media have proven to be particularly useful for optical imaging applications: axial gradients, with the refractive index varying along the symmetry axis, and radial gradients, with the refractive index varying with the distance from the symmetry axis [128], [129]. In particular, GRIN rods are cylindrical lenses with a radial (r) symmetric gradient of the refractive index $n(r)$, as depicted in Fig. 14A. They are commonly fabricated by silver ion exchange in molten salt. During this procedure, a special-glass-made rod is immersed in a molten salt bath until the glass and the bath exchange sufficient cations by diffusion to generate the silver concentration gradient corresponding to the desired refractive index modulation. Fabrication of large diameter GRIN elements is limited because of the long diffusion times required for the ion-exchange process to occur, for example, the diffusion time for a 20 mm diameter GRIN lens is about one year. On the other hand, smaller size optical elements (down to 350 μm in diameter) can be manufactured with very good optical tolerance and it is possible to obtain high optical powers with *NA* values close to 0.55 at 860 nm [130]. These features are extremely difficult to achieve with classical optically homogeneous elements, in which the thickness distribution (obtained by curved shaped facets) is used to bend light, indeed, in this case, extremely precise control is required during surface manufacturing even for spherical lenses. Another advantage of GRIN lenses is that, given their rod-like shape, they can be easily assembled in stacks to obtain longer rods with combined optical performance. Having flat facets, adjacent GRIN lenses can be directly coupled using optical glues, without the need for external frames. Moreover, GRIN lens manufacturing is cost-effective

compared with standard optical approaches, and this is of great convenience when chronic mounts [131] or disposable units are needed.

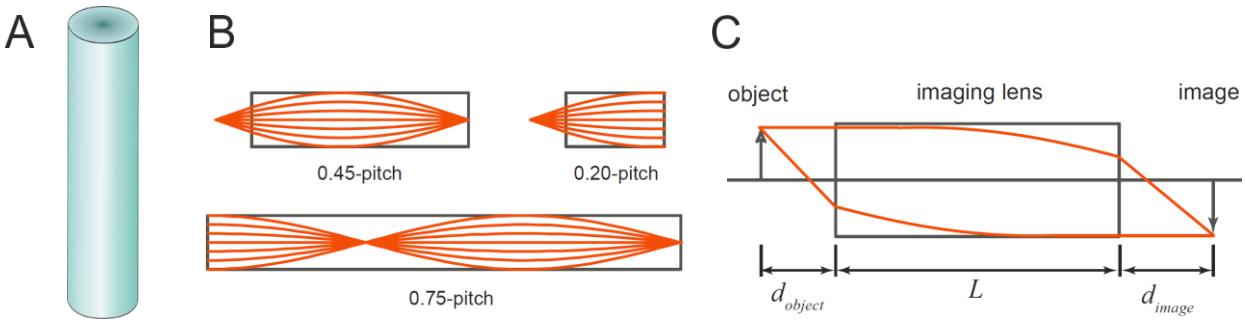

Fig. 14: Radial gradient cylindrical optical elements

A) Representation of a GRIN rod with shades proportional to refractive index. GRIN rods have a refractive index which is radially modulated: it is higher along the axis of the cylinder and it is decreasing with radial distance. Iso-index surfaces result cylindrical. B) Schematic of ray tracing inside GRIN rods of different lengths. For a given pitch P, the optical propertis of the GRIN rod are determined by its length L. The length L is indeed usually defined relative to P. The length of 0.45P of the upper-left rod makes it a finite conjugate relay lens, while the other two examples are infinite conjugate elements, because of their collimating properties. C) Working distances are defined as the distance of the object plane and the image plane from the facets of the GRIN rod.

In a GRIN rod, the radial refractive index profile follows a sech modulation of the form:

$$n(r) = n_0\, sech(gr) \qquad (10)$$

with a higher refractive index n_0 constant along the core (optical axis) of the rod and a lower refractive index $n(r)<n_0$ along radial directions through the outer surface.

The gradient parameter is defined as $g=2\pi/Z_{1P}$, where Z_{1P} is the spatial period of the sinusoidal path followed by the light beam passing through a GRIN rod. This distribution of the refractive index $n(r)$ indeed results in continuous light focusing with a sinusoidal evolution within the rod volume. Z_{1P} is also defined as the pitch (P) unit of the lens and inside the GRIN rod; a virtual image is created every half pitch (Fig. 14B).

Singlet GRIN lenses can be used as relay elements or as collimating/focusing elements (GRIN objective) according to their length relative to the pitch, as depicted in Fig. 14B. The working distance is defined as the distance between the (object or image) plane where light is focused and the proximal end of the GRIN rod (Fig. 14C). This parameter is set by the GRIN lens length L and it can be calculated in the paraxial approximation considering the relation between object and image position [132]:

$$d_{object} = \frac{tan(gL)\frac{n_{object}}{n_0} + g d_{image}\frac{n_{object}}{n_{image}}}{tan(gL) d_{image} g^2 \frac{n_0}{n_{image}} - g} \qquad (11)$$

Solving this equation for a GRIN objective ($d_{image} = \infty$), the working distance is:

$$d_{object} = \frac{n_{object}}{n_0}\frac{cot(gL)}{g} \qquad (12)$$

The constraint $d_{object} \geq 0$ (true for a converging lens) imposes that the lens length L falls in one of the intervals $(0, P/4] \cup (P/2, 3P/4]...$ and that these lenses are of infinite conjugate design. For GRIN lenses instead used as relay devices, convention sets the image plane at the face of the endoscope, $d_{image} = 0$, hence

$$d_{object} = -\frac{n_{object}}{n_0}\frac{tan(gL)}{g} \qquad (13)$$

Again, the constraint $d_{object} \geq 0$ imposes the physical condition on $L \in (P/4, P/2] \cup (3P/4, P]...$ and that these optical elements are of finite conjugate design [132].

In the case of GRIN lens-based microendoscopes for two-photon imaging, the probe is used in the relay design and is placed after the microscope objective. In this configuration, the object to be relayed by the GRIN lens is the focal point that is being scanned over the objective focal plane, and d_{object} is the distance from the objective focal plane to the first surface of the GRIN rod. The raster scanned imaging plane of the microscope is therefore relayed at the distal tip of the GRIN microendoscope at the working distance specified according to the previous equations.

Relative movement of the objective with respect to the probe results, then, in changing d_{object} and consequently d_{image}. It is in this way possible to examine more focal planes at different axial positions without moving the GRIN lens, which is particularly relevant when the probe is implanted into tissue and cannot be repositioned. However, different focal planes do not have the same imaging performance. Indeed, a translation of the object plane does not result simply in a translation of the image plane: different focal planes are characterized by different aberrations, magnifications, *NA* and field of view (FOV) sizes. Moreover, these effects become more pronounced for smaller probe diameters [132].

The *NA* of GRIN lenses depends on the maximum change in refractive index achievable during the fabrication process, while its resolving power can be determined by knowing the PSF width of the coupled microscope objective $\sigma_{microscope}$ and the PSF width $\sigma_{singlet}$ and magnification $M_{singlet}$ of the GRIN singlet with the formula [132]:

$$\sigma^2_{system} = \frac{1}{M^2_{singlet}}\sigma^2_{microscope} + \sigma^2_{singlet} \qquad (14)$$

According to this relation, high resolution is obtained by using a high-*NA* microscope objective and a high-magnification GRIN probe. An overfilling *NA* objective would improve the resolution, due to both better fluorescence excitation and better photon collection. On the other hand, relay lenses of longer pitch length have lower *NA* and hence worse resolution: this means that greater depth

penetration can be reached with long-relay GRIN lenses, but with a degradation of the system resolution.

1.3.3 Aberrations in GRIN lenses

Aberrations in GRIN optics are not just due to surface contributions. Being light rays curved inside inhomogeneous materials, wavefronts passing through GRIN lenses are affected both by monochromatic and chromatic deformations throughout the volume of the rod [128]. Also, aberrations induced by GRIN media scale with the number of pitch-lengths used to relay the image [133]. Therefore, for the same pitch, longer rods result more aberrated.

Intrinsic optical aberrations, together with low *NA* values (< 0.6), worsen GRIN lens-based microendoscopic imaging performance, in terms of spatial resolution, compared to that of conventional two-photon microscopy [123]. Moreover, unlike expensive optical components which contain many elements for minimization of aberrations over a large FOV, GRIN lenses can be corrected for on-axis aberrations, while off-axis aberrations are usually present and therefore drastically reduce the image field [134].

Different approaches have been used to compensate for GRIN lenses' intrinsic aberrations and improve imaging capability through microendoscopes, mainly by combining GRIN rods with other micro-optical elements or by compensating for aberrations with a wavefront shaping device.

For example, the combination of one highly focusing pitch rod and a long pitch relay lens results in less aberration per unit length and a magnification different from 1:1 [118], [132]. On the other hand, AO has been successfully applied to obtain diffraction-limited imaging spots over an enlarged FOV both in two-photon [134], [135] and confocal [136], [137] microscopy. Similar results were obtained by coupling specifically designed GRIN rods with high-*NA* plano-convex lenses [123], [138] (Fig. 15A), placed on the distal end of the rod and with an analogous strategy, chromatic aberrations could also be compensated for [139]. Murray adopted an even simpler strategy: he combined a GRIN rod with a coverglass and was able to balance spherical aberration by using the correction collar of the microscope objective [133]. Matz instead continued Messerschmidt's work and developed composite microendoscopes (composed by assembling up to five optical elements) optimized for one-photon imaging with sub-micron resolution, enlarged FOV and corrected for longitudinal chromatic aberration [140] (Fig. 15B) or designed for coherent anti-Stokes Raman scattering [141]. These are all examples of how combining GRIN elements with classical (or GRIN) lenses, it is possible to obtain relatively compact and high performance optical systems.

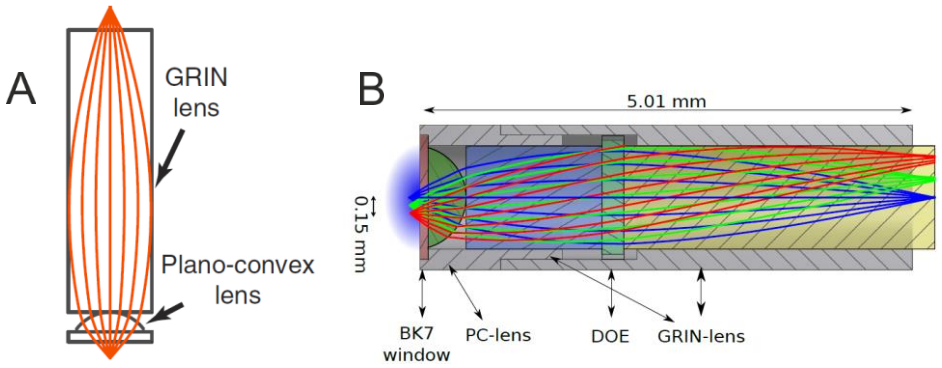

Fig. 15: Improvement of imaging performances in GRIN lens based microendoscopes

In both examples A and B, optical aberrations were successfully compensated by coupling the GRIN rod with other micro-optical elements. A) A plano-convex lens is placed on the distal end of a custom designed GRIN rod in order to obtain a high NA value in the central portion of the FOV. B) A series of micro-optical elements is combined to improve the imaging performance of the microendoscope. The optical assembly is kept aligned within a metallic cannula.

1.4 Two-photon photopolymerization

Not only fluorescence microscopy took advantage of the discovery of high-power ultrashort pulsed laser systems. The possibility to confine laser energy precisely both in time and space triggered novel technologies based on nonlinear interaction phenomena. Among them is micro-lithography and, of relevance for this work, two-photon photopolymerization (TPP) [142], [143], a new approach for 3D microfabrication with subdiffraction-limit resolution [144], [145].

TPP is based on the polymerization of a photosensitive material (photoresist) induced by two-photon absorption. Given that this process is precisely triggered only inside the 3D focal spot of the objective, and that long wavelengths can penetrate deep into the photoresist volume, it is possible to generate arbitrary volumetric structures of polymerized material within the bulk of the photosensitive medium, by 3D scanning point by point the desired shapes, as depicted in Fig. 16A. After this procedure is completed, the non-illuminated regions are washed out with a solvent (developer) and the polymerized volume remains in the prescribed 3D structure. It is in this way possible to fabricate any computer-generated 3D form by direct laser “writing” into the volume of a photosensitive material (Fig. 16B).

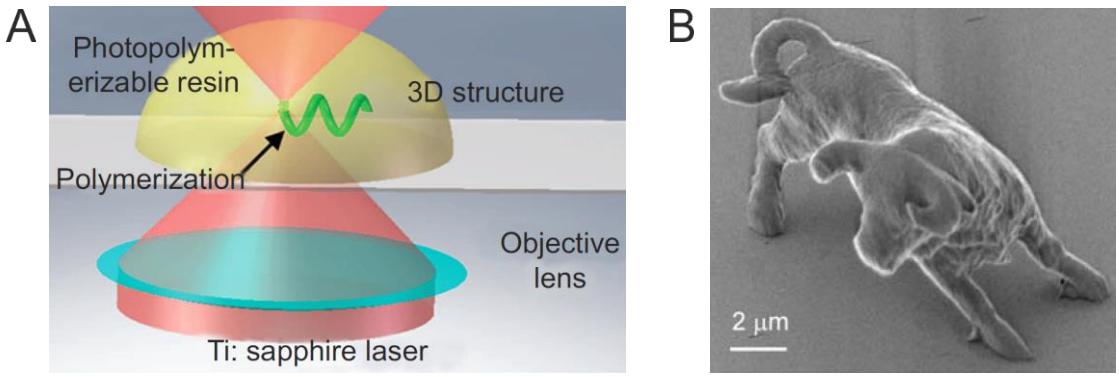

Fig. 16: Two-photon photopolymerization fabrication

A) Representation of the 3D printing process through TPP [146]*: an ultrashort pulsed laser is focused by an objective lens within a photopolymerizable resin inducing polymerization along precise 3D shapes. B) Example of microfabrication obtained with TPP: a micro bull.*

Induced polymerization has a threshold behavior and it is generated by a nonlinear process, therefore TPP can provide a resolution beyond the diffraction limit if both the laser pulse energy and the number of applied pulses per scanned position are precisely controlled. Beyond that, also highly accurate positioning systems are necessary for the correct movement of the focal spot and these limit monolithic structures to a maximum size of a few hundred μm. In this framework, usually, computer-controlled precise positioning systems are combined with a NIR light source (typically Ti:sapphire femtosecond laser with $\lambda \sim 800$ nm) to get a resolution of 100 nm or better.
There are two types of photoresist materials: negative and positive. In the former, that is the one used in this work and whose working principle was briefly described above, light exposure leads to a cross-link of polymer chains (making them insoluble to the developer), while in the latter, it is the opposite and two-photon excitation breaks those links [147]. It is therefore possible to wash out either the positive or the negative structure shaped by 3D laser scanning.
TPP is in fact an effective and inexpensive technology for the fabrication of micro-optic elements and devices that require arbitrary shape and high surface quality, among them, for example, microprism and microlens arrays, small scale diffractive optical elements or photonic crystals [148], [149]. Apart from micro-optical elements, TPP is applied also in various other fields, like microfluidics, biomedical science, dielectrics, metamaterials and so on, but to date it still remains a laboratory tool, mainly due to time consuming printing procedures, and just recently, Geng et al. combined TPP with a random access digital micromirror device scanner to speed up the fabrication process [150].

1.5 Optogenetics

To fully understand how specific neuronal populations process information and are involved, for example, in sensory perception or behavioral tasks, correlative evidence alone, provided by the readout of neuronal activity during behavior with functional imaging, is not sufficient [151]. A causal approach, in which the activity of neurons is artificially perturbed, is essential to test the function of specific neuronal networks, and understand, for example, whether they are truly carrying sensory information or driving behavior.

Perturbative interventions with high temporal precision and cellular selectivity would allow fine causal investigations of single-cell functions. Among various approaches to perturbation (e.g., pharmacological manipulation or electrical stimulation) *optogenetics* is the preferred choice in many experimental conditions because it combines cell-type specificity with high temporal resolution. Indeed, optogenetics makes use of both genetic and optical techniques to induce or prevent neuronal activity of cell-type specific subpopulations (see section 1.6) in living tissue or behaving animals with millisecond temporal resolution [152].

Optogenetics approaches in neuroscience are based on the induced neuronal expression of exogenous light-sensitive membrane proteins (*microbial opsins*) that, when stimulated with light, efficiently transport specific ions across the cell membrane [153]. Microbial opsins applied for optogenetics can be grouped in two major classes: light-gated ion pumps and light-gated ion channels. In both cases the light-triggered ion flux is generated because opsins undergo conformational changes upon light absorption, but the difference between the two classes is that while ion pumps actively transport one ion per photon absorbed, light-gated ion channels open upon illumination and passively transport ions according to their electrochemical gradient.

Opsins allow bi-directional manipulation of neuronal activity, in fact both excitatory and inhibitory opsins exist. Excitatory opsins, when illuminated, induce a depolarization of the membrane potential, hence increasing the AP firing probability, while inhibitory opsins hyperpolarize cells, therefore decreasing their spiking probability. The most used opsins in optogenetics are *channelrhodopsins* (excitatory ion channel, *ChRs*), *halorhodopsin* (inhibitory ion pump, *NpHR* or *Halo*) and *bacteriorhodopsin* (inhibitory ion pump, *BR*) [154], and a schematic representation of their function is shown in Fig. 17 (top line), together with the effect they elicit on neuronal activity (bottom line). The toolkit of available opsins has enormously expanded in recent years: engineered variants and chimeric proteins have been developed with various expression properties, cellular and subcellular localization factors, molecular kinetics, photocurrents amplitudes, light sensitivity, spectral properties and ion selectivity, in order to meet specific requests for different experimental designs [155]–[159]. For example, it is now possible to choose between light-gated ion channels

with fast closing kinetics (from ~ 4 - 10 ms) or extremely slow kinetics that require tens of minutes to close (step function opsins) unless light of a specific wavelength is administered [160]. Channelrhodopsins are cation channels that, when opened, allow passive diffusion of H^+, Na^+ and, to a lesser extent, K^+ and Ca^{2+} [161] into the cell. ChR2 is the most used channelrhodopsin and its absorption spectrum peaks near 480 nm [153], while *C1V1*, one of its variants, has a red-shifted absorption spectrum [160]. Regarding inhibitory opsins, artificial channels permeable to hyperpolarizing ions were first engineered by making channelrhodopsin selectively permeable to Cl^- ions [162], [163] and then two natural hyperpolarizing opsins with good performances were published in 2015 resulting in valid counterparts for ChR2 [164]–[166]. Halorhodopsin is a selective pump that transports Cl^- ions into the cytoplasm when illuminated (absorption peaks at ~ 580 nm) [167], while bacteriorhodopsins are selective pumps permeable to H^+ protons. The BR most used are Archeorhodopsin-3 (Arch) [168], with an absorption peak at ~ 560 nm, and one of its variants, Arch T [169].

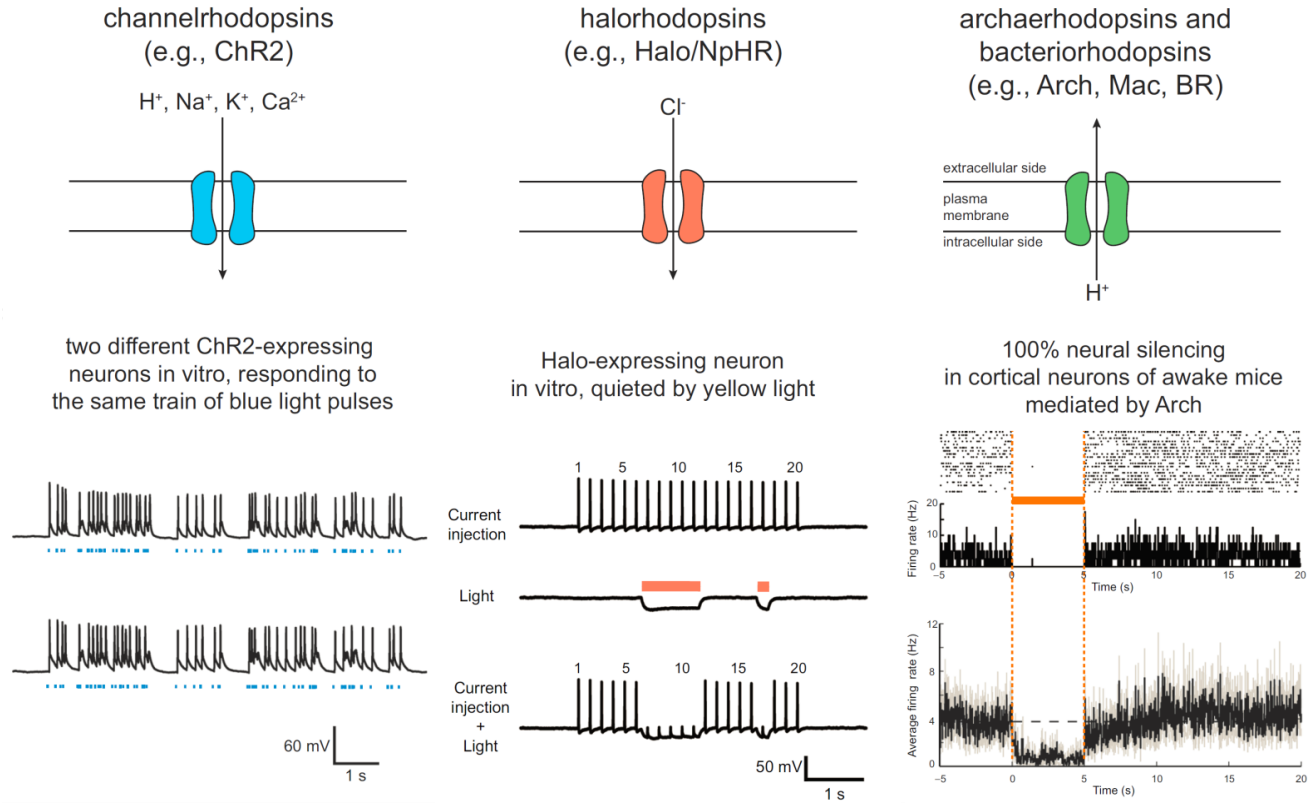

Fig. 17: Optogenetics

Below each illustration, representing ion fluxes generated by the activation of channelrhodopsin (left), halorhodopsin (middle) and archeorhodopsin (right), representative traces showing neuronal physiological responses to light-induced activation of the respective membrane proteins [154].

In most optogenetic experiments, the perturbation is performed via single-photon wide-field photostimulation [170], [171] but, with this approach, it is not possible to selectively perturb the

activity of single neurons due to the lack of illumination confinement. The simultaneous photostimulation of large neuronal populations may generate oversynchronous activities which cause non physiological results, indeed most neuronal computations are characterized by complex spatio-temporal patterns of activity distributed across neurons. Therefore, to precisely and causally test the role of neuronal activity patterns, optogenetics must be performed with cellular or subcellular resolution. Early approaches to solve this problem were based on the use of digital micromirror devices (DMDs, [172]) or computer-generated holography (CGH, [173], [174]) to confine one-photon illumination to specific regions of interest [175]. These techniques however, still lacked single-cell resolution in the case of densely packed neuronal populations, because one-photon excitation does not provide optical sectioning and, especially *in vivo*, scattering degrades spatial resolution [176]. A possible solution to improve spatial resolution in optogenetics is two-photon photostimulation. Indeed, with the same advantages offered with functional imaging, two-photon excitation is confined in subcellular volumes and improves the penetration depth in scattering tissue, allowing the causal perturbation and functional testing of specific spatio-temporal activity patterns with single-cell resolution [177].

1.6 Protein expression in specific neuronal subpopulations

Neurons can be classified according to the proteins they naturally produce and these subpopulations, which carry out different functions, appear intermingled and interconnected, form the basic components of neuronal circuits. By inducing the expression of fluorescent functional indicators and/or opsins (molecules that allow the monitoring and the manipulation, respectively, of neuronal activity) in restricted neuronal subpopulations, it is possible to investigate the role of specific cell classes in neuronal computations.

Molecular genetics technologies allow the expression of specific molecules in target neuronal subpopulations through gene delivery approaches. Selectivity with respect to neuronal subtypes is achieved by fusing the protein-coding sequence (encoding the functional fluorescent indicator or opsins, for example) with a cell type-selective promoter, which guarantees a cell-type specific transduction of the protein. The delivery of transgenes has been successfully applied to various species mainly using lentiviruses and adeno-associated (AA) viral vectors [178], leading to stable and long-term protein expression. Usually AAVs, that have been engineered with different serotypes, tropisms and various axonal transport ability, are preferred with respect to lentiviruses for safety reasons, since they are not pathogenic by themselves, and because they provoke a reduced immune response. Nevertheless, despite their widespread use, viral infections provoke an

inflammatory response that could affect regular neuronal physiology and induce brain tissue damage.

To further increase the cell specificity of protein expression, AAV transfection can be combined with site-specific recombinase technology, for example with the *Cre-loxP recombination system*. In one of the variations of this technology (used in this work and represented in Fig. 18), the protein-coding DNA sequence in the plasmid is made non-transcribable by the insertion of a blocking sequence between two *loxP* sites (*Cre*-dependent DNA sequence). The blocking sequence can be removed only by a specific molecule, the *Cre* recombinase enzyme, that is able to recognize and recombine pairs of *loxP* sites after the removal of the DNA portion between them, making in this way possible, only for those cells that express *Cre,* the production of the target protein [179]. Cell-specificity is obtained by expressing *Cre*-dependent DNA sequences under cell-specific promoters or by using transgenic mouse lines expressing the recombinase enzyme in specific neuronal populations [180]–[185]. Moreover, viral injections can be avoided by breeding transgenic *Cre*-lines with reporter lines conditionally expressing reporter genes and this method allows easy and homogeneous expression with high cellular specificity.

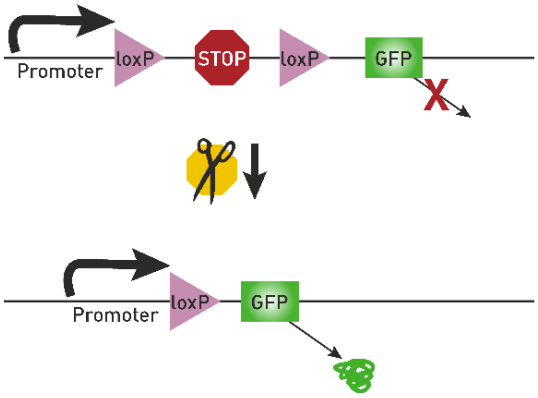

Fig. 18: Cre-loxP protein expression system

A STOP sequence is included between two loxP sites along the plasmid, before the protein-coding sequence (in the picture represented by the GFP ractangle). Only cells that are expressing cre recombinase (here depicted as a scissor) can remove the blocking sequence and complete the transcription of the protein (GFP).

1.7 Somatosensory pathway of mice whiskers system

Sensation is essential to perceive, react and interact with the environment. Indeed, through sensation and experience, living beings build their own internal representation of the outside world. Among different senses, somatosensation is responsible for touch perception, awareness of

body movement and position in space (proprioception), temperature sensing (thermoception) and recognition of potential harmful stimuli (nociception) [186]–[189].

Touch sensation is initiated by primary sensory neurons, and these cells are just the first element of a complex system that generates somatosensation. Primary sensory neurons usually have a bifurcated structure: at one end they innervate the skin with specialized sensory receptors that transduce mechanical stimuli into electrical activity [190], while the other end extends towards the central nervous system (CNS) to reach the spinal cord [191], [192]. Along the somatosensory pathway, the information continuously collected by the receptors is passed from primary sensory neurons to other stations, specifically the brainstem and the thalamus [193], before being sent to the neocortex [191]. The sensory pathway is therefore highly hierarchically organized and information is sequentially processed at different stages with specific functions. Each station receives some input information, actively integrates and shapes it, and transmits an output signal to the subsequent stage. As information ascends the hierarchy, more complex features are extracted from the sensory signals [194] and eventually, in the neocortex, where somatosensory information is further processed and combined with messages coming from other senses, as well as with signals about the internal state of the animal (attention, for example), appropriate responses are finally elaborated to guide behavior. Importantly, information not only flows forward, but it is also fed back to previous stages so that higher order stations can contribute in the lower level processing of the signal.

The work described in this thesis makes use of mice. Among animal models used for neurophysiological research, rodents have often been chosen because they are mammals (therefore sharing with humans many physiological and genetic brain features) and they can be easily handled and housed. In addition, their life cycle is very short (they reach adulthood in about 10 weeks) and they reproduce rapidly. Moreover, a wide selection of transgenic mouse lines, characterized by low genetic variability, are available to genetically target specific neuronal populations.

The whisker somatosensory system of rodents has been widely investigated in order to understand neural sensory processing, because of its behavioral relevance and its hierarchically organized structure [193], [195] . Indeed, rodents are nocturnal animals and mainly use touch perception to explore the nearby environment, especially through facial (mystacial) vibrissae, also called whiskers, whose follicles are densely innervated (through 50-200 mechanoreceptors per follicle) by primary sensory neurons [196]. Rodents explore their surroundings by whisking (“active sensing”), a process in which they rhythmically move their vibrissae back and forth at approximately 5-20 Hz by contracting muscles present in the whisker pad [197], [198]. Touch perception is thus generated by integration of motor and sensory signals and allows rodents to perceive many physical properties regarding whisker deflections, such as amplitude, direction, frequency, speed and acceleration [199]–[204], with precise spatial and temporal accuracy.

Mice have ~30-35 whiskers orderly arranged in a reticular matrix on each side of the snout [198], [205] and the whisker somatosensory pathway, represented schematically in Fig. 19A, starts with the mechanoreceptors present in the follicles, as already mentioned. Cell bodies of primary sensory neurons innervating the follicles are located in a region called the *trigeminal ganglion*, where distinct primary sensory neurons respond differently to specific mechanical stimuli, allowing single cells to encode different physical properties, like position, frequency and intensity of the stimulation [204]. Each neuron here in general innervates a single follicle, hence responds to a single whisker, and cell bodies responding to the same whisker are in proximity (spatially clustered), forming clusters responding to different whiskers that are somatotopically organized in a matrix, resembling the disposition of whiskers on the snout [195]. Primary sensory neurons then make excitatory connections in two regions within the *brainstem trigeminal complex*, as represented in the scheme shown in Fig. 19B: the *principal trigeminal nucleus* (*PrV*) and the *spinal trigeminal nucleus* (*SpV*) [195], [206], [207]. Neurons in the *PrV* mostly receive information from a single whisker and are somatotopically organized in clusters, called *barrelettes* [208]. Barrelettes are also present in the *SpV*, but here neurons have a multi-whisker receptive field (RF), because they receive information from more than one vibrissa. Three different parallel pathways depart from the brainstem trigeminal complex on their way to the thalamus. *PrV* cells mostly innervate the contralateral dorsomedial part of the ventral posterior medial nucleus of the thalamus (*dmVPM*), forming the *lemniscal pathway*. From *SpV*, cells innervating the contralateral posterior medial nucleus of the thalamus (*POm*), form the *paralemniscal pathway*, while those targeting the ventrolateral part of the VPM (*vlVPM*) constitute the *extralemniscal pathway* [195], [209].

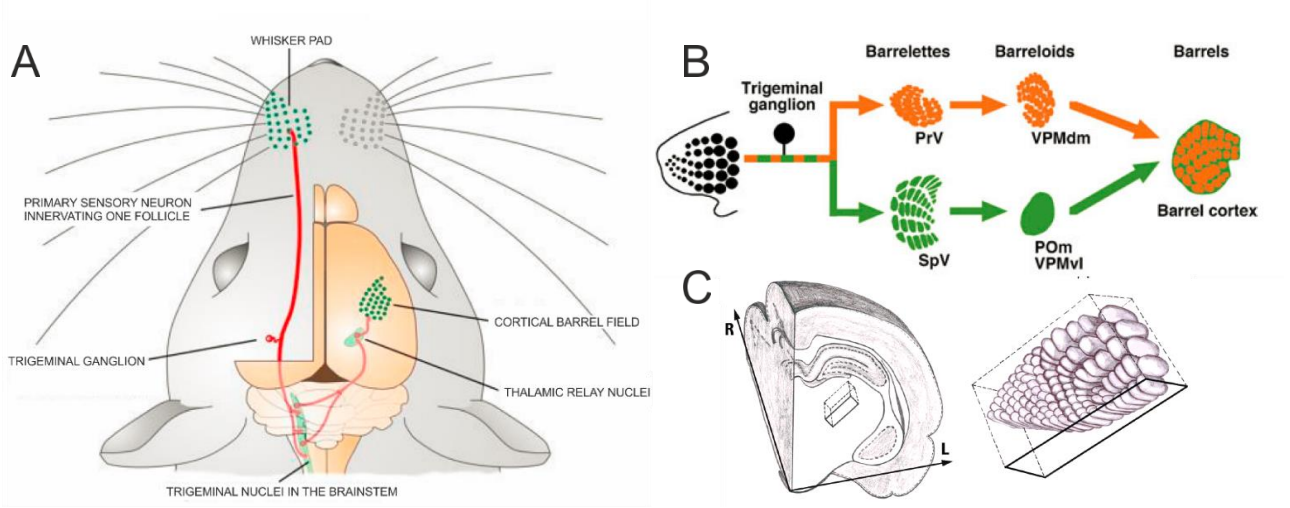

Fig. 19: Whisker somatosensory pathway

A) Schematic representation of the whisker somatosensory pathway. Each whisker follicle is innervated by many primary sensory neurons responding to whisker dynamics through mechanoreceptors. The cell bodies of primary sensory neurons are located in the trigeminal ganglion and contact different nuclei in the ipsilateral brainstem trigeminal complex, namely PrV and SpV.

Signals from here are passed to the contralateral thalamus following different parallel routes as explained in the text. Thalamus then directly contact cortical neurons in the primary whisker somatosensory area wS1. Figure adapted from [210]. *B) The various nuclei involved along the different parallel pathways connecting the peripheral sensory neurons to the cortex. In orange the barrel-related pathway (lemniscal) and in green the septum related circuit (comprehending paralemniscal and extralemniscal pathways). Figure adapted from* [211]. *C) Drawing showing the tridimensional disposition of barreloids within the thalamus* [212].

The thalamus, first considered as just a relay station [213], is the last region in which signals are actually processed before reaching the neocortex. Moreover, it is also involved in a coordinated processing of information with the cortex, through intimate interconnections forming the so-called *thalamo-cortical loop*. The main thalamic nuclei involved in whisker somatosensation are *VPM* and *POm*. As previously mentioned, they belong to different pathways and do not interact directly, suggesting that they perform different functions [195]. Neurons in *dmVPM* are somatotopically organized in clusters called *barreloids* [214], functional units that extend from the ventro-lateral to the medio-dorsal direction, as depicted in the representative drawing in Fig. 19C. Most of the neurons in barreloids have single-whisker receptive fields (typical for the lemniscal pathway) and only in the head (dorsal part) and in the tail (ventral part) of these clusters, they have multiwhisker RF. Neurons in barreloids respond both to movement of the whiskers and touch with short latencies (5-10 ms) [195] and are tuned for stimulus features like direction and velocity [215], [216]. *dmVPM* cells send axons principally to the primary somatosensory area of the neocortex (wS1), with somatotopically organized projections reaching corresponding clustered structures called *barrels* (which is why wS1 is also called the barrel cortex). Neurons in *vlVPM*, in contrast, belong to the extralemniscal pathway, mostly show multi-whisker receptive fields and convey preferentially touch information [195]. They are not somatotopically organized [217] and project both to wS1 (targeting regions between barrels called *septa*) and secondary somatosensory cortex (wS2). POm participates in the paralemniscal pathway. Here, neurons have multi-whisker RFs and are not somatotopically organized. Moreover, POm neuron responses are characterized by longer latencies, conveying information mostly related to whisker movements. They mainly target wS1 septa, wS2 and the primary motor cortex (M1) [195].

Once processed by thalamic nuclei, the somatosensory signals are transmitted to the neocortex. Here, somatosensory areas are highly organized, both anatomically and functionally, and indeed they can be subdivided horizontally in six distinct layers (or laminae, labeled with numbers) according to neuronal morphology, properties and connections. Along the somatosensory pathway, layer IV (LIV) of wS1, also named the *granular layer*, is the major recipient of thalamocortical axons and it is characterized by neuronal clustered structures called barrels. Barrel columns, that can be

defined by extending the LIV somatotopic organization vertically across all the six layers, are the main functional elements of wS1, indeed they process mainly single-whisker information through dense inter-layer intra-column specific neuronal connections. Information within barrel columns is processed sequentially across different layers [218] until deeper layers V and VI project towards other cortical areas (mainly ipsilateral S2, ipsilateral M1 and contralateral S1) or feedback signals to subcortical regions (also to the thalamus) [219] to ultimately generate specific stimulus-related behaviors.

1.7.1 Thalamic neurophysiology

In mammals, the thalamus constitutes the larger portion of the diencephalon and is situated in a central position within the brain volume. It is symmetrically divided by the mid-sagittal plane in two halves that lay at the lateral sides of the third ventricle and about 50 distinct thalamic nuclei can be classified within the thalamus according to the anatomical and cytoarchitectural properties (for example, Fig. 20A shows some nuclei that can be identified in a coronal section of the mouse brain). Boundaries between nuclei are less sharp in mice than rats and in rats than primates, however thalamic organization in mice is typical of placental animals.

All sensory pathways, except for olfaction, pass through specific thalamic nuclei before reaching their target cortical areas and this is the reason why thalamus is often defined the gateway to the cortex. Moreover, almost all cortical areas receive thalamic inputs and send back projections to the thalamus, in a highly organized fashion [220], underlying the strong interplay between these two brain regions in the processing of information.

It is worth noting that inhibitory neurons are almost absent in sensory thalamic nuclei of rodents, while this is not the case for primates. The main inhibitory thalamic inputs for mice and rats come from a particular thalamic region called the reticular nucleus (RTN), a topographically organized, shell-shaped structure that lies above the dorsolateral thalamus [221] (Fig. 20B). RTN is placed in a strategical position, in between the thalamus and cortex, so that both thalamocortical and corticothalamic axons can make excitatory synaptic contacts on RTN cells. In this way, “if the thalamus is the gateway to the cortex, RTN might be described as the guardian of the gateway” [222]. Also the structure of RTN is unusual, indeed, while local excitatory connections both within and between thalamic nuclei are usually almost absent, RTN inhibitory neurons have large collateral projections that spread extensively within the nucleus [222].

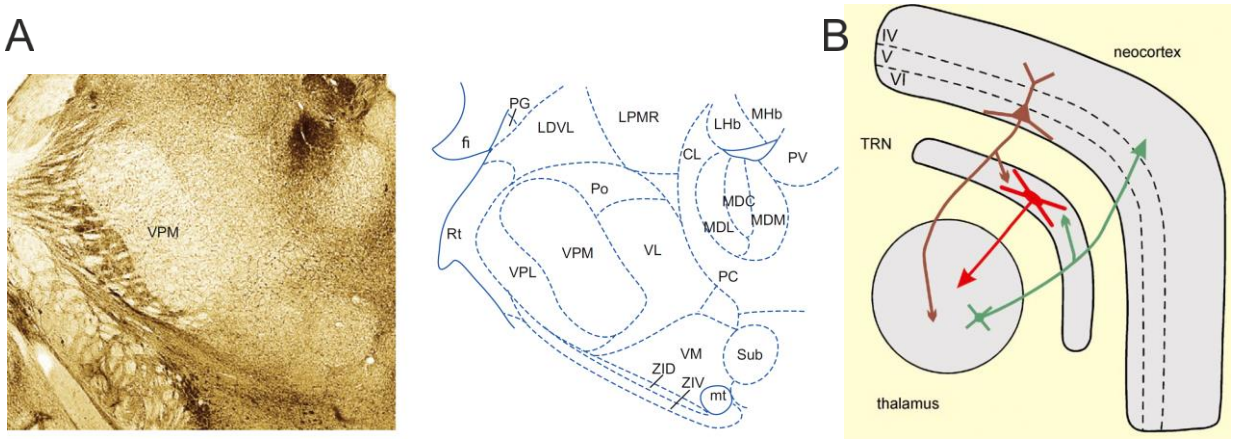

Fig. 20: Thalamic nuclei and RTN

A) Left: acetylcholinesterase stained coronal section of the thalamus of a mouse. VPM stands out, very lightly stained in comparison with neighbouring nuclei, represented graphically on the right [220]. *B) Scheme showing the anatomical disposition of thalamus, sensory cortex and RTN. Depicted is also the thalamocortical loop: feedforward messages are passed by thalamic neurons to layer IV in the cortex, while a feedback signal travel from layer VI back to the thalamus. Both thalamocortical and corticothalamic axons contact RTN neurons, that provide inhibition to the thalamus* [221].

Thalamic excitatory neurons are also called relay cells. Anatomically, they vary in size and according to their dendritic arborization can be classified as *radiate* or *bushy*. Inputs received by relay cells can be distinguished into two different types on the basis of their synaptic structure and function: *drivers*, which drive the activity patterns of postsynaptic neurons, defining their receptive fields, and *modulators*, which shape and fine-tune the activity of target neurons without altering their receptive fields [223], [224]. Drivers usually target proximal dendrites with large synapses characterized by fast ionotropic receptors, while modulators, whose signaling is mediated by slower metabotropic receptors, are mainly found on distal synapses. While the fraction of driver inputs on each relay cell is about 5-10%, the vast majority of synaptic inputs have a modulatory function and a large (30 - 44% [225]) contribution to thalamic modulatory inputs comes from excitatory neurons located in cortical deeper layer V and VI, which act as cortical feedback and close the thalamocortical loop. Other modulatory inputs are received from serotonergic, noradrenergic, histaminergic and dopaminergic neurons [226] coming from different brain regions. Thalamic nuclei can be distinguished as "*first order*" (*primary*) or "*higher order*" (*secondary*), according to the region from where they receive driver inputs. First order nuclei are those driven by ascending sensory pathways or by subcortical centers; therefore, the driver signals that first order nuclei receive have not yet been processed by the cortex. Higher order nuclei (also called *association nuclei*) receive information that has already been processed by cortical circuits, hence allowing, for example, transthalamic corticocortical communication. Regarding the rodent whisker

somatosensory pathway, VPM is the main primary thalamic nucleus, while POm, although receiving SpV inputs, is classified as higher order, because its activity is mainly driven by Layer V wS1 axons. An important feature of thalamic cells is their ability to fire APs in two distinct modalities, *tonic* or *bursting* [227] and to rapidly switch from one modality to the other, thanks to the high number of modulatory inputs that they receive. The firing modality of a neuron is determined by its state, that is the recent history of its resting membrane potential, and on a population level it has an important role in the generation of thalamocortical oscillations [228] and in the dynamic control of information processing [229]. Indeed the spiking activity induced on a neuron by the same input is completely different in the two modalities: a tonic response to a suprathreshold depolarization is characterized by a series of unitary APs while, on the other hand, depolarization leads to bursts of 2-9 high-frequency APs during bursting mode (Fig. 21A).

Burst firing is induced when the cell is depolarized by extra currents of Ca^{2+} ions, called *T-type* Ca^{2+} *currents*, I_T. These depolarizing currents flow through *T-type* Ca^{2+} *channels* that open (generating I_T) or close, when the membrane potential stays hyperpolarized or depolarized by ≥ 5 mV, respectively, with respect to the resting potential for ≥ 100 ms. T-channels are not an exclusive of thalamus, but given that they are densely expressed in relay cells, here their opening can induce relevant all-or-none depolarizing I_T currents that last until voltage dependent K^+ channels open and repolarize the cell. The dynamics underlying the transitory depolarization induced by Ca^{2+}/K^+ fluxes are much like those responsible for the common Na^+/K^+ action potential, but with two substantial differences: T-type channels operate at more hyperpolarized states (hence the name "*low threshold spikes*") and I_T has a longer refractory period, of about 100 ms, resulting in a maximum spiking occurrence of 10 Hz.

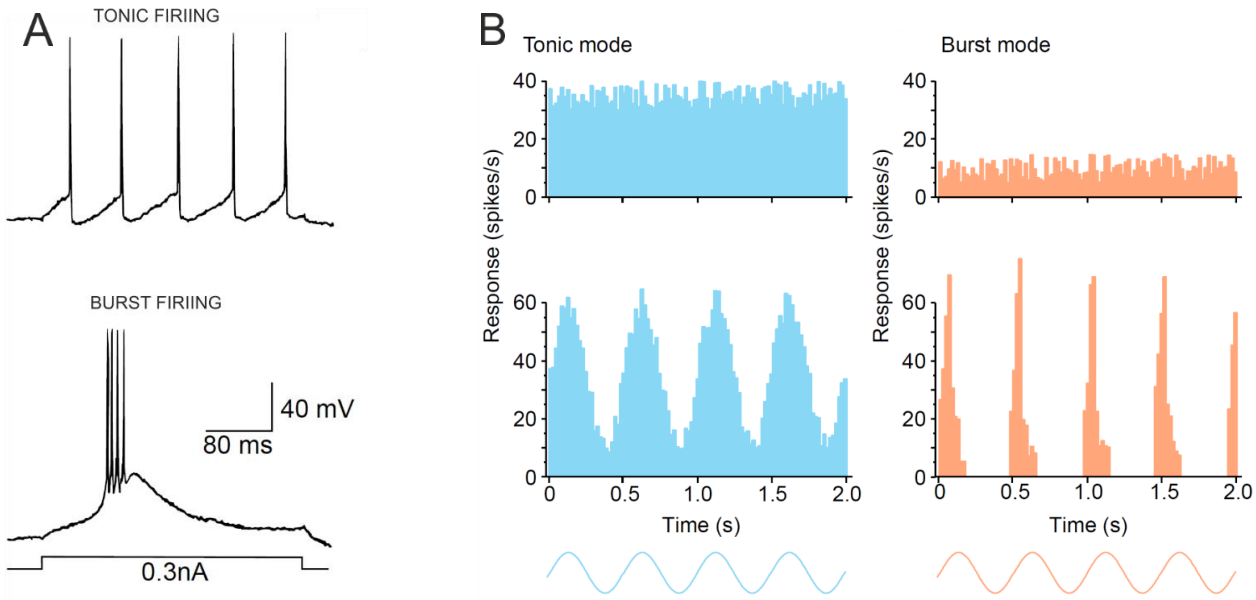

Fig. 21: Tonic and bursting firing in the thalamus

A) Tonic firing (top) and bursting firing (bottom) responses to the same depolarizing current by a neuron in the primary visual thalamic nucleus. The different firing modalities can be artificially induced by imposing different holding potentials before the stimulation. If the membrane potential has been enough hyperpolarized for at least 100 ms, the response will be a burst of action potentials. B) Average response histograms of one cell to four-cycles of drifting sinusoidal grating (lower panels) and during spontaneous activity (upper panels). In the tonic mode the spontaneous firing rate is higher and the firing rate during the presentation of the stimulus is linearly proportional to the stimulus itself. Lower spontaneous activity is recorded while the neuron is more hyperpolarized (bursting mode) and stimulated responses result nonlinear compared to the stimulus intensity.

As anticipated before, information processing and transmission is strictly related to the firing modality. While tonic responses are characterized by firing rates proportional to the depolarizing inputs, this is not true for bursting responses, where the relation between firing rate and depolarizing inputs is extremely nonlinear (Fig. 21B). Therefore, while tonic mode seems appropriate for the accurate transfer of stimulus features (relevant in case of discrimination tasks), burst mode has been hypothesized to encode more salient messages (relevant in a context of stimulus detection) [222], [228], [230]. Indeed, although the peak stimulus-induced firing rate is quite similar for the two modalities, the lower spontaneous activity during bursting mode results in a higher SNR. Moreover, the long refractory period underlying bursts of APs would overcome the pair-pulsed depression characterizing most of the thalamocortical synapses, generating stronger inputs to the cortex, which could be useful for example to report relevant changes in the environment that require a shift in attention, namely a “wake up call” [231].

1.7.2 Ventral posteromedial thalamic nucleus (VPM)

As already mentioned, the VPM is the first order thalamic nucleus for the whisker somatosensory pathway. More relevant for this study is the dorsomedial part of the VPM, the thalamic stage involved in the lemniscal pathway, in which excitatory relay cells cluster somatotopically in discrete barreloids corresponding to processing units for single-whisker information. In general, neurons clustered together innervate a single barrel in wS1, suggesting separated labeled-line coding of whisker-specific signals along the lemniscal pathway [200]. Nevertheless anatomical substrates for cross-whisker modulation between barreloids have been found [232], [233] and relay cells with multiwhisker receptive fields located in the head of barreloids have been found to project in the septal regions within wS1 [234].

Given the strong bidirectional connection between thalamus and cortex, changes in thalamic activity massively contribute to changes in cortical state while the cortex has a dominant role in thalamic information processing. In particular, dmVPM projections to Layer IV wS1 are the major driver of barrel cortex, indeed VPM AP firing is the main factor responsible for the generation of the desynchronized cortical state that is typical of active behavior [235] and corticothalamic feedback axons are precisely shaping the response properties of relay cells [225], [236], [237]. Moreover, neural activity in dmVPM is dynamically modulated by behavioral states in awake mice [238]. Urbain et al. showed that membrane potentials become more depolarized and AP firing increases during active wakefulness (defined according to LFP and EEG recordings) compared to resting states (Fig. 22A). Firing rate is strongly increased, especially during active periods characterized by a desynchronized LFP trace and free whisking in air (Fig. 22B). Furthermore, the probability of burst events is higher in this behavioral condition.

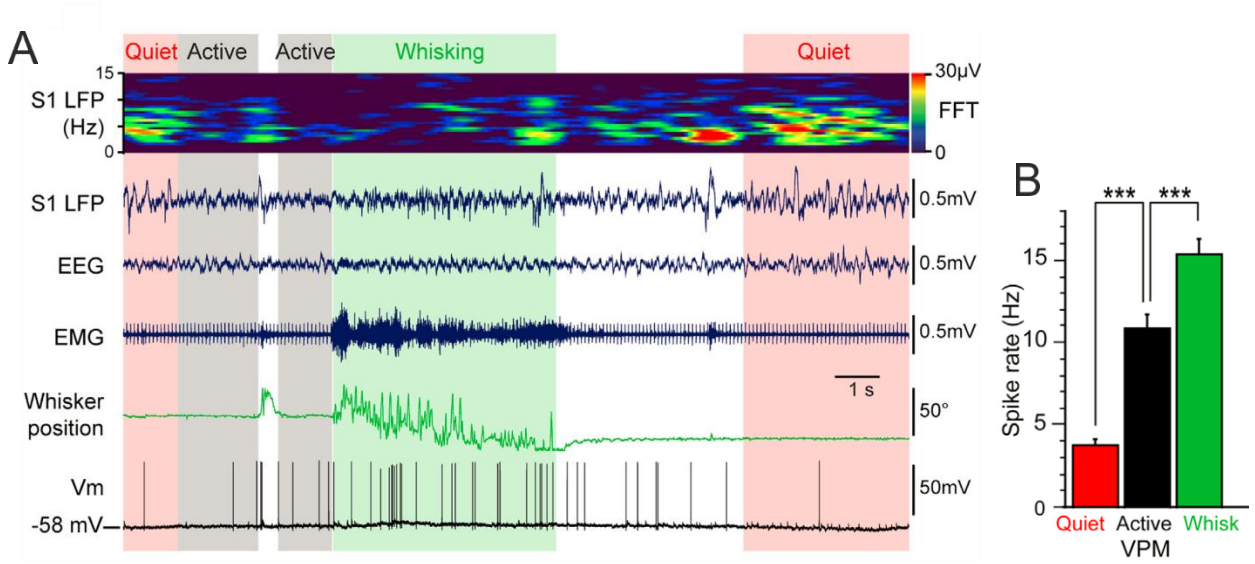

Fig. 22: Modulation of VPM electrophysiological activity by behavior

A) Aligned recording of LFP in wS1, EEG, EMG, whisker position and membrane potential of a VPM cell. Quiet, active and whisking periods were classified according to the LFP trace and the whisker position. Firing rate is strongly increased in active periods, especially while whisking [238]. *B) Mean firing rate extracellularly recorded from VPM cells* [238].

Nonetheless, thalamic nuclei consist of a heterogeneous set of specialized cells [216]; some dmVPM neurons exhibit spiking rates that are phase-locked to the whisking cycle. Such a firing modulation would encode the position of the vibrissae precisely, which is fundamental information for active sensing. Other than whisker movements, neurons belonging to the lemniscal pathway are also responsive to touch stimuli. Indeed, touch either adds or subtracts spikes from the free whisking response [239]. The potential ambiguity resulting from the mixed encoding of position and touch by single neurons could be resolved then by a nonlinear input-output neuronal relation in the cortex, providing the correct separation of the two types of information [240]. Moreover, despite that different subpopulations of neurons have been identified within single barreloids [241], it is still unknown if neurons more responsive to whisker movements or touch are spatially organized. Combined whisking and touch signals in relay cells are hypothesized to involve processing of object identity and indeed diverse stimulus features are encoded by individual cells that are sparsely distributed within the dmVPM neuronal population. Therefore, while the dominant mode of communication with the cortex has to date been assumed to be one with most relay cells synchronously activated [242], the great majority of dmVPM neurons have been proven to be selectively sensitive to specific and diverse kinetic features, such as position, velocity or acceleration, with a few of them conveying information about multiple features [243]. In this scenario, while whisking on objects, different kinetic features are sensed at different times and dmVPM cells sensitive to the corresponding features respond independently at different times.

Indeed, synchronicity between relay neurons is stimulus-dependent and is smaller for smooth whisker movements [242]. In fact, at the population level, dmVPM responses have been defined as “dynamically synchronous”, meaning that the same event at different times can elicit different sparse patterns of synchronous activity between neurons [244]. Therefore information processing within barreloids is characterized by a temporally sparse activation of spatially distributed neuronal ensembles that encode specific information about whisker motion and touch through a code that is dynamically modulated by behavior.

2 Rationale and aim

Over the last 20 years, methods of optical brain imaging have rapidly advanced and emerged as increasingly powerful means for cellular-level recordings in behaving animals. Fluorescence light imaging, combined with exogenous optical contrast agents has become extremely useful for the anatomical and functional study of live neurons, especially in vivo, thanks to the development of novel microscopy techniques, new vital fluorophores, viral vectors, and transgenic methods for specific gene delivery. However, one of the main drawbacks of optical methods for investigating the brain is tissue scattering, which limits both penetration depth and imaging resolution. Among the wide range of optical imaging techniques, two-photon laser scanning microscopy has become the preferred tool for imaging intact biological specimens. Compared to single-photon imaging, the main advantages of multiphoton microscopy are the intrinsic optical sectioning capability, which reduces out-of-focus photobleaching, photodamage and scattered light contamination, and the longer penetration depth, due to the longer wavelengths that are used in two-photon imaging, which are less sensitive to tissue scattering. Two-photon microscopy is currently widely used in neuroscience and provides high-resolution anatomical and functional information of cellular structures laying several hundred microns within biological tissue. However, light scattering still imposes strong depth limitations and restricts the applicability of this technique to deeper (> 1.5 mm) brain regions.

The strong interest in investigating the activity of neuronal populations buried deep within cerebral tissue prompted the development of microendoscopy. Microendoscopes are light guides that are directly inserted into tissue and allow imaging at their distal end. Ideally, microendoscopes should be optimized in terms of both optical performances and physical size, in order to guarantee good imaging capability over a wide area with a limited invasiveness. Gradient index (GRIN) lens-based implantable microendoscopic probes have been widely used to date to perform one- and two-photon fluorescence microscopy in otherwise inaccessible brain regions. GRIN lens-based endoscopes are characterized by diameters in the range of 0.3-1.5 mm and they allow functional and morphological imaging. However, they are characterized by small *NA* values and moreover, their imaging performance is limited by intrinsic aberrations. Therefore, laser scanning microscopy through GRIN lens-based microendoscopes still underperforms imaging with conventional macro-

objectives in terms of image quality and resolution. GRIN probes suffer for the presence of different kinds of aberrations, both on-axis and off-axis, both types limiting their field of view and degrading the spatial resolution. Increasing *NA* values and correcting aberrations are thus two essential steps to improve the efficiency of excitation and collection of signal photons while preserving images' fine structure.

Two different strategies have been efficiently used to improve the imaging performances of GRIN microendoscopes. On one hand, compound microendoscopes, made of a cascade combination of a GRIN lens and other optical parts (such as plano-convex spherical lenses or diffractive optical elements) have been assembled. Compound microendoscopes are characterized by high *NA* values on-axis and hence provide good imaging performances in term of resolution, but they have a small FOV compared to their outer diameter, which is typically larger than 1 mm. Indeed, technical limitations in manufacturing high-precision optics with small lateral dimensions have, so far, prevented improvements in the performances of GRIN microendoscopes with lateral diameter < 1 mm using corrective optical microelements. On the other hand, adaptive optics (AO) has been applied in order to shape the imaging light wavefront and cancel out the deformations induced by aberrations. In this case, smaller probes can be used and both intrinsic and sample-induced aberrations are corrected, but adaptive optics is a complex technique that requires an extensive modification of the microscope hardware and software. Moreover, under many experimental conditions, AO requires a significant amount of time to measure the deformations of the wavefront, limiting the temporal resolution of the imaging system.

The goal of the work described in this thesis was to develop and apply a new generation of aberration-corrected microendoscopes. Ready-to-use probes with built-in aberration correction would allow imaging in large areas of deep brain regions with homogeneous resolution and without the need to remove significant portions of the overlying tissue. To optimize the extension of the FOV compared to the endoscope size, while maintaining a minimally invasive probe dimension, small diameter (350 µm or 500 µm) GRIN lenses were combined with custom corrective aspheric microlenses generated by two-photon photo-polymerization (TPP), a lithography technique that allows the fabrication of accurate 3D elements at such small scales. This method has no limitations on the size of the corrective lenses for current GRIN-based microendoscopes (diameter 0.3-0.5 mm) and required no modification of the microscope optical path. We designed, fabricated, and characterized these aberration-corrected microendoscopes and validated them by imaging VPM neurons in anesthetized and awake head-fixed animals.

3 Materials and methods

3.1 Optical design and simulation

Simulations were run with OpticStudio15 (Zemax, Kirkland, WA) to define the profile of the aspheric corrective lens to be integrated in the aberration–corrected microendoscopes, with the aim to achieve: i) a full-width half maximum (FWHM) lateral resolution < 1 μm at the center of the FOV; ii) a FWHM axial resolution below < 10 μm; iii) a working distance between 150 μm and 220 μm into living brain tissue. The wavelength used for simulations was λ = 920 nm since the devices were developed for two-photon functional microscopy applications using GCaMP6s [61].

The surface profile of corrective aspheric lenses has been described as [245]:

$$Z(r) = \frac{cr^2}{1+\sqrt{1-(1+k)c^2r^2}} + \sum_n \alpha_n r^{2n} \qquad (15)$$

Since GRIN lenses have intrinsic spherical aberration, the optimization for the shape of the corrective lenses started with the profile of a Schmidt corrector plate [92] as initial guess; the parameters c, k, α_n (with n = 1-8) in equation *(15)* were then automatically varied in order to maximize the Strehl ratio over the largest possible area of the FOV (Table 2). A fine manual tuning of the parameters was performed for final optimization.

	c	**k**	**α1**	**α2**	**α3**	**α4**	**α5**	**α6**	**α7**	**α8**
Type I	-2.58E-01	-1.74E+00	8.58E-01	-5.30E+01	5.95E+03	-2.77E+05	7.26E+06	-8.91E+07	2.47E+08	2.19E+09
Type II	1.02E+03	-2.37E+03	-1.46E+00	2.87E+01	-4.60E+01	-7.69E+03	1.96E+05	7.82E+06	-1.69E+08	-3.88E+08
Type III	-4.99E-01	8.20E+00	1.54E+00	-1.35E+02	3.67E+04	-3.92E+06	2.17E+08	-5.56E+09	3.34E+10	6.29E+11
Type IV	-2.41E-01	-1.17E+00	9.22E-01	-1.34E+02	4.36E+04	-4.28E+06	2.23E+08	-5.55E+09	3.48E+10	4.94E+11

Table 2: Coefficients for the aspheric corrective microlenses.

Coefficients used in equation (15) for the aspherical corrective lenses used in type I-IV enlarged field of view (eFOV) microendoscopes.

3.2 Corrective lens manufacturing and endoscope assembly

The optimized aspheric lens structure obtained with simulations was exported into a 3D mesh processing software (MeshLab) and converted into a point cloud dataset fitting the lens surface

(with ~ 300 nm distance among first neighborhood points). Two-photon polymerization with a custom set-up [149] including a dry semi-apochromatic microscope objective (LUCPlanFLN 60x, NA 0.7, Olympus Corp., Tokyo, JP) and a near infrared pulsed laser beam (duration, 100 fs; repetition rate, 80 MHz; wavelength, 780 nm; FemtoFiber pro NIR, Toptica Photonics, Graefelfing, DE) was used for the fabrication of the corrective lenses. A drop of resin (4,4'-Bis(diethylamino)benzophenone photoinitiator mixed with a diacrylate monomer), sealed between two coverslips, was moved by a piezo-controlled stage (model P-563.3CD, PI GmbH, Karlsruhe, DE) with respect to the fixed laser beam focus, according to the 3D coordinates of the previously determined point cloud, with precision of 20 nm. Output laser power was ~ 15 mW at the sample. Once the surface was polymerized, the lens was dipped for ~ 2 minutes in methanol followed by ~ 1 minute immersion in isopropyl alcohol, and finally exposed to UV light (λ = 365 nm; 3 Joule / cm^2) to fully polymerize the bulk of the structure. In the second stage of the project, a commercial TPP fabrication system (Photonic Professional GT, Nanoscribe GmbH, DE) was also used for corrective lens fabrication.

For fast generation of multiple lens replicas, a molding [246] technique was used. To this end, polydimethylsiloxane (PDMS, Sylgard 164, 10:1 A:B, Dow Corning, Auburn, MI) was casted onto the lens and hardened by heat cure in a circulating oven at 80°C for approximately 30 minutes. The resulting bulked structure of solid PDMS was then used as negative mold. A drop of a UV-curable optically-clear adhesive with low fluorescent emissivity (NOA63, Norland Products Inc., Cranbury, NJ) was deposited on the negative mold, pressured against a coverslip (5 mm diameter) of appropriate thickness (100-200 μm thick depending on the enlarged field of view (eFOV) microendoscope type, Fig. 23) and hardened by UV exposure. The coverglass with the lens attached was detached from the mold and glued onto a metal ring. One end of the appropriate GRIN rod (NEM-050-25-10-860-S; NEM-050-43-00-810-S-1.0p; GT-IFRL-035-cus-50-NC; NEM-035-16air-10-810-S-1.0p , all purchased from Grintech GmbH, Jena, DE) was attached perpendicularly to the other surface of the coverslip using NOA63. Alignment of the corrective lens and the GRIN rod was performed under visual guidance using an opto-mechanical stage (Fig. 26A-B). An additional and removable coverglass or a silicone cap (Kwik-Cast Sealant, World Precision Instruments) was glued on the top of every support ring (Fig. 26D-E) to keep the polymeric corrective lens clean and to protect it from mechanical damage.

3.3 Optical characterization

Optical characterization of eFOV-microendoscopes was carried out with a two-photon laser-scanning microscope equipped with a wavelength-tunable, ultrashort-pulsed, mode-locked Ti:Sapphire laser source (Ultra II Chameleon, pulse duration, 160 fs; repetition rate, 80 MHz;

wavelength, 920 nm; Coherent Inc., Santa Clara, CA) and a commercial Prairie Ultima IV scanhead (Bruker Corporation, Milan, IT, former Prairie Technologies). For all measurements, the wavelength was set at 920 nm. The optomechanical assembly used for the microendoscope characterization is shown in Fig. 26C. Two infinity-corrected objectives were used: EC Epiplan-Neofluar 20x, 0.5NA (Zeiss), and LUCPLFLN 60X, 0.7NA (Olympus). Measurement of maximal on-axis resolution was performed with the LUCPLFLN 60X objective to overfill the eFOV-microendoscope numerical aperture and reach diffraction limited performances in accordance with optical simulations, whereas other characterizations were done with the 20X objective. Spatial resolution of each microendoscope was evaluated using subresolved spherical fluorescent beads (diameter: 100 nm, Polyscience, Warrington, PA), following a previous spatial calibration using a custom fluorescent ruler (Motic calibration slide). The same ruler was used as a reticular grid to evaluate the distortion of the FOV. To appreciate the curvature of the imaging field, thin (thickness: 300 nm) fluorescent slices [247] were used. Fluorescent samples were deposited on a microscope slide and imaged through the endoscope assembly aligned to the microscope objective, with or without the corrective microlens above the coverslip, using the coupling apparatus described in Fig. 26C. Imaging was performed with the distal end of the GRIN rod immersed in a droplet of water placed on the slide. The distance between the focal plane of the microscope objective and the endoscope assembly was 100 μm and it was fixed for all measurements. Given the imaging field curvature of endoscopes, for both the ruler and the thin fluorescent slices (planar samples), the acquisition of z-series of images (512 pixels x 512 pixels, with 1 μm axial step) was necessary.

Analysis of thin fluorescent film acquisitions

Image analysis was carried out using the ImageJ/Fiji software and custom Python code. In x,z projections, we first fitted the fluorescence intensity profile with a circular section. We then averaged the fitting circular section across x,z projections obtained from different z-stacks for the same GRIN rod and finally measured the mean curvature of the FOV of that specific GRIN rod from the average circular section. The axial projection of each z-stack was remapped onto the fitting circular section to optimally estimate radial distances. For fluorescence intensity measurements, in each z-stack we measured the fluorescence intensity along N randomly chosen radial directions (N = 400). Fluorescence intensity along a given direction was initially smoothed with a ~7 μm flat moving window, averaged across N and normalized to the maximal intensity value.

Measurement of distortion and calibration of the pixel size

To measure the distortion in the FOV, we imaged a regular fluorescent grid spanning the FOV. We measured the number of pixels necessary to span 10 μm in the x and y direction as a function of the distance from the FOV centre. We then computed the ratio between the measured number of pixels

and the calculated number of pixels based on the expected resolution provided by the acquisition system. This ratio provided a magnification factor which varied along the radial direction. We fitted the estimated magnification factor (from x and y direction) using a linear and a quadratic curve. The quadratic curve gave the best fit both for the corrected and uncorrected endoscopes (corrected: p0=0.76, p1= -6.24e-04, p2= 1.95e-05, norm of residuals = 1.78. Uncorrected: p0=0.73, p1= -2.91e-04, p2= 8.11e-06, norm of residuals = 0.24).
We used the estimated magnification factors for the generation of synthetic data and for the analyses of experimental data. In this last case, we corrected the position of the ROIs centres and the estimated size of the ROIs.

PSF on- and off-axis

In order to characterize imaging quality over the FOV, z-stacks of 100 nm Y/G fluorescent beads were taken at different distances from the optical axis.
For off-axis measurements, given that beads are lying on a planar surface while the FOV is a concave upward surface, laser power and GRIN-sample spacing were varied to have beads on focus at different radial distances from the optical axis. These distances were then measured taking into account the varying pixel size due to the distorted FOV.

Intensity profiles obtained from sections in x, y, z directions of the PSFs were fitted with Gaussian curves and their FWHM was respectively defined as x, y and z resolution. Transverse resolution is calculated as the average of x and y resolution, considering the varying transverse magnification present at different positions in the FOV, while the axial one is the FWHM of z resolution. In cases in which the axial intensity profile, due to aberrations, was better fitted with a sum of two Gaussian curves instead of a single one, the axial resolution was defined as the axial distance between the two peaks of the best fitting curves. For each group of measurements at a specific distance from the optical axis, outliers were identified using the Rout method (GraphPad Prism 6) and excluded from the dataset. Mean and standard deviation of resolution were plotted against radial distance (Fig. 28). Data were fitted with a symmetric quartic function to respect the cylindrical geometry of the optical system and the maximal FOV radial extent was determined as the radial distance at which the axial resolution fitting curve crossed a 10 μm threshold. PSF on- and off-axis analysis were conducted using three endoscopes per type.

3.4 Animal surgery, viral injection and microendoscope implant

Experimental procedures involving animals have been approved by the Istituto Italiano di Tecnologia Animal Health Regulatory Committee, by the National Council on Animal Care of the Italian Ministry of Health (authorization # 1134/2015-PR) and carried out according to the

guidelines of the European Communities Council Directive. Animals were housed under a 12-hour light:dark cycle in individually ventilated cages. Experiments were performed on adult (8-10 week old) C57BL/6J (Charles River, Calco, IT), and Scnn1a-Cre (B6;C3-Tg(Scnn1a-cre)3Aibs/J, Jackson Laboratory, Bar Harbor, USA) mice. Adeno-associated viruses (AAVs) AAV1.Syn.GCaMP6s.WPRE.SV40, AAV1.Syn.flex.GCaMP6s.WPRE.SV40, AAV1.CAG.Flex.eGFP.WPRE.bGH, AAV1.CaMKII0.4.Cre.SV40 were purchased from the University of Pennsylvania Viral Vector Core. Viral injections and aberration-corrected microendoscopes insertion were performed during a single surgical procedure. Animals were anesthetized with 2% isoflurane, placed into a stereotaxic apparatus (Stoelting Co, Wood Dale, IL) and maintained on a warm platform at 37°C. A small hole was drilled through the skull and 0.5 - 1 µl (30 - 50 nl/min, UltraMicroPump UMP3, WPI, Sarasota, FL) of AAVs containing solution was injected at stereotaxic coordinates: 1.4 mm posterior to bregma (P), 1 mm lateral to the sagittal sinus (L) and 1 mm deep (D) to target the hippocampal CA1 region; 1 mm anterior to bregma (A), 2 mm L and 2 mm D to target the dorsal striatum; 1.7 mm P, 1.6 mm L and 3 mm D to target the ventral posteromedial thalamic nucleus (VPM). Co-injection of AAV1.Syn.flex.GCaMP6s.WPRE.SV40 and AAV1.CaMKII0.4.Cre.SV40 (1:1) was performed to express GCaMP6s in hippocampus CA1 pyramidal cells. Injection of AAV1.Syn.GCaMP6s.WPRE.SV40 was performed to express GCaMP6s in the dorsal striatum. Injection of AAV1.Syn.flex.GCaMP6s.WPRE.SV40 in the Scnn1a-Cre mouse line was performed to express GCaMP6s in the VPM. Layer IV expression of GFP was achieved by injecting AAV1.CAG.Flex.eGFP.WPRE.bGH in the somatosensory cortical area of Scnn1a-Cre mice. Following virus injection a craniotomy (~ 600 x 600 μm^2 or ~ 400 x 400 μm^2 depending on the endoscope size) was performed over the neocortex at stereotaxic coordinates: 1.8 mm P and 1.5 mm L to image the hippocampus; 0.7 mm A and 1.8 mm L to reach the dorsal striatum; 2.3 mm P and 2 mm L to reach the VPM. A thin column of tissue was suctioned with a glass cannula (inner diameter = 300 µm, outer diameter = 500 µm; Vitrotubs, Vitrocom Inc., Mounting Lakes, NJ) and the microendoscope was slowly inserted in the cannula track, using a custom holder, down to the depth of interest and secured by acrylic adhesive and dental cement to the skull. If necessary, metal spacers (thickness: ~ 100 µm) were glued on the flat coverslip surface to obtain the desired protrusion distance of the GRIN rod. After surgery, animals were positioned under a heat lamp and monitored until recovery.

To evaluate how much both thalamocortical (TC) and corticothalamic (CT) connections were affected by the surgical operations performed during the implant of GRIN lens endoscopes, Scnn1a-Cre mice were injected, after tissue suctioning, at 100 nl/min with flex-GFP virus and red retrobeads (diluted respectively 1:2 and 1:8 in saline solution, 250 nl total volume) in VPM.

3.5 Functional imaging with eFOV microendoscopes in vivo

For experiments in anesthetized mice, three to five weeks after injection, mice were anesthetized with urethane (2 g/kg) and placed into a stereotaxic apparatus to proceed with imaging experiments. Body temperature was kept at 37 °C and depth of anesthesia was assured by monitoring respiration rate, eyelid reflex, vibrissae movements, and reactions to pinching the tail and toe. In some experiments, oxygen saturation was controlled by a pulseoxymeter (MouseOx, Starr Life Sciences Corp., Oakmont, PA).

For experiments in behaving mice, imaging was performed 2-4 weeks after the endoscope implant, after 7-10 days of habituation, in which mice were placed daily on the set up, each day for a longer time duration, up to 45 minutes. During experiments, 5 minutes of recording sessions (performed with frame rate ~ 3 Hz) were interleaved by 5 minutes of pause in which no imaging was performed. Mice were always allowed to run spontaneously on the wheel. For scanning imaging of GCaMP6-expressing neurons, the same microscope set-up used for the optical characterization of eFOV-microendoscopes was used. GCaMP6 fluorescence was excited at 920 nm (laser power measured after the objective: 28-90 mW).

Initially, for validation experiments, temporal series recorded in the scanning configuration were imported into the open source ImageJ/Fiji software and movement correction was performed using the plugin Image Stabilizer. Calcium traces were analyzed using a custom code based on the open-source CellSort MATLAB toolbox [248]. Briefly, the motion-corrected image stack was normalized and analyzed by principal components analysis (PCA) to find and discard dimensions that mainly represented noise. Principal components displaying a variance greater than noise were then analyzed with an iterative independent component analysis (ICA) algorithm to identify active cells. Manual validation of extracted traces was performed. Signals $S_i(t)$ were standardized as $S_{\sigma,i}(t) = \frac{(S_i(t) - \overline{S_i})}{\sigma(S_i)}$, where $\overline{S_i}$ and $\sigma(S_i)$ are respectively the mean of the signal and its standard deviation (s.d.).

For experiments in VPM we upgraded our analysis pipeline. We developed a graphical user interface (GUI) in Matlab (version R2017A) for the preprocessing of the recorded time series. The GUI enable the loading of data saved in TIFF format (both multi-page and sequences of single files) or already pre-processed .mat files. Upon data loading, the GUI stored in a data structure information relative to the acquisition. Information automatically saved in a .xml file generated from the acquisition software included: size of the FOV in pixels, microns to pixels conversion factor, acquisition rate, and dwell time.

In the main window of the GUI, the acquired data could be visualized scrolling through the single frames. In case of motion artefacts, we included in the GUI the motion correction algorithm described in [249] and provided at https://github.com/flatironinstitute/NoRMCorre. Rigid

correction and non-rigid correction of the acquisition could be performed. For further details about the correction procedure, see [249]. After the optional motion correction step, segmentation of the FOV was performed. To this aim, a new window is used, where it could be simultaneously visualized the average (or dynamic range = max-min) temporal projection of the FOV (projection time window length = 1 s) and single frames. In order to draw a ROI, a bounding box around the ROI could be positioned or the contour of the ROI could be manually drawn. In the second case, an ellipse was fit to the borders of the cell body of the target neuron. Pixels in the bounding box (or in the ellipse) were sorted according to their intensity in a time interval around the visualized frame ([-0.4 s, 1 s]) and only those pixels necessary to maximize the peak-signal-to-noise ratio of the mean intensity were selected. Peak-SNR was defined as $peakSNR = \frac{\max_{t\in[\hat{t}-\delta t,\hat{t}+\delta t]} f(t)-avg(f_{baseline})}{std(f_{baseline})}$, where $f_{baseline}$ was defined as the portion of intensity trace lower than the 25th percentile of the intensity distribution. The intensity trace and the peak-SNR as a function of the selected pixels number could be visualized. After ROIs segmentation, the spatial footprints of the ROIs were saved in a matrix A of size [n_px]x[n_ROIs]. Each column of this matrix corresponded to a single ROI and contained zeros for pixels that did not belong to the ROI and the temporal average intensity for pixels belonging to the ROI. The raw fluorescence intensity of the segmented ROIs was stored in a matrix F_{raw} of size [n_ROIs]x[n_frames]. Each row of this matrix corresponded to a single ROI and contained the temporal course of the mean intensity across pixels belonging to the ROI. The users can then choose to optionally extract the normalized calcium activity. In this case, we used the algorithm provided by [250] (https://github.com/flatironinstitute/CaImAn-MATLAB) to perform the deconvolution of calcium activity from the fluorescence. The algorithm was based on the fit of the fluorescence activity with an autoregressive order. We used models of order 1 if the acquisition rate was low (<2Hz), of order 2 otherwise. For further details about the deconvolution algorithm, see [250]. The normalized calcium activity of the ROIs was saved in a matrix Cdf (calcium-delta fluorescence) of size [n_ROIs]x[n_frames].

At the end of the pre-processing, a structure was saved containing all the extracted information: acquisition parameters, ROIs spatial footprints, ROIs fluorescence activity, ROIs deconvolved normalized calcium activity (optional). This structure was used for the subsequent analyses.

3.6 Behavioral traces extraction and raw data binarization

Whiskers mean angle

Movements of the whiskers in the whisker pad contralateral to the surgery were imaged with a CMOS camera (Basler acA800) directed through a 45° inclined mirror placed below the whiskers with a sampling frequency of 150 Hz. Illumination was provided by a circular array of infrared LEDs

(emission wavelength 800 nm) fixed to the microscope objective and aligned to the whiskers and the mirror below them. A diffusive Teflon film was used to obtain a homogeneous background intensity. With this configuration most of the whiskers (especially the portion near the follicle) were imaged and resulted black on a white background. Videos of whiskers were binarized with ImageJ Ridge Detection plugin in order to individuate pixels corresponding to whiskers. These videos were then processed in Matlab to extract the whiskers mean angle signal and to binarize it into whisking periods: all the whiskers were fitted with straight lines and for each frame the mean angle of all the lines was calculated respect to the horizontal direction of the field of view. Once the mean angle of the imaged whiskers was calculated for each frame, this signal was processed with two operations: a moving standard deviation over a 400 ms window and Gaussian filter over a 50 ms window were subsequently applied. The binarization of the signal in whisking periods was performed with a semiautomatic approach by applying simultaneously both a temporal threshold and an amplitude one. While the temporal threshold was fixed at 200 ms, the amplitude threshold was extracted with a semiautomatic approach: in a portion of approximately 1/10 of the full length video, whisking periods were individuated manually and this binarization was used to find the best amplitude threshold with a Roc analysis. Temporal gaps between whisking periods that resulted to be shorter than 0.5 s were considered whisking as well and the mean angle was not calculated for frames in which less than 4 whiskers were detected, linear interpolation was used to fill these missing frames. Signals were at the end downsampled at 80 Hz.

Pupil size

A movie of the eye contralateral to the surgery was acquired during each experimental session with a CMOS camera (Basler acA800) at 80 Hz acquisition rate. Illumination was provided by 920 nm radiation used to perform calcium imaging with the two-photon microscope exiting from the pupil. A long pass filter (Thorlabs HP 900) was placed in front of the camera objective in order to discard the unwanted light. Movies acquired in this way showed a white pupil in a dark background. Movies were analyzed with Matlab: each frame was thresholded with Otsu's method and the region corresponding to the pupil was approximated with an ellipse. The major axis length of the fitting ellipse was considered the pupil diameter. Frames in which the pupil was not detected were interpolated linearly.

Locomotion

Locomotion signals were obtained with an optical encoder mounted under the wheel and analyzed with Matlab. Detection of locomotion periods was performed thresholding the speed of the wheel: thresholds were adapted from [251]: after downsampling the signal at 40 Hz, an instant was considered to be part of a locomotion period if the instantaneous speed was higher than 1 cm/s, the

instantaneous speed of the low passed signal (short pass filter at 0.25 Hz) was higher than 1 cm/s and if the average speed over 2 s windows was higher than 0.1 cm/s. Temporal gaps between locomotion periods that were shorter than 0.5 s were considered locomotion as well. Locomotion signals were at the end down sampled at 80 Hz.

After the processing, all behavioral variables (continuous and binary) were down sampled to the acquisition rate of two-photon calcium imaging data. Down sampling was performed using decimation and linear interpolation in case of continuous variables, only decimation in case of binary variables.

3.7 Immunohistochemistry

Deeply anesthetized animals were transcardially perfused with 0.01 M PBS (pH 7.4) followed by 4 % paraformaldehyde. Brains were post-fixed for 6 h, cryoprotected with 30 % sucrose solution in 0.1 M PBS and serially cut in coronal sections (thickness: 40 - 50 μm) using a HM 450 Sliding Microtome (Thermo Fisher). Sections were then counterstained with Hoechst (1:300, Sigma Aldrich, Milan, IT), mounted and coverslipped with a DABCO [1,4-diazobicyclo-(2,2,2)octane]-based antifade mounting medium. Fluorescence images were acquired with a Leica SP5 inverted confocal microscope (Leica Microsystems, Milan, IT).
For the evaluation of the anatomical connections between WPM and wS1, mice were perfused after 10 days from the injection and subsequent GRIN lens implantation. 50 μm thick coronal brain slices were cut, counterstained with Hoechst (1:300, Sigma Aldrich, Milan, IT) and mounted with VECTASHIELD Antifade Mounting Medium. Confocal images were acquired with a Nikon Eclipse Ti in the three channels (blue, red and green) and analyzed.

3.8 Analysis and statistics

<u>On-axis PSF measurements</u>

Values reported in Table 3 were expressed as mean ± standard deviation. A Kolmogorov-Smirnov normality test was run on each experimental sample. When comparing two populations of data, Student's t-test was used to calculate statistical significance in case of Gaussian distribution.

<u>ROIs density</u>

We observed that, in general, the background intensity was not uniform in the FOV and in some regions we could not detect ROIs. In order to discount this factor in the count of the ROIs, we normalized the count to the brighter part of the FOV, obtaining a measurement of the ROIs density (number of ROIs divided by the total bright area). To detect the dark background regions, we used

the edges of the FOV (where mostly dark noise is collected) as intensity threshold. All the parts of the FOV with mean intensity lower than 85th percentile of the "edges" intensity were discarded for the normalization of the ROIs count. The remaining part of the FOV was considered as bright area and used for the ROIs density analyses.

Behavioural states definition

Four behavioural states were defined: quiet (Q) if there was neither locomotion nor whisking, whisking (W) if there was whisking but not locomotion, locomotion (L) if there was only locomotion but not whisking, whisking and locomotion (WL) otherwise. Epochs with only locomotion were extremely rare (1.45 ± 0.75 % of total acquisition time, mean ± SE) and were not considered in all the following analyses. Therefore only three behavioural states were considered for the following analyses, denoted with Q, W and WL. For the SVM analysis and for the NMF analysis, where we performed a binary classification, we considered just two states: quiet (Q) and active (A). The Q state was defined as before, while the active state was the combination of both W and WL state.

Mean fluorescence across states

For each ROI, the raw fluorescence was averaged in each of the three behavioural states (Q, W and WL) to obtain the mean fluorescence for each state. The activity was then compared across states for the pooled data and at single acquisition level. Statistical comparison was performed with a Wilkoxon rank-sum paired test corrected for multiple comparison (Bonferroni post hoc correction).

Information theory analyses

In order to compute the information encoded in the calcium signal about whisking we considered two states (quiet Q and active A) and we calculated whether some information about the animal state was encoded within the activity of single ROIs. We used the Matlab toolbox provided in [252]. For each state, we randomly sampled (without replacement) n_T time points, where n_T was the number of time points spent in the less frequent state. For each ROI, we used the calcium activity in the selected time points to compute the information carried by that ROI regarding the state of the animal (direct method, quadratic extrapolation for bias correction, bins = 2, shuffling iterations = 500). We considered the amount of information significantly different from 0 only if the real information value was larger than the 95th percentile of the distribution of n = 500 shuffled information values. We repeated this procedure n = 100 times, randomly sampling different time points. The reported information values are the average information encoded across different iterations.

Support vector machine (SVM) classification

Support vector machines (SVM) are supervised models used for data classification. We trained a Gaussian kernel SVM to classify the animal state (Q or A) by observing either single ROI activity or population activity. We considered only two states (W and Q), as we did for the information analysis. For each state, we randomly sampled (without replacement) n_T time points, where n_T was the number of time points spent in the less frequent state, and we split them into two equal and balanced sets. We used one set as the training set for the SVM. We performed ten-fold cross validation on the training set over a fixed grid for the hyperparameters of the SVM. We then tested the performance of the SVM using the test set. We repeated this procedure n = 100 times randomly sampling different time frames. The reported classification accuracy is the average information encoded across different iterations. We classified the animal state using both single ROIs activity and population activity. For population activity, we first considered only the ROIs in the central part of the FOV (distance from FOV center < ¼ of FOV radius) and then incrementally added the other ROIs (distance steps = ¼ of FOV radius) for the training and testing phase of the SVM.

Non-negative matrix factorization

Non-negative matrix factorization (NMF) is a dimensionality reduction technique that consists in representing the data (n x t) as the product between a set on k non-negative modules (n x k) and k non-negative activation coefficients (k x t). The modules are weighted subsets of the data, while the activation coefficients of a module describe how the components of the module are activated in time.

To compute NMF, we considered only two states (Q and A), as we did for other analysis. For each state, we randomly sampled (without replacement) n_T time points, where n_T was the number of time points spent in the less frequent state, and we split them into two equal and balanced sets (a training set and a test set).

We selected the number of NMF modules looking at the ability of a LDA classifier trained on the reduced data to predict the presence or absence of whisking. We first reduced the dimensionality of the training set and the test set to k, with k ranging from 1 to the number of ROIs of the dataset. Then, for each factorization, we trained on the training set a LDA classifier to predict the behavioral state variable and we tested its performance on the test set. We selected as final dimension for the NMF, the number of modules at which we found the first elbow in the performance plot (performance increase <0.4%).

At the end, we reduced the dimensionality of the entire dataset computing the NMF with the selected number of modules. For each module in the obtained factorization, we computed the following quantities:

- Sparseness: $sparseness = \frac{\sqrt{\sum_j \left(w_j^{(i)}\right)^2}}{\sum_j w_j^{(i)}}$, where $w_j^{(i)}$ denotes the contribution of the j-th ROI to the i-th module. Sparseness values close to 1 indicate that few ROIs contribute heavily to the module, while sparseness values close to 0 indicate that the contribution of ROIs to the modules is more homogeneous.
- Whisking modulation index (WMI): $WMI = \frac{mean(act_A) - mean(act_Q)}{mean(act_A) + mean(act_Q)}$, where act_A and act_Q denote the activation coefficients in each behavioral state. WMI larger than 0 indicates that the module's activity is higher during A state, while WMI smaller than 0 indicates that the module's activity is reduced during A state.
- Spatial spread: this is the average weighted distance between each pair or ROIs in the module. The weights are given by the contribution of each ROI to the module.

Measurement of TC and CT connectivity

Six emispheres were used: three implanted with endoscopes, three injected but not implanted with the endoscope as controls. Three confocal images were acquired for each of them, at a minimum distance of 20 μm between different focal planes. They were blurred with a Gaussian filter (sigma = 2 μm) and binarized with a triangle thresholding method. wS1 was manually identified using anatomical cues form Hoechst labeling in each sample. To quantify the amount of preserved TC and CT connections, the percentage of suprathreshold wS1 area was calculated respectively for the green and the red channels. A single value for each sample was obtained by averaging between confocal images and used to run the Mann-Whitney tests for the different colors.

3.9 Simulations

Anatomical sample

We simulated the neurons from which we recorded signal as spheres. For each field of view (FOV) the average radius *r_mean* of the spheres was estimated from recorded data (*r_mean*= 7.9 ± 2.3 μm, mean±std). For each FOV, we then introduced some variability in the neurons size, sampling it from a normal distribution with mean *r_mean* and standard deviation *r_sigma* = 1.3 (within FOV std estimated from data). We added into the center of each neuron a nuclear region, such that the spherical shell surrounding the nucleus had a width of variable size (*r_shell* randomly sampled from a normal distribution with mean = 4 um and standard deviation=1). We assumed that such nuclear region did not express GCaMP6s, therefore the fluorescence signal could be collected only from the spherical shell surrounding the nucleus. We randomly placed the simulated neurons in a volume of size 500*500*80 um without any overlap between them until the volume was filled with neurons

or until a neural density of 83,100±7,900 cells/mm3 [253] was reached. The resolution of the spatial volume was 0.5 um/pixel in the x and y direction, 1 um/pixel in the z direction.

Neural activity

Neural spiking activity was generated as the sum of one or more Poisson processes. We assigned to each neuron a mean spiking rate (rho = 0.4 spikes/s, arbitrary selected) and we generated a binary synchronicity matrix (with value 1 for connected neurons, connection probability=0.8, arbitrary selected). The activity of each neuron was the sum of an independent Poisson process and as many common Poisson processes as the connected neurons. The spiking rate of the summed Poisson processes had the mean spiking rate characteristic for that neuron. We then generated calcium activity and fluorescence traces using the equations in [254]. To convolve spike trains into calcium activity we selected an autoregressive model of order 1 (parameter γ=0.7) and to convert calcium activity into fluorescence intensity we used a model with supralinearities and Hill saturation (parameters: baseline=0, single event amplitude=1500, Hill saturation coefficient=1, dissociation constant=1, noise variance=0.05). For further details about model parameters, please refer to [254].

Imaging conditions

We set the size and the resolution of the FOV we wanted to simulate (FOV size = 500*500 um, x and y resolution=2.5 um/pixel). We then adjusted the resolution according to the changes in magnification factor we estimated using experimental data (see § 3.3), obtaining a non-uniform resolution in the FOV. For each pixel in the FOV, we built the corresponding point spread function (PSF) and we placed it into the brain volume. The PSF was simulated as an ellipsoid. The ellipsoid x, y and z dimensions varied as a function of the distance from the FOV center and were determined using experimental measurements of fluorescent beads (see § 3.3). For each pixel in the FOV, the corresponding PSF was centered in the intersection between a line drawn from the pixel position in the xy plane and orthogonal to the xy plane and a spherical dome estimated from measurements of fluorescent films. The PSF was then rotated until its z axis is orthogonal to the estimated spherical dome. In case of uncorrected endoscopes we observed that the imaging surface was doubled in the outer part of the FOV. In this case, we assigned to each pixel two PSFs (one for each imaging surface). We also modeled changed in the fluorescence intensity of the FOV. We used measurements of subresolved fluorescent layers (see § 3.3) to estimate an intensity mask that is applied to the FOV.

Time Series simulation

To generate Time Series, we considered each pixel in the FOV and the corresponding PSF(s). There were 3 possible conditions:

- The pixel was in the edges of the FOV. The signal of the pixel was randomly sampled from a normal distribution, with mean and the standard deviation estimated from experimental data in the following way. We first found that dark noise mean was best fitted by a Gaussian mixture model (component 1: proportion=0.37, mean=137.48, std=48.96; component 2: proportion=0.63, mean=126.83, std=5.02), while the standard deviation of the dark noise depended on the dark noise mean in a linear way (p0=-175.39, p1=1.57). We therefore generated simulated dark noise with mean randomly sampled from the GMM distribution and standard deviation linearly dependent from the mean.
- The pixel was in the "central" part of the FOV, but no neurons were within its PSF(s). The signal of the pixel was randomly sampled from a normal distribution, with mean and the standard deviation estimated from experimental data in the following way. We first fitted the mean intensity of pixels neither in the edges nor belonging to ROIs using a lognormal distribution (mean=5.43, std=0.36) and computed the best linear fit between the squared root of the mean intensity and the intensity standard deviation (p0=-162.55, p1=18.28). We then generated simulated noise in the FOV as gaussian noise with mean randomly sampled from the lognormal distribution and standard deviation linearly dependent from the squared root of the mean.
- The pixel was in the "circle" and at least one neuron was in the PSF(s). We assigned to each voxel in the PSF Gaussian noise estimated as in the previous point, in case no neurons were in the voxel, or the fluorescence intensity of the neuron occupying that voxel. In case a neuron was contained in the voxel, we added Gaussian noise to the neuron signal. The mean of the added gaussian noise was zero, while the standard deviation was proportional to the square root of the mean intensity of the voxel (coefficients estimated from a linear fit between the square root of the mean intensity and the intensity standard deviation of pixels assigned to ROIs in experimental data. p0=-132.44, p1=16.94). We then averaged the activity of all the voxels.

<u>FOV segmentation</u>

We wanted to segment the FOV simulating a manual segmentation. We started from a full ground truth segmentation of the FOV. In this case, for each neuron, we knew whether its signal was collected from one or more pixels and we could generate the corresponding spatial footprint. i.e. the pixels collecting signal from that source. The final FOV ground truth segmentation was obtaining in three steps.

- The first step consisted in removing from the segmentation the neurons whose spatial footprint in the FOV was smaller than n_px (we tried n_px = 5,10,15). The underlying motivation was that users do not segment ROIs composed by only few pixels.

- The second step consisted in merging the spatial footprints of sources with a "large" overlap. We explored different threshold for the definition of "large" overlap (60, 70, 80, 90% of the footprint area). The underlying motivation was that users and demixing algorithms were able to split signals from different sources only if the overlap in the spatial footprint was not complete.
- The last step consisted in selecting only those spatial footprint with a signal of sufficient quality. We measured the quality of the signal using the peakSNR (defined in § 3.5). We explored different thresholds for the SNR (5, 10, 15, 20, 25, 30). The underlying motivation was that only ROIs with neural-like activity will be segmented in a manual segmentation.

Data analyses

Correlation with ground truth

In order to assess the reliability of the measured signal, we computed the correlation between the fluorescence signal of each segmented ROIs and the corresponding ground truth neuron. In case of merged neurons (step 2 in the segmentation algorithm), we computed the correlation with all the sources and considered the first and second highest correlations.

Pairwise correlations

We splitted the FOV in two regions: the central region (distance from center smaller than half the FOV radius) and an external ring (distance from center larger than half the FOV radius). For each pair of ROIs in each FOV region, we computed the pairwise distance between ROIs and the pairwise correlation between ROIs fluorescence signal. We also computed the pairwise correlation between the fluorescence ground truth signals of the neurons conveying signal to the ROI.

ROIs signal-to-noise ratio (SNR)

To measure the quality of the extracted ROIs signal, we used the signal-to-noise ratio, defined as $SNR = \frac{power(Cdf)}{power(Fraw-Cdf)} = \frac{\sum_i (Cdf(t_i))^2}{\sum_i (Fraw(t_i)-Cdf(t_i))^2}$. Before computing this quantity, we z-scored the raw fluorescence intensity (F_{raw}) and the deconvolved calcium activity (Cdf) of each ROI.

4 Results

Four types (type I-IV) of eFOV-microendoscopes of various lengths and lateral dimensions were developed, all composed of a GRIN rod, a glass coverslip and a microfabricated corrective aspheric lens (Fig. 23). One end of the GRIN rod was directly in contact with the glass coverslip and the GRIN rod was different in each of the four types of eFOV-microendoscopes (lateral diameter, 0.35-0.5 mm; length, 1.1-4.1 mm; all 0.5 NA; Table 3). The glass coverslip was 100 μm thick for type I, III, IV eFOV-microendoscopes and 200 μm thick for type II eFOV-microendoscopes. This design did not require additional cannulas or clamping devices [113], [118] which would increase the lateral size of the microendoscope assembly or reduce its usable length, respectively.

For each type of GRIN rod used in the eFOV-microendoscopes, ray trace simulations determined the specific lens profile (Fig. 23) that corrected optical aberrations and maximized the FOV (Fig. 24). In the representative case of type I eFOV-microendoscope, the coefficients used in equation (1) were: c: -2.579E-1, k:-1.74, α_1: 8.575E-1, α_2:-5.297E1, α_3: 5.952E3, α_4: -2.765E5, α_5: 7.258E6, α_6: -8.914E7, α_7: 2.469E8, α_8: 2.193E9. For type I eFOV-microendoscopes the corrective lens had a diameter of 0.5 mm and height of < 40 μm. For this type of eFOV-microendoscope, the simulated diffraction point spread functions (PSFs) at incremental radial distances (from 0 to 200 μm) from the optical axis showed that the Strehl ratio of the system was > 80% (diffraction-limited condition according to the Maréchal criterion [93]) at a distance up to ~ 165 μm from the optical axis with the corrective lens. For the same optical system without the corrective lens, this ratio maintained this value up to ~ 70 μm (Fig. 24A), leading to an increase in the area of the diffraction-limited FOV of ~ 5 times. The coefficients used in equation (1) for all other types of eFOV-microendoscope are reported in Table 2 (§ 3.1). Fig. 24B-D reports the simulated PSF and Strehl ratio for corrected and uncorrected type II-IV eFOV-microendoscopes. eFOV-microendoscopes, compared to uncorrected probes, showed a ~ 2-9 fold larger FOV in terms of area.

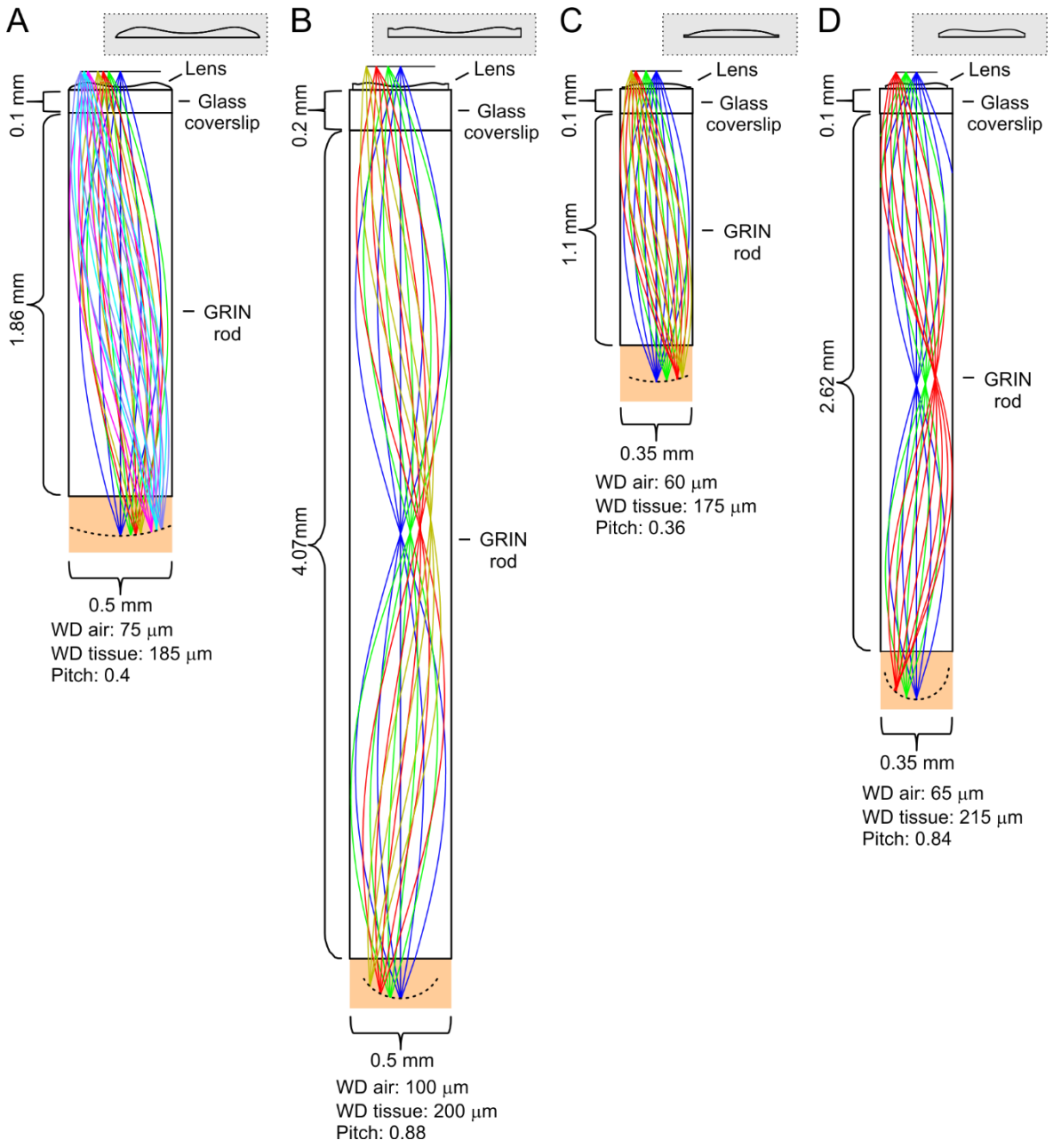

Fig. 23: Optical design of eFOV-microendoscopes

A-D) Images showing ray trace simulations for the four different eFOV-microendoscopes (type I-IV) developed in this thesis. The insets show the profiles of corrective polymer lenses used in the different eFOV-microendoscopes. For each eFOV-microendoscope, it is specified the thickness of the coverslip, the length, the diameter of the GRIN rod, the pitch of the GRIN rod, and the working distance, in air or in tissue, at which the correction of aberrations is performed. Portions of tissue in which imaging is performed lay below the distal end of the GRIN lenses, and are depicted as pink rectangles.

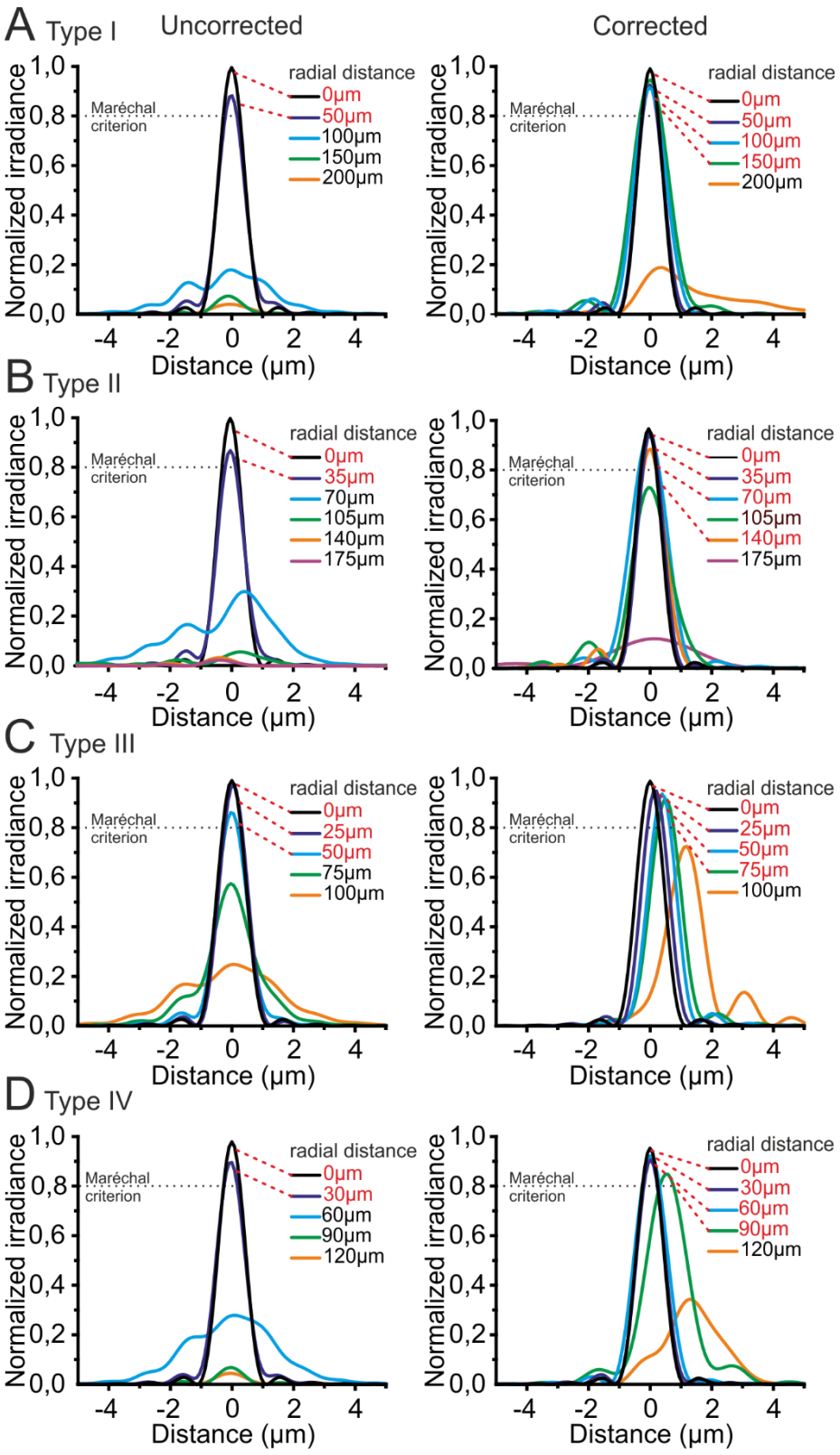

Fig. 24: Corrective lenses improve the simulated optical performances of ultrathin microendoscopes

A) Simulated diffraction PSFs of type I microendoscopes without the corrective lens (uncorrected, left) and with the corrective lens (corrected, right). PSFs are shown color coded according to their radial distance from the optical axis. The black dotted line represents the diffraction-limited condition that was set at 80 % (Maréchal criterion). Distances written in red indicate the radial positions at which

the maximal normalized irradiance of the corresponding PSF was > 80 %. B-D) Same as in A) for type II (B), type III (C), and type IV (D) microendoscopes.

Type	Diam. (mm)	Length (mm)	On-axis $FWHM_{x,y}$ (µm) N = 10	On-axis $FWHM_z$ (µm) N = 10	FOV diam. (µm) N = 5
I	0.5	1.86	uncor.: 0.89 ± 0.04 cor.: 0.82 ± 0.01 p = 1.2E-4	uncor.: 8.5 ± 0.4 cor.: 6.7 ± 0.2 p = 2.6E-10	uncor.: 148 cor.: 266
II	0.5	4.07	uncor.: 0.88 ± 0.04 cor.: 0.88 ± 0.03 p = 8.5E-1	uncor.: 9.7 ± 0.5 cor.: 7.3 ± 0.2 p = 1.5E-9	uncor.: 102 cor.: 312
III	0.35	1.1	uncor.: 0.81 ± 0.09 cor.: 0.76 ± 0.02 p = 9.5E-2	uncor.: 8.1 ± 0.3 cor.: 6.3 ± 0.3 p = 7.8E-11	uncor.: 124 cor.: 308
IV	0.35	2.62	uncor.: 0.82 ± 0.05 cor.: 0.77 ± 0.08 p = 9.7E-2	uncor.: 8.0 ± 0.4 cor.: 6.4 ± 0.5 p = 4.8E-7	uncor.: 68 cor.: 138

Table 3: Physical and optical characteristics of eFOV-microendoscopic probes

For statistical comparison of corrected vs uncorrected microendoscopes Student's t-test was used.

Corrective lenses were generated by TPP [149] and fabricated through plastic molding replication [246] directly onto the glass coverslip. Corrective lenses were printed at KAUST NanoFab CoreLabs with a Nanoscribe TPP system by the group of our collaborator Dr. Carlo Liberale combining a low *NA* objective and an IP-S resin. This configuration is recommended for micro-optics printing [255] because it provides smooth surfaces with optical-quality roughness and shape accuracy (Fig. 25A) and fast fabrication times. The matching between design and fabrication was verified for the four types of corrective lenses with a contact stylus surface profiler (Dektak 8, Veeco). The results (Fig. 25B) showed that the fabricated lenses faithfully replicate the designed 3D profile.

Replication of the lenses was performed with a plastic molding technique. In this way, corrective microlenses, made of UV-curable optically-clear adhesive (NOA63, Norland Products Inc., Cranbury, NJ), could be easily fabricated directly on coverslips. GRIN rods were precisely aligned to the corrective microlenses and glued on the opposite side of the coverslip using a custom optomechanical stage (Fig. 26A-B).

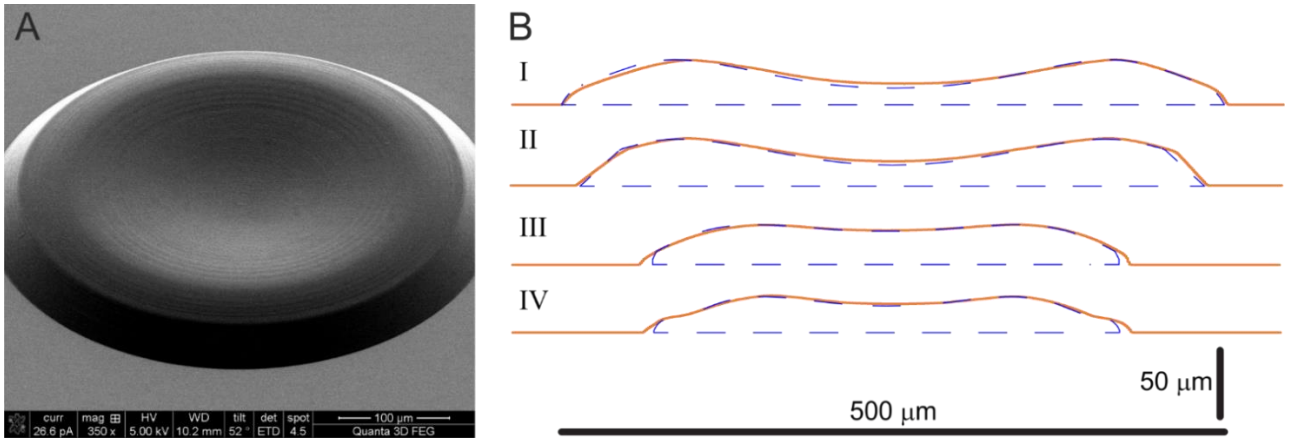

Fig. 25: Quality of TPP printed microlenses

A) SEM image showing an example of lens fabricated with TPP. B) Accuracy of lens profiles. Blue dashed lines indicate the designed lens profiles, while the red continuous lines represent the profiles measured with a contact stylus surface profiler.

To experimentally validate the optical performance of the eFOV-microendoscopes, we first coupled them with a standard two-photon laser scanning system using a customized mount, which allowed the coupling of the endoscopes with the microscope objective (Fig. 26C).

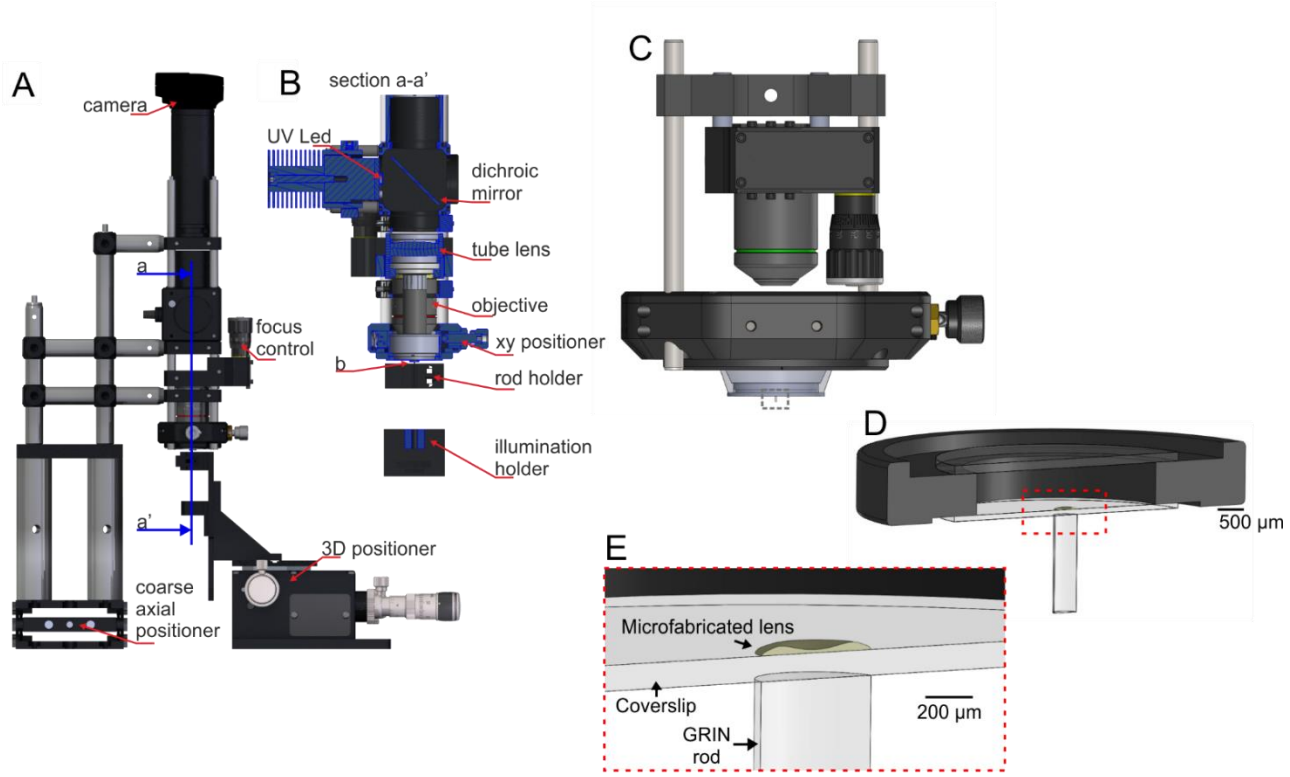

Fig. 26: Set ups for the assembly and characterization of eFOV-microendoscopes

A) Optomechanical stage used for microendoscope assembly. Arrows indicate key components: camera (DCC1645C), fine z control (SM1Z), coarse z control (L200/M), and xyz control (MAX313D/M). All items were purchased from Thorlabs. The blue line indicates the part of the set up whose section is shown at an expanded scale in B). B) Section of a portion (a-a') of the set up shown in A). Key components were: high power UV LED (M375L3, Thorlabs), long pass dichroic mirror (FF409-Di02, Semrock), tube lens (AC254-150-A, Thorlabs), objective (UPlanFLN 4x 0.13NA, Olympus), xy control (CXY1, Thorlabs), custom GRIN rod holder, fiber optic holder (HCS004, Thorlabs). C) Schematic of the optomechanical assembly used for microendoscopic imaging. The coupling objectives were EC Epiplan-Neofluar 20x (Zeiss) and LUCPLFLN 60X (Olympus). The z control (SM1Z) and xy control (CXY2) were purchased from Thorlabs. D) Schematic of the self-supported eFOV-microendoscope mount for head implant (highlighted with the grey dotted line in C) is shown at an expanded scale. The GRIN rod is attached to one side of the glass coverslip, the microfabricated polymer lens to the other side of the coverslip, coaxial with the GRIN rod. The coverslip is glued on a circular metal ring that facilitates fixation on the animal's skull. The detail of the coupling between optical elements is shown at an expanded scale in E). E) Zoom in of the portion highlighted with the red dotted line in D).

We measured the maximum on-axis spatial resolution by imaging subresolved fluorescence beads (diameter: 100 nm) at 920 nm with a 60X *NA* 0.7 microscope objective (LUCPLFLN 60X, Olympus). The large *NA* of the coupling objective (0.7) was used to overfill the acceptance angle of the back aperture of the microendoscope (*NA* = 0.5). We found that eFOV-microendoscopes had significantly

improved axial resolution compared to uncorrected probes. For example, for type I eFOV-microendoscopes, the minimal value of FWHMz was 6.7 ± 0.2 µm for corrected endoscopes and 8.5 ± 0.4 µm for uncorrected probes (Fig. 27A,B, Table 3; Student's t-test, p = 2.6E-10; N = 10). The lateral resolution was also slightly increased for type I eFOV-microendoscopes (Table 3). Experimental measures of lateral and axial resolution on-axis for type II-IV eFOV-microendoscopes are reported in Table 3. Importantly, the axial resolution was significantly increased in all corrected eFOV-microendoscopes compared to uncorrected probes. We then evaluated potential inhomogeneity of magnification across the FOV (distortion) in corrected microendoscopes by imaging a custom fluorescent reticular grid (Fig. 27C-D), which allowed us to evaluate the variation of the pixel size as a function of the radial position (Fig. 27E-F).

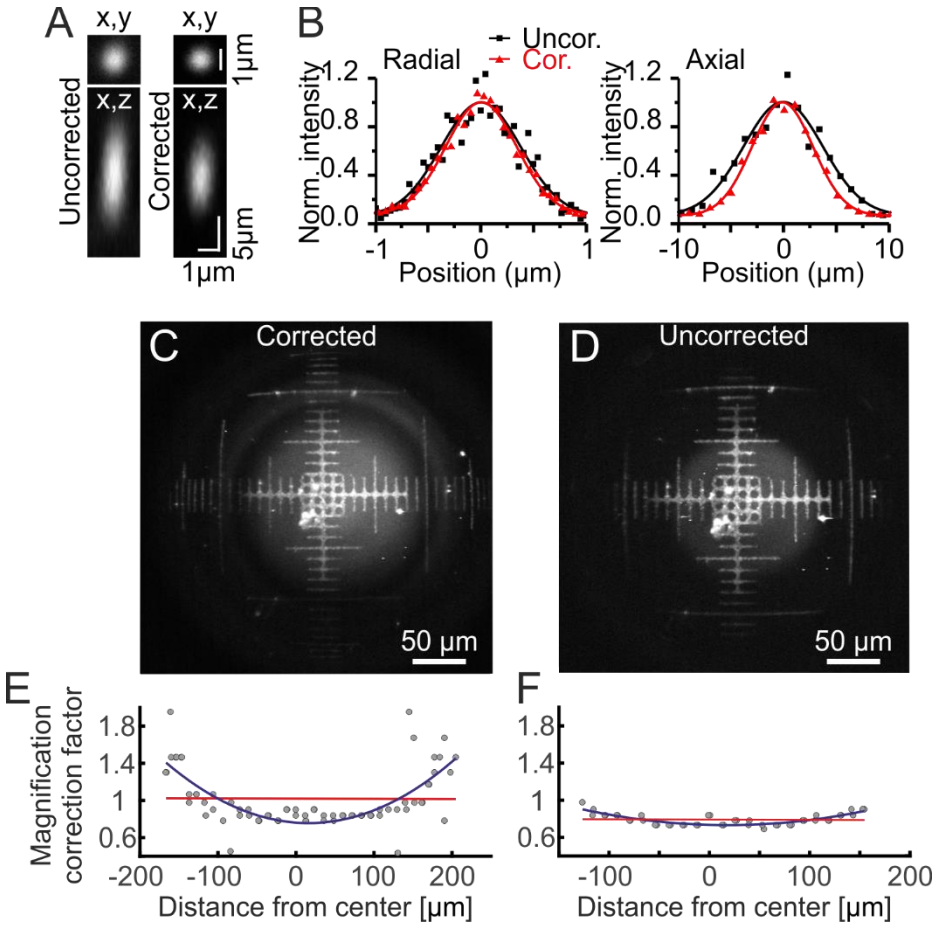

Fig. 27 On-axis resolution and distortion

A) Representative images in the x,y plane (top) and in the x,z plane (bottom) of a subresolved fluorescent bead (diameter: 0.1 µm) imaged with a type I eFOV-microendoscope without (uncorrected, left) and with (corrected, right) the microfabricated corrective lens. λ_{exc} = 920 nm. B) Normalized intensity profiles along the lateral (radial, left) and axial (right) directions of the images shown in A) for uncorrected (black) and corrected (red) type I microendoscopes. Data are normalized to the maximum of the Gaussian fit (solid line). C-D) Images of the fluorescent reticular grid used to

determine the FOV distortion for type II microendoscope. E-F) Magnification correction factor as a function of the radial position in corrected (left) and non corrected (right) microendoscopes. The magnification corrector factor is the conversion factor between undistorted (taken without the endoscope) and distorted (taken with the endoscope) pixel size. A magnification correction factor higher than 1 means a reduced magnification, hence a bigger pixel size. Each point represent experimental values pooled from the two perpendicular directions in the x, y plane.

Next, we measured the spatial resolution as a function of the radial position by imaging subresolved fluorescence beads (diameter: 100 nm) at 920 nm with a 20X *NA* 0.5 microscope objective (Epiplan-Neofluar, Zeiss). This measurement was used to evaluate the increase in dimensions of the FOV upon aberration correction using polymer lenses. Fig. 28 shows the axial and lateral resolution at different radial distances from the optical axis, for the four types of corrected endoscopes. While the lateral size of the PSF is not significantly improved by the aberration correction, in all four type of microendoscopes, the axial resolution is significantly higher over longer radial distances when the corrective lens is applied compared to the uncorrected case. It is important to note that in these measurements, we did not consider the curvature of the FOV, which, as expected by ray trace simulations (Fig. 23), is more pronounced for eFOV-microendoscopes. We then estimated the radial size of the FOV based on the values of axial resolution measured in Fig. 28. The radius of the FOV was defined as the distance at which data fitting curves intersected a threshold set at the value of 10 μm (roughly the average diameter of a neuron in many brain regions). We found that the eFOV-microendoscopes had a FOV area that was ~ 3.2 to 9.3-folds wider (depending on microendoscope type) compared to uncorrected probes (Fig. 28,
Table 3), demonstrating extended FOV in corrected microendoscopes, in good agreement with the predictions of the optical simulations. Since aberrations generally increase with the length of the GRIN rod used in the microendoscope [133], aberration correction resulted in larger improvements in optical performance in the eFOV-microendoscope with the longer rather than shorter GRIN rod.

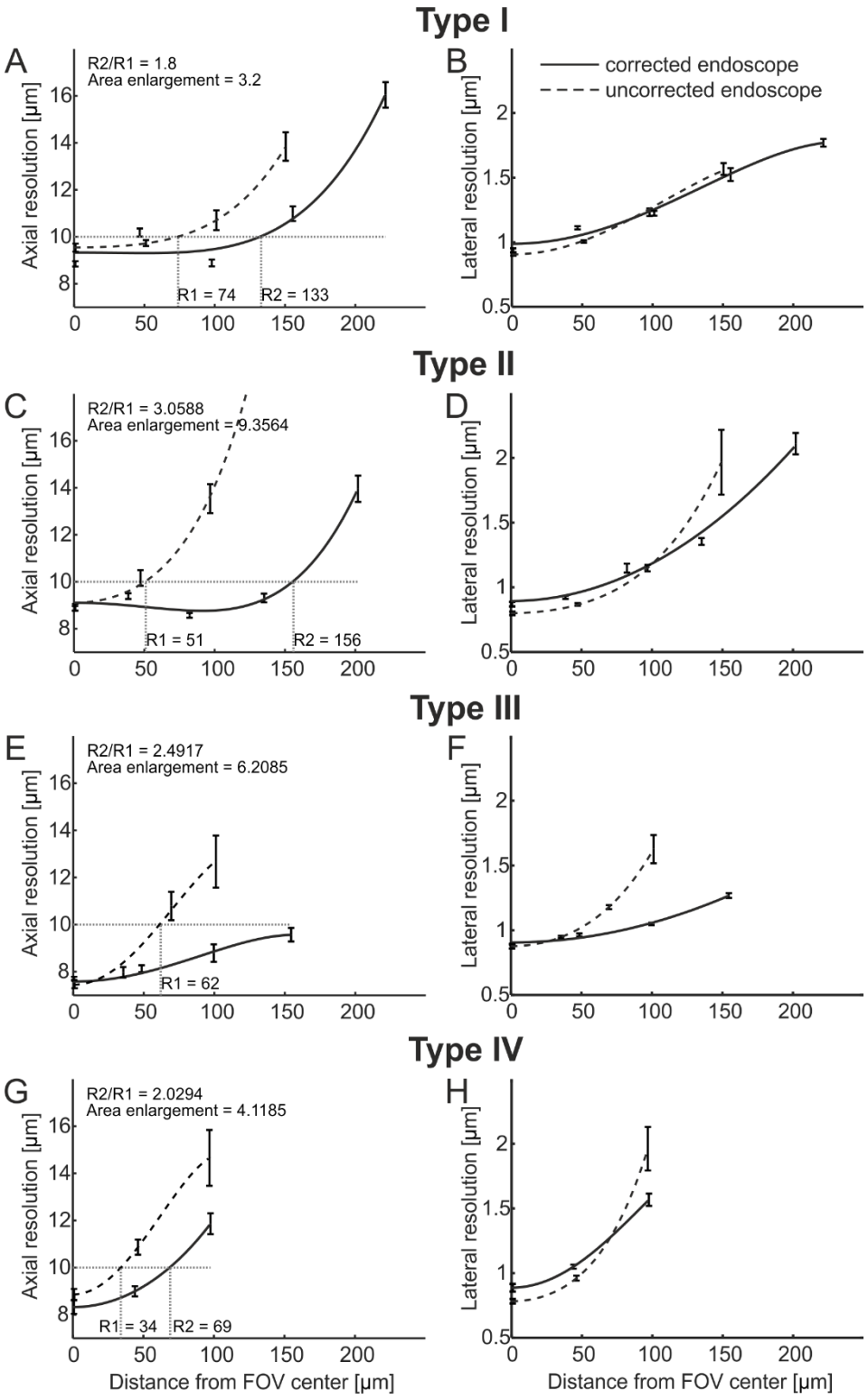

Fig. 28: Spatial resolution across the FOV in corrected endoscopes

Axial resolution (left column, A, C, E, G) and lateral resolution (right column, B, D, F, H) across the FOV for the four types of endoscopes in the corrected (solid line) and uncorrected (dashed line) cases, as a function of radial position. Points represent values obtained by averaging at least eight measurements from three different probes, while error bars represent standard deviations. Lines are quartic functions fitting the data. The radial extension of the FOV was estimated at the intersection between the fitting function with a 10 µm threshold (dotted grey line) and is reported as R1 (for the uncorrected probes)

and R2 (for the corrected probes). The increase of the radial FOV is evaluated by the ratio R2/R1. The obtained value is squared to quantify the corresponding enlargement in terms of area (upper-left inserts in left column graphs).

The ability of eFOV-microendoscopes to effectively image larger FOVs compared to uncorrected probes was further confirmed with subresolved thin fluorescent layers (thickness: 300 nm) as detailed in [256] (Fig. 29-Fig. 30) and in biological tissue by imaging neurons expressing GFP in fixed brain slices (Fig. 31).

Fig. 29 shows the imaging surface in all types of corrected microendoscopes via x,z projections of 3D acquisitions of a subresolved fluorescent layer (thickness: 300 nm). Both the axial profile (thickness) and the intensity of the imaged fluorescent layer (which represent the imaging surface) appear homogeneous over longer radial distances in the case of eFOV microendoscopes compared to uncorrected probes. For uncorrected probes, the thickness of the imaged subresolved fluorescence layer becomes larger and its intensity rapidly fades with radial distance. It is interesting to note that in the off-axis regions of uncorrected probes, astigmatism is clearly visible in the form of two separate lobes. Importantly, eFOV-microendoscopes do not show this behavior, demonstrating that the corrective lens effectively compensates for astigmatism. Fig. 29 shows the curvature of the focal plane of both corrected and uncorrected endoscopes. Corrective lenses thus do not correct for field curvature. This type of aberration was more pronounced in the case of eFOV-microendoscopes, probably because of their larger FOV. The enlargement of the FOV in corrected probes is also shown in Fig. 30, where x,y projections (Fig. 30A) of the thin film aquisitions were analyzed to reveal the expansion of average radial distribution of fluorescence intensity (Fig. 30A') when the corrective lens is applied. The diameter of the FOV (measured at radial distances at which the measured fluorescence drops below 80%) was significantly higher for corrected compared to uncorrected microendoscopes (356.5 ± 8.4 μm vs 218.8 ± 83.4 μm for corrected and uncorrected type I probes, respectively, p = 9E-4, N = 7; 360.3 ± 11.3 μm vs 156.9 ± 4.8 μm for corrected and uncorrected type II probes, p = 2E-14, N = 8-9; 163.8 ± 4.5 μm vs 131.1 ± 6.0 μm, for corrected and uncorrected type III probes, p = 4E-8, N = 9; 234.3 ± 2.1 μm vs 117.3 ± 3.1 μm, for corrected and uncorrected type IV probes, p = 7E-18, N = 8-9. All p-values were obtained with Student's t-test).

Fig. 31 shows the enlarged FOV of eFOV-microendoscopes on fixed brain tissue, with GFP-expressing neurons: cell bodies and their processes are clearly visible at distal portions of the images in the case of corrected probes.

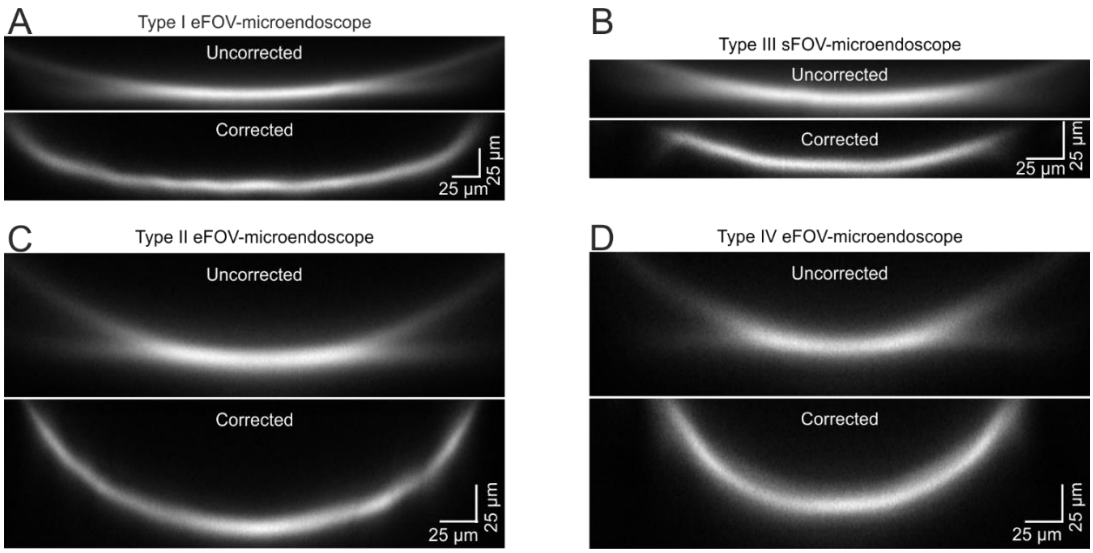

Fig. 29: Extended FOV in corrected microendoscopes: subresolved fluorescent layers. XZ projections.

A-D) x,z projections (x, horizontal direction; z, vertical direction) of a z-stack of two-photon laser scanning images of a subresolved fluorescent layer (thickness: 300 nm) without (uncorrected, top) and with (corrected, bottom) corrective lens for type I (A), type II (C), type III (B) and type IV (D) eFOV-microendoscopes. Excitation wavelength: λ = 920 nm.

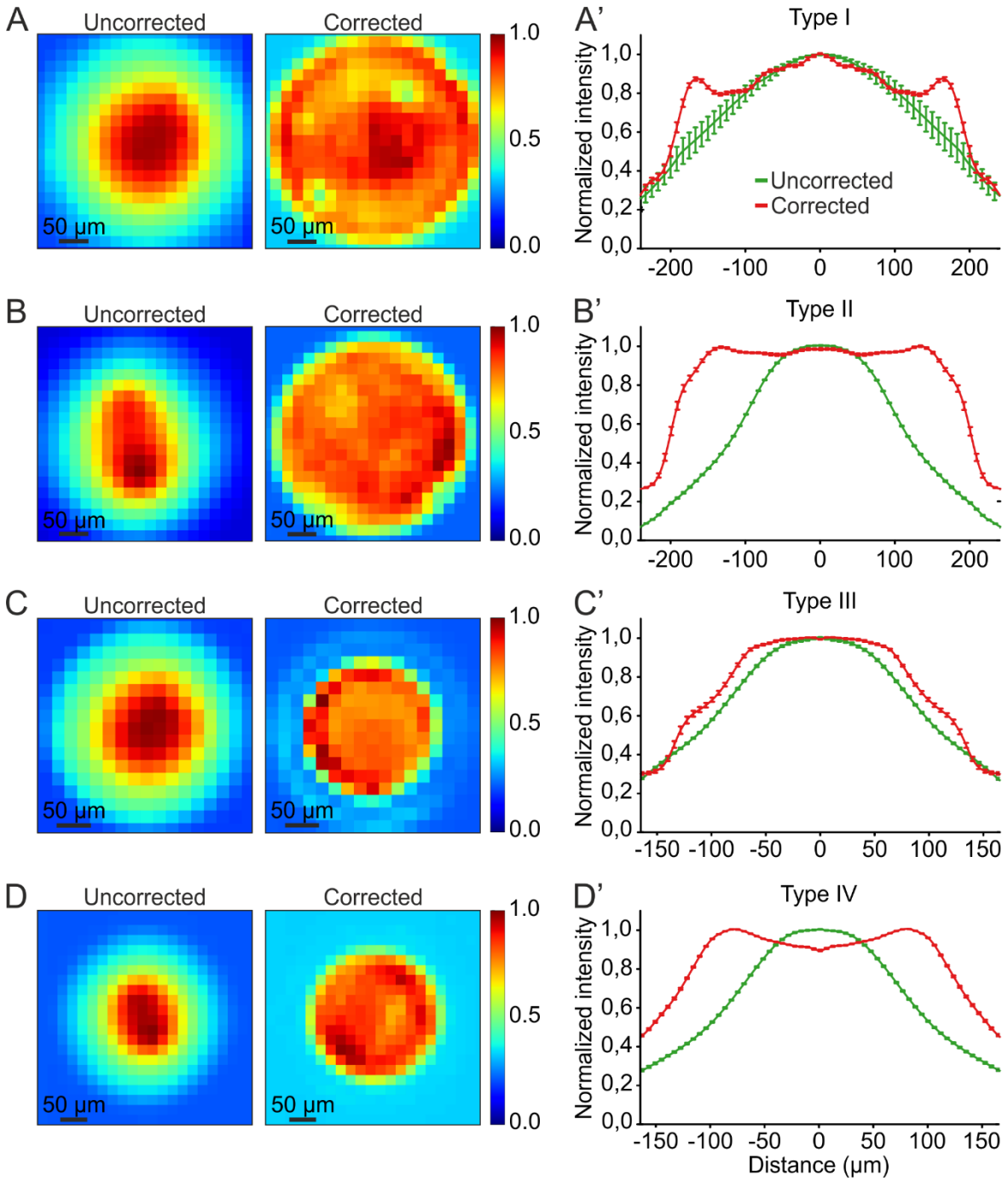

Fig. 30: Extended FOV in corrected microendoscopes: subresolved fluorescent layers. XY projections

A) Pseudocolor images showing the spatial distribution of fluorescence of uncorrected (left image) and corrected (right image) type I microendoscopes. Images are obtained monitoring a thin homogeneous fluorescence layer and were resampled (pixel dimension: 20 µm) to suppress sharp fluorescence variations. A') Fluorescence intensity profile along a line crossing the optical axis for uncorrected (green line) and corrected (red line) type I microendoscopes. Traces are shown as mean ± sem across different experiments (N = 7). B-B') Same as in A-A') for type II microendoscopes. In B'), N = 8. C-C') Same as in A-A') for type III microendoscopes. In C'), N = 9. D-D') Same as in A-A') for type IV microendoscopes. In D'), N = 8.

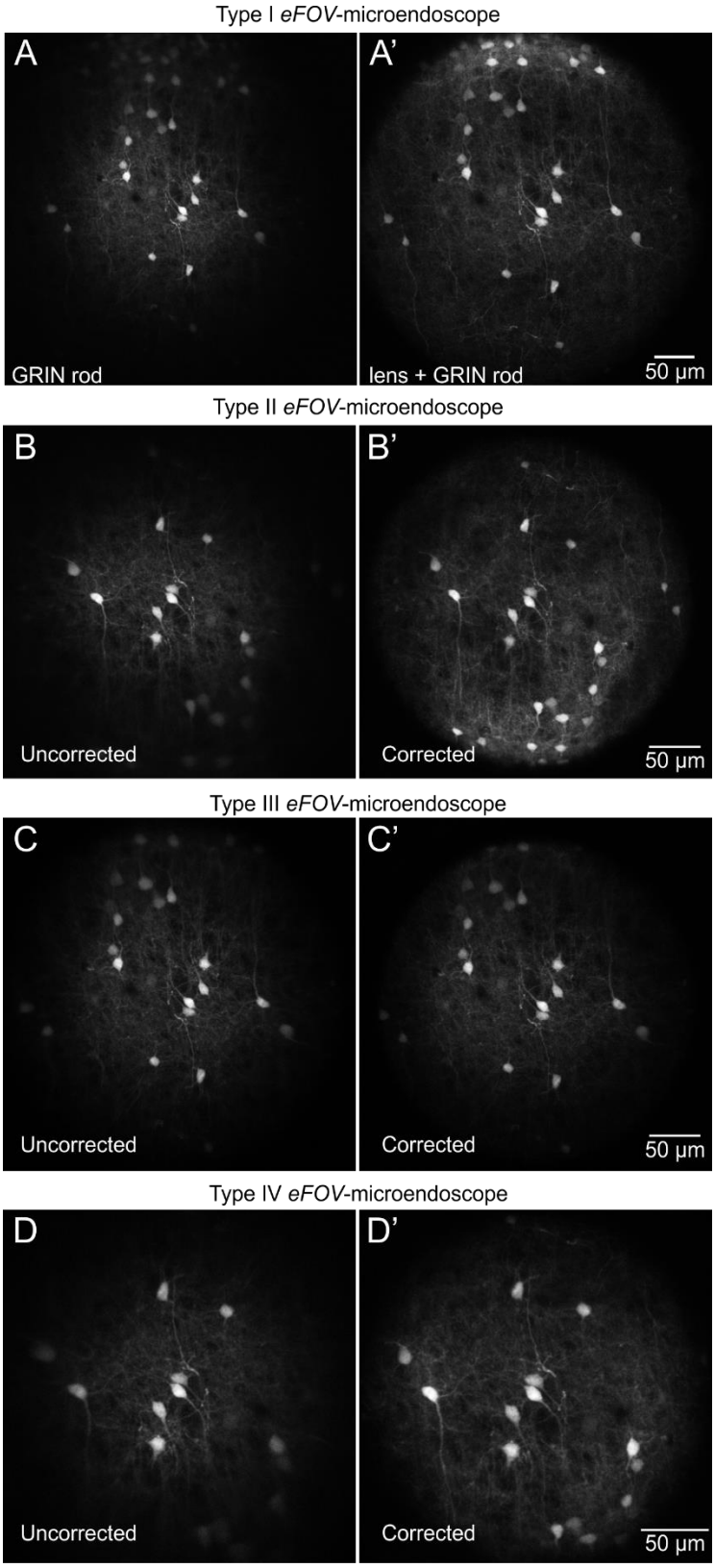

Fig. 31: Extended FOV in corrected microendoscopes: fixed brain tissue

A-D) Representative images of fixed cortical tissue expressing GFP in neuronal cells were acquired with type I (A), type II (B), type III (C) and type IV (D) eFOV-microendoscopes without (uncorrected, left panels) and with (corrected, right panels) corrective lens. Excitation wavelength: λ = 920 nm.

To validate eFOV-microendoscope performance for functional measurements in vivo, we expressed the genetically-encoded calcium indicator GCaMP6s in different mouse deep brain regions: hippocampus, striatum and thalamus (Fig. 32) and implanted eFOV-microendoscopes above the injected areas (Fig. 33). It is worth noting that an advantage of the customized mount that we developed to hold eFOV-microendoscopes (Fig. 26D,E) is that it allows their full-length insertion within the tissue. As compared to the most common microendoscope configurations described in the literature ([123], [124], [134], [135], [257]), our experimental solution enables the use of shorter probes, which are less sensitive to aberrations.

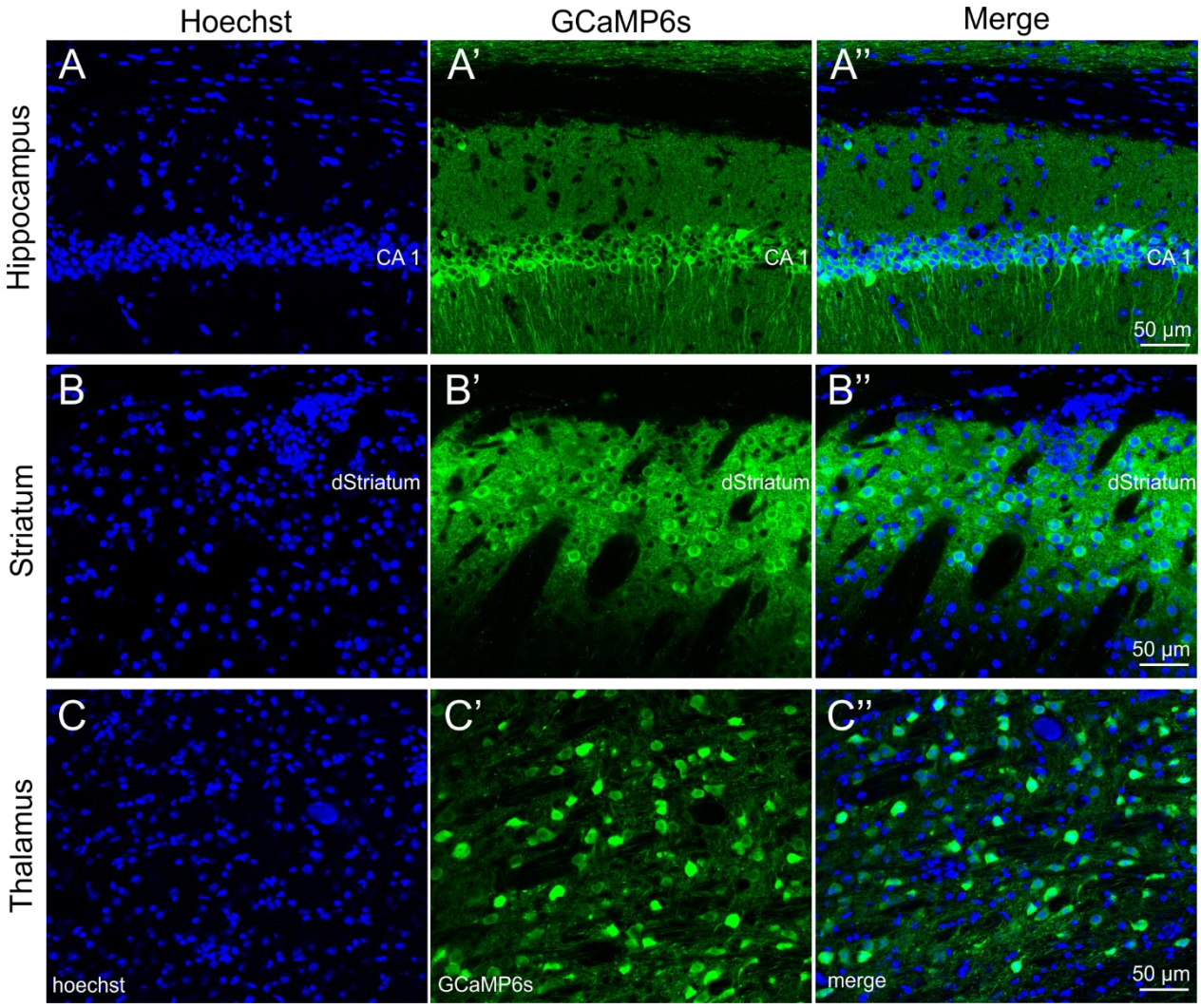

Fig. 32: GCaMP6s expression in deep brain regions

A-A'') Confocal images of hippocampal CA1 neurons expressing GCaMP6s (A'). Nuclei were counterstained with Hoechst (A). Images are merged in A''. Scale bar in A'' applies to A-A''. B-B'') Same as in A-A'' for neurons in the dorsal striatum. C-C'') Same as in A-A'' for neurons in the ventral posteromedial (VPM) thalamic nucleus.

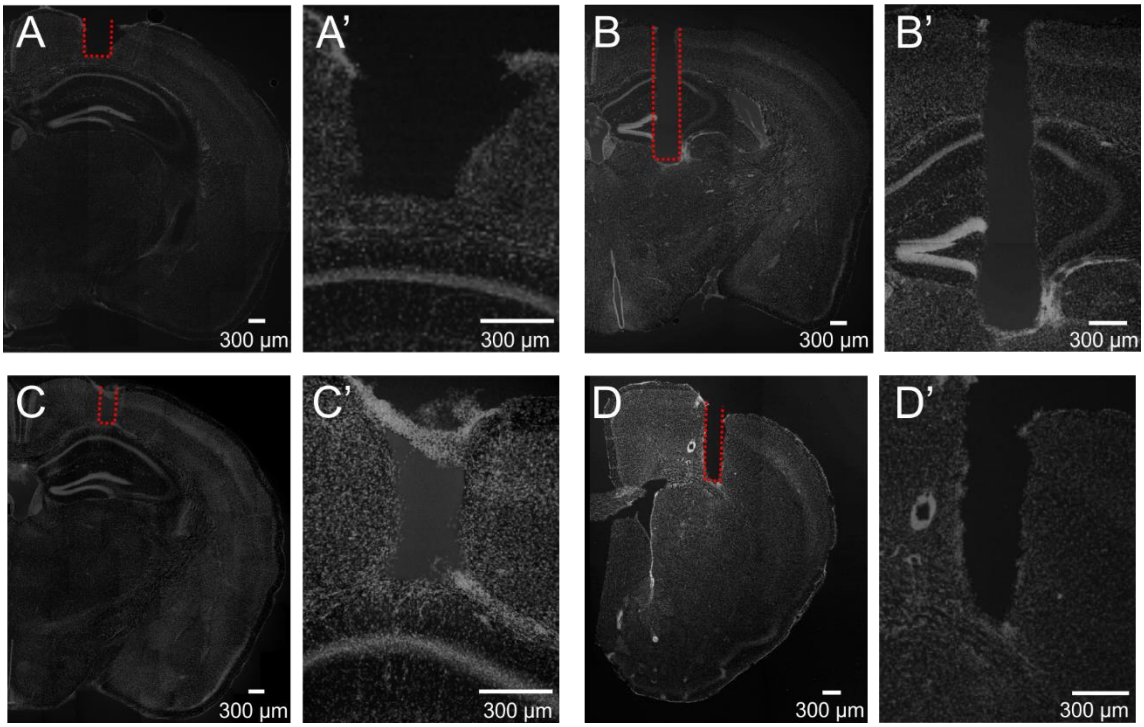

Fig. 33: Implantation of different types of eFOV-microendoscopes for imaging diverse brain regions

A-D') Confocal images showing coronal slices from mice implanted with type I (A-A'), type II (B-B'), type III (C-C') and type IV (D-D') eFOV-microendoscopes. Type I and III eFOV-microendoscopes were used to reach the hippocampus, type II to reach the thalamus and type IV to reach the striatum. Slices were counterstained with Hoechst. The probe track is highlighted with the red dotted line in A, B, C, D and shown at a higher magnification in A', B', C', D'.

We applied eFOV-microendoscopes to perform in vivo population imaging in injected anesthetized mice in the raster scanning configuration at 0.5-0.7 Hz (Fig. 34). Spontaneous activity in the CA1 hippocampal region was imaged with type III eFOV-microendoscopes (Fig. 34A) and type I eFOV-microendoscopes (Fig. 34B). Using a cell-sorting algorithm based on PCA/ICA analysis [248], tens to hundreds of active ROIs were identified and could be imaged on a single FOV using eFOV-microendoscopes, confirming efficient population imaging. Moreover, neuronal processes and dendritic spines could be reliably monitored in lateral parts of the FOV, demonstrating high-resolution imaging across the whole extended FOV in vivo and proving the effectiveness of eFOV-microendoscopes for imaging neuronal activity at both the cellular and synaptic levels. Longer eFOV-microendoscopes for imaging of deeper brain areas, such as the dorsal striatum and the ventral posteromedial thalamic nucleus, were also successfully implanted.

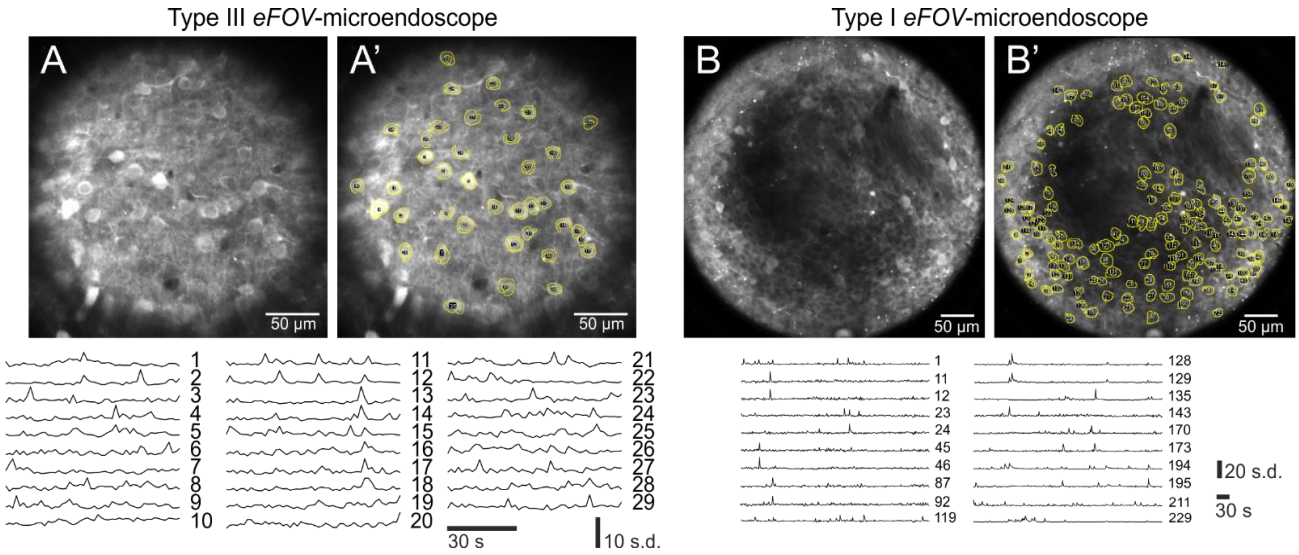

Fig. 34: Large FOV functional imaging of hippocampal networks with minimal invasiveness in anesthetized mice

A) Population imaging with ultrathin type III eFOV-microendoscopes. Average projection of fluorescence dynamics in GCaMP6s expressing hippocampal neurons recorded by two-photon imaging using type III eFOV-microendoscopes. Active ROIs are identified and numbered in A'). The lower panel shows fluorescence signals over time for the ROIs displayed in A'). B) Population imaging with ultrathin type I eFOV-microendoscopes. Average projection of fluorescence dynamics in GCaMP6s expressing hippocampal neurons recorded by two-photon imaging using type I eFOV-microendoscopes. Active ROIs are identified and numbered in B'). The fluorescence signal over time for some representative ROIs are displayed in the panel below.

We then extended the use of eFOV-microendoscopes to perform two-photon functional imaging in awake, head-fixed mice. Using type II eFOV-microendoscopes, we examined the spatio-temporal activation of neuronal populations in the ventral posteromedial (VPM) thalamic nucleus, a primary relay area involved in the processing of somatosensory information. Our goal was to measure the output activity of VPM neurons and to study how this activity is modulated in space and time by the behavioral state of the animal (e.g., whisking, locomotion, and arousal). For this aim, it is important to note that VPM output activity is strongly modulated by the excitatory input to the VPM that originates from cortical LVI of the whisker primary somatosensory cortex (wS1). Moreover, wS1 activity, including that of LVI, is in turn strongly regulated by VPM spiking, which represent one of the main excitatory inputs to wS1. Thus, in order to record VPM signals resembling those occurring in unperturbed physiological conditions, it is of fundamental importance to preserve most of the input/output VPM connections, in particular the thalamocortical and corticothalamic connectivity. Many thalamic imaging experiments have been performed with a large optical window [258] that requires removing a large portion of the overlaying cortical tissue, including significant portion of

wS1 (Fig. 35). In this context, the use of ultrathin, corrected microendscopes allows imaging of a large number of neurons with minimal invasiveness, sparing many of the fundamental afferent/efferent fibers targeting/originating from the VPM. To experimentally confirm that most of the anatomical connections between VPM and wS1 were preserved in mice implanted with eFOV microendoscopes, we injected eGFP and red-retrobeads in VPM (Fig. 36A) in implanted and non-implanted animals. In such a preparation, green and red fluorescence signals in wS1 represent the presence of direct thalamo-cortical (TC) and cortico-thalamic (CT) anatomical connections, respectively, with specific topographical organization. TC axons were observed in LIV of wS1, while CT axons originated from LVI. Importantly, both TC and CT connectivity was not significantly affected by the implantation of type II eFOV-microendoscopes (Fig. 36B).

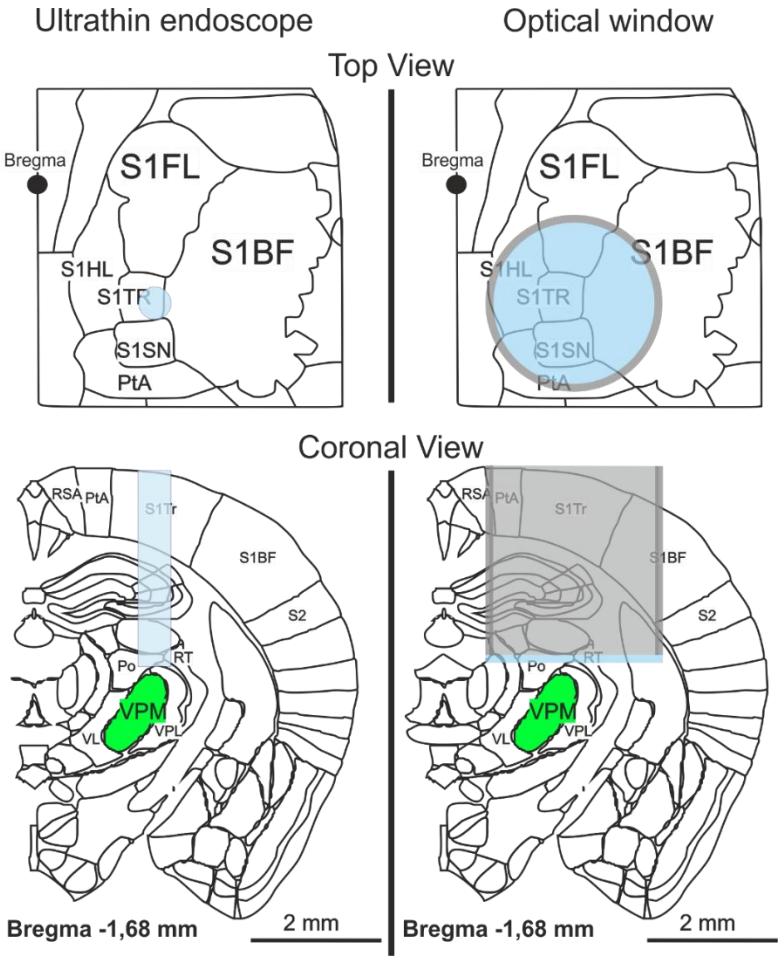

Fig. 35: Invasiveness of ultrathin endoscope vs optical window in VPM imaging

Schematic showing the implantation of an ultrathin microendoscope (left) and of an optical window (right) for thalamic two-photon imaging. Upper panel shows a view from the top, while the coronal view is reported in the bottom panel. S1FL = primary somatosensory, forelimb region; S1BF = primary somatosensory, barrel field; S1HL = primary somatosensory, hindlimb region; S1TR = primary somatosensory, trunk region; S1SN = primary somatosensory, shoulder and neck region; PtA = parietal association region; RSA = retrosplenial agranular region; S2 = second somatosensory cortex; VPM =

ventral posteromedial thalamic nucleus; RT = reticular thalamic nucleus; Po = posteromedian thalamic nucleus; VPL = ventral posterolateral thalamic nucleus; VL = ventrolateral thalamic nucleus.

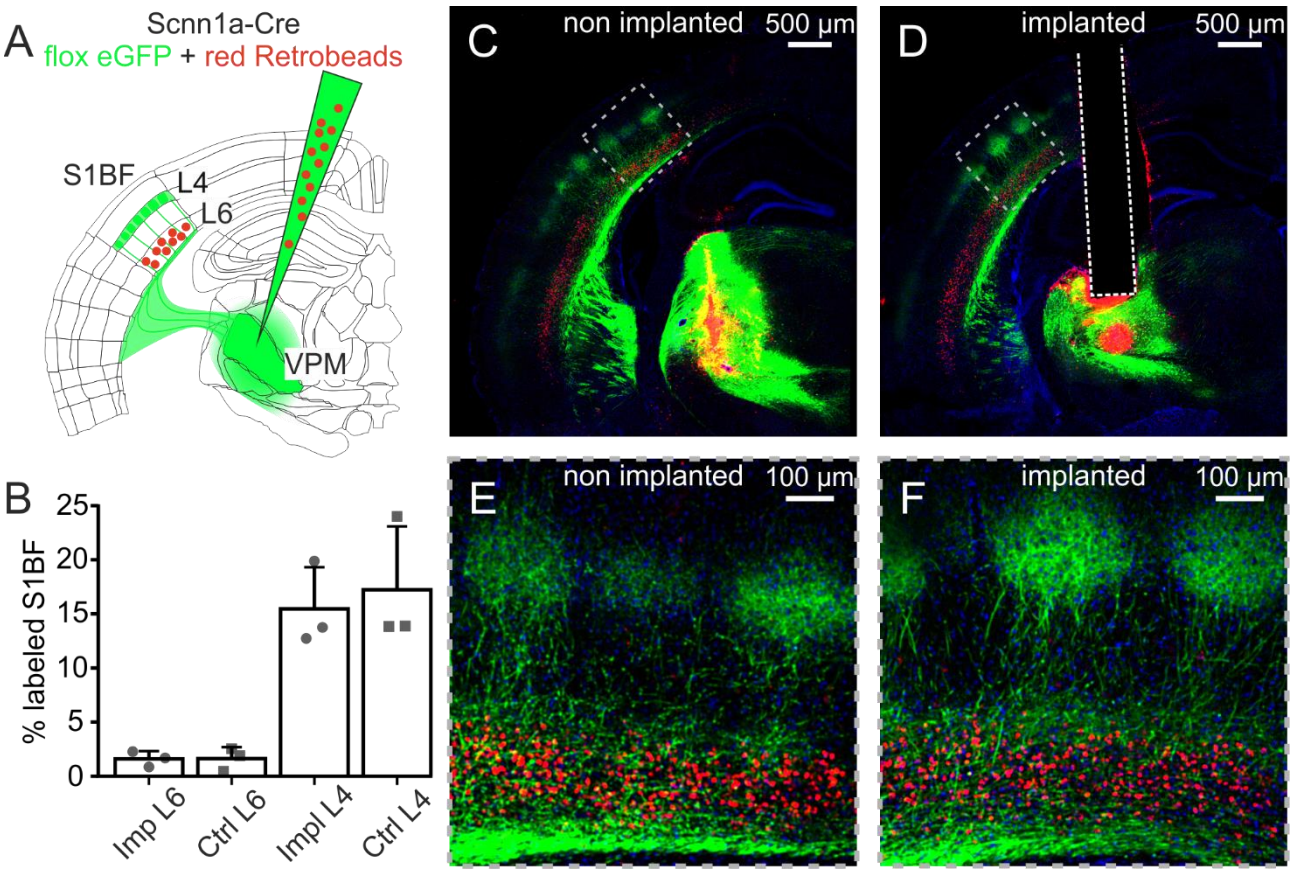

Fig. 36: Ultrathin endoscope implants preserve the anatomical connectivity of the VPM-wS1 loop

A) Injection of red retrobeads and of an AAV virus transducing floxed eGFP in the thalamic VPM nucleus of Scnn1a-Cre mice, a strain of transgenic mice expressing the enzyme Cre recombinase in VPM neurons. B) Percentage of the labeled barrel field cortical area (wS1) by retrobeads (red signal, LVI) and eGFP (green signal, LIV). C) Confocal image showing a coronal slice from a control animal. Scale bar 500 µm. D) Same as C) but for a mouse implanted with a GRIN microendoscope. E) Zoom in of C) over wS1. Scale bar 100 µm. F) Same as in E) but for a zoom in of D).

We then locally injected floxed-GCaMP6s AAV in the VPM of mice of the transgenic line SCnn1a-Cre, which expresses the Cre recombinase enzyme prevalently in primary thalamic nuclei, and implanted type II eFOV microendoscopes (Fig. 37A) such that the front end of the endoscope faced the VPM. Fig. 37B shows GCaMP6s staining of VPM neurons in fixed tissue and Fig. 37C shows VPM neurons imaged in vivo through the eFOV microendoscope. Mice expressing GCaMP6s and implanted with the eFOV microendoscope were head-fixed on a running wheel under the two-photon microscope, after a period of habituation to the experimental conditions (see Materials and Methods for details). Locomotion was monitored, as well as pupil diameter and movements of the

whiskers (Fig. 38A-B). Signals measuring locomotion and whisker movements were binarized according to a threshold criterion in order to identify time windows in which mice were running or actively whisking (Fig. 38C) and neuronal activity was extracted from t-series of fluorescence images (Fig. 38D-E). Neuronal segmentation was performed manually, using a graphical user interface developed in collaboration with Dr. Stefano Panzeri's laboratory (see § 3.5). We identified quiet (Q) periods, time intervals that were characterized by the absence of locomotion and whisker movements, and active periods, intervals with locomotor activity, dilated pupils, and whisker movements. Active periods were subdivided into whisking (W), whisking and locomotion (WL), and locomotion with no whisking (L). Mice move their whiskers when they move, and therefore L periods were very rare. Fig. 38F shows a histogram representing the amount of time spent in the different behavioral states.

We found that resting periods showed calcium events that were distributed both across time and neurons. In contrast, active periods displayed an increase in both frequency and amplitude of calcium signals across VPM neurons compared to resting periods. This results in a significant increase in the average fluorescence across neurons during active periods (Fig. 38G). The increase in neuronal activity is also correlated with pupil size, which indeed reflects the arousal level of the animal [259]. Moreover, active periods were characterized by the emergence of a significant number of neural pairs displaying correlated activity over hundreds of micrometers, suggesting the presence of distributed functional subnetworks, which are further examined below.

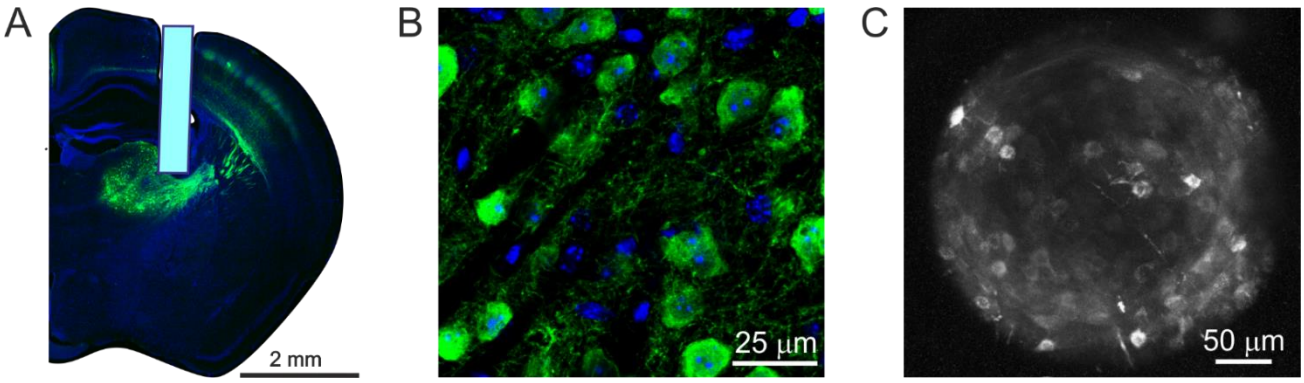

Fig. 37: GCaMP6s expression in the ventral posteromedial nucleus (VPM) of the mouse thalamus

A) Epifluorescence image of fixed tissue showing GCaMP6s expression (green signal) in thalamic nuclei including the VPM following viral injection in Scnn1a-Cre transgenic mice with an AAV virus carrying a floxed GCaMP6s construct. Hoechst staining is shown in blue. B) Confocal image displaying GCaMP6s-expressing neurons in the VPM in fixed tissue. C) Two-photon image showing GCaMP6s expression in the VPM in vivo acquired through type II eFOV-microendoscope.

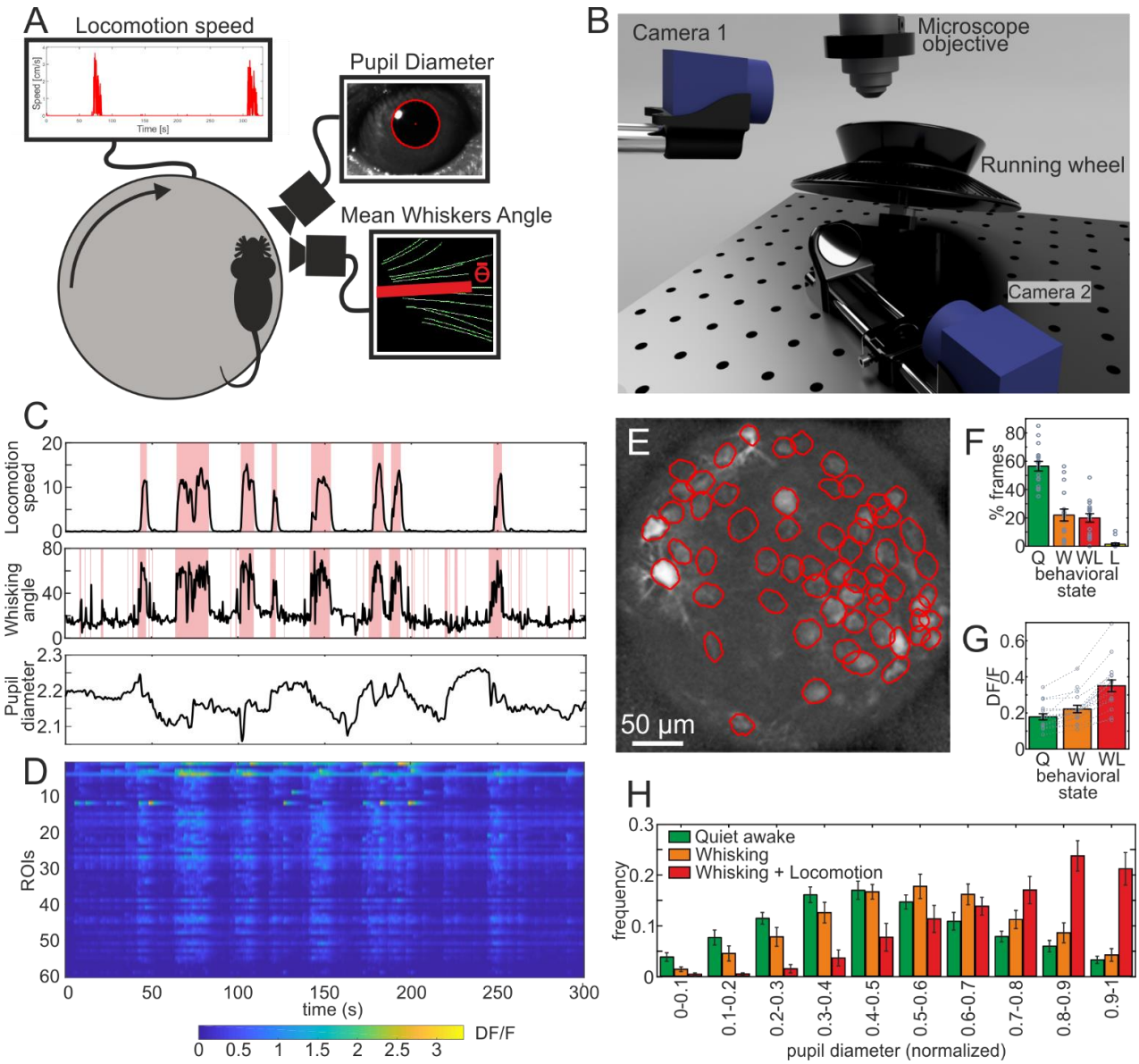

Fig. 38: Experimental set up for the measurement of neuronal population activity in the VPM while monitoring locomotion, whisking, and arousal state

A) Schematic of the experimental set up for the recording of locomotion, mean angle of the whiskers, and pupil size. B) 3D rendering of the set up shown in A). C) Behavioral traces extracted from a typical experimental session. Locomotion is expressed in cm/s, mean angle of the whiskers in degrees, while pupil diameter in mm. D) Pseudocolor matrix representing fluorescence dynamics extracted from regions of interests (ROIs) corresponding to individual neurons, showed as ΔF/F over time. Each line corresponds to a single neuron. E) ROIs associated with the traces showed in D). F) Average of the percentage of time spent in each defined behavior. Each point represents a single experiment. G) Average of the mean ΔF/F across ROIs identified in each defined behavior. Each point represents a single experiment. H) Average across experiments of the percentage of time spent in different behavioral states with different pupil diameters. Error bars in panel E), F), G) display standard errors.

We investigated how neuronal activity is modulated by the behavioral state, in particular by periods in which whisking behavior was detected. We considered neuronal activity both at the single-cell and population levels, identifying, in the latter case, spatio-temporal activity patterns emerging in the VPM. We first quantified the mutual information content about whisking behavior within single neurons (Fig. 39A). Most of the neurons were individually informative about whisking behavior and moreover, these results did not depend on the radial position of cells within the recorded FOVs, suggesting that the information content was homogeneously distributed across the whole FOVs imaged (Fig. 39C). We then evaluated the performances of a support vector machine (SVM) classifier in predicting whisking periods according to fluorescence traces extracted from individual cells. We found good performance for most of the neurons (Fig. 39B), meaning that the activity of most neurons could be individually used to correctly infer the whisking behavior. Similarly in this case, there was no radial dependence of the results (Fig. 39D), suggesting that neuronal activity was homogeneously distributed across space. Nevertheless, on a population level, the classifier performance was modulated by the dimension of FOV considered. Bigger portions of the FOV (hence containing more neurons) were characterized by better performances in the prediction of whisking behavior (Fig. 39E).

At the population level, we applied the non-negative matrix factorization (NMF) method to identify subpopulations of neurons (called modules in Fig. 39F-I) characterized by synchronous activity and hence constituting potential neuronal ensembles underlying whisking behavior. Modules detected were activated differently in time (Fig. 39F) and were sparsely distributed in space (Fig. 39G, H). Moreover, they were modulated, differently by whisking periods. We defined a whisking modulation index (WMI) and found that while the majority of modules was positively modulated by whisking (WMI > 0), the activity of a few modules was suppressed during whisking periods (negatively modulated, WMI < 0). Sparseness of modules appeared to be negatively correlated with the WMI, suggesting that those few modules that were negatively modulated by whisking were also characterized by few, but highly informative neurons (within the ensemble). In contrast, modules with high WMI values were less sparse, suggesting similar activity (and information) across most of the neurons belonging to these ensembles. Notably, single modules covered distances of hundreds of μm (Fig. 39I), spanning the whole eFOV (Fig. 39G).

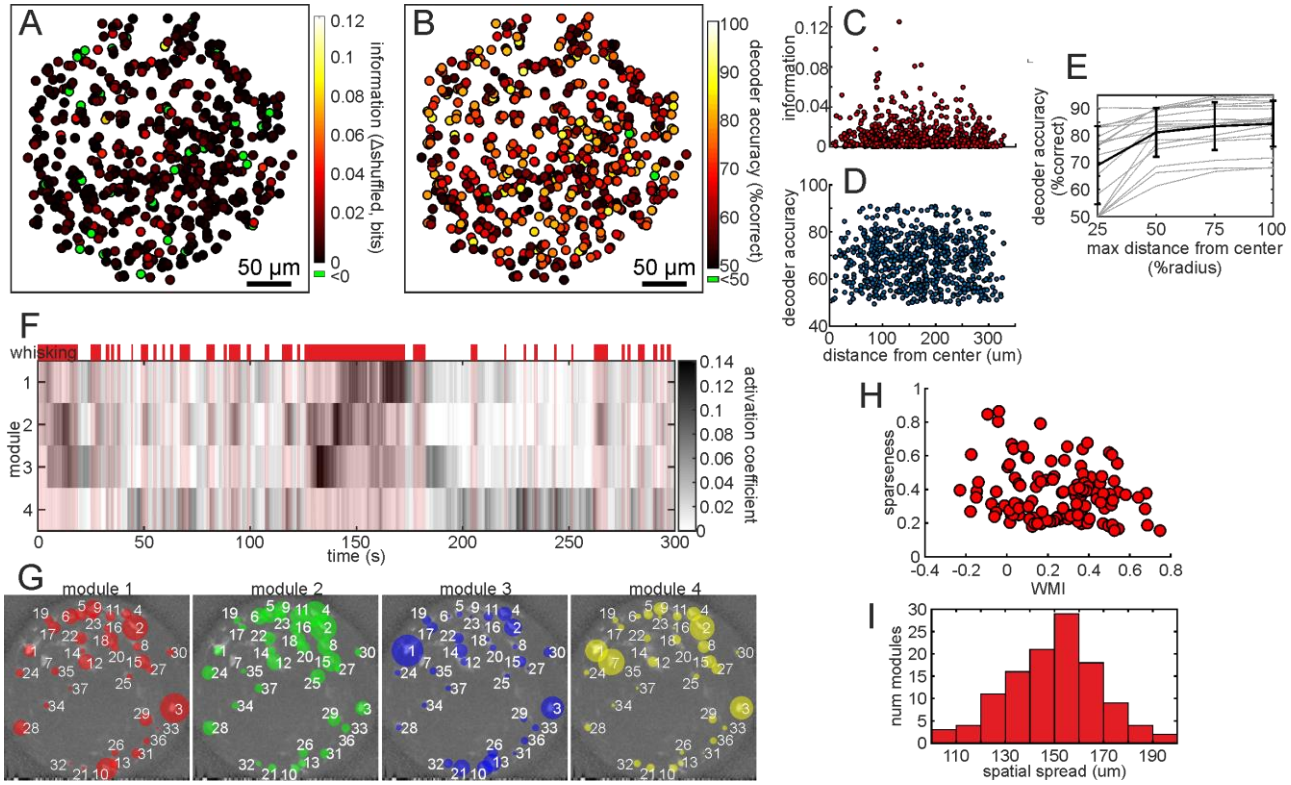

Fig. 39: Information about whisking is homogeneously distributed in VPM and it is characterized by the emergence of sparse spatio-temporal patterns of synchronous activity

A) Whisking information content of all the neurons collected across experiments. B) Performance of an SVM classifier in predicting whisking periods according to fluorescence dynamics of single neurons. C) Whisking information content of single neurons plotted against their radial position. D) Performances of the SVM classifier for each neuron plotted against their radial position. E) Performances of the SVM classifier considering the activity of neuronal populations located within concentric regions of the FOV with different extensions. Grey lines refer to single experiments, while the black line is the average across experiments. F) Activation coefficient across time for the four modules identified in the FOV containing the 37 neurons shown in G). Whisking periods are depicted by red rectangles above the greyscale matrix. Each line correspond to one module. G) Representation of the four modules whose activity coefficient variations are reported in F). Each dot represents a neuron belonging to the specific module and the radius of each dot is proportional to the weight of that neuron within the module. H) Sparseness of each module plotted against its WMI. Each dot represents one module and modules extracted from the same experiment are displayed with the same color. I) Spatial extension of modules.

In order to further quantify the advantages of type II eFOV-microendoscopes compared to uncorrected probes in precisely detecting neuronal activity, we performed simulations in which we simulated two-photon VPM imaging t-series using synthetic data. We compared the results of the simulations with those obtained from preliminary experiments in which imaging in the VPM was

performed on the same preparation with corrected eFOV microendoscopes before and after the removal of the corrective microlens.

For simulations of synthetic fluorescence t-series, neuronal activity within a volumetric distribution of cells was generated and sampled across an imaging focal plane resembling the real one (Fig. 40A), for both the eFOV-microendoscope and the uncorrected probe. Artificial time-series were generated for both conditions, and fluorescence traces were extracted from neurons, together with the corresponding ground truth of neuronal activity. Fig. 40B shows examples of temporal averages of synthetic and real acquisitions, for corrected and uncorrected endoscopes. We found that eFOV-microendoscopes allowed the recording of neuronal activity with better SNR compared to non-corrected probes (Fig. 40C-D), in agreement with the increased axial spatial resolution that was experimentally measured (Fig. 28). Neuronal/region-of-interest (ROI) segmentation (the identification of pixels corresponding to neurons/ROIs) was performed automatically in the case of synthetic data, according to the ground truth and the SNR of fluorescence traces. The number of identified neurons depended on the SNR threshold used for the segmentation and when a higher SNR was required, fewer neurons were identified. Nevertheless, Fig. 40C (upper panel) shows that more neurons were segmented within the higher SNR range in the case of eFOV-microendoscopes. On the other hand, more neurons with a low SNR were segmented in the case of acquisitions with the non-corrected probe. Fig. 40C (lower panel) shows results from real data. In this case, the segmentation was done manually and there was no significant difference in the number of identified neurons with or without the corrective lens in terms of their density. This suggests that the SNR threshold used by the experimenter (based on visual inspection of the time-series) for the segmentation was around 10, where the two curves in the upper panel of Fig. 40C intersect. The same results are depicted in Fig. 40D, where plots representing the SNR characterizing each ROI (left graphs) or averaged across ROIs belonging to the same acquisition (right graphs) are shown for simulated (upper panels) and real (bottom panels) data. Also in this case, the SNR was higher in the case of acquisitions obtained with eFOV-microendoscopes. The same trend was found for real data, although the results did not reach significance, probably due to the low amount of experimental data (Fig. 40D, bottom graphs).

In synthetic data, we evaluated, for each ROI, the correlation with the ground truth fluorescence signal. For those ROIs whose fluorescence dynamics were determined by more than one neuron, the correlation with the second most relevant cell was also calculated. Fig. 40E (left graphs) shows that there was a stronger correlation with the ground truth signals in the case of ROIs segmented from eFOV-microendoscopes acquisitions compared to uncorrected probes. Accordingly, contamination from nearby neurons was higher in uncorrected endoscopes (Fig. 40E, right graphs).

Lastly, we evaluated pairwise activity correlations between the pairs of neurons as a function of the pair distance. Pairs of neurons were selected within two portions of the FOV: central (center) and distal (surround; Fig. 40F). Simulations showed decreased pairwise correlations in eFOV-microendoscopes compared to uncorrected probes, with the value of the pairwise correlation for eFOV-microendoscopes plateauing to the ground truth value. This was especially true for small (< 20 μm) pair distances, within the range in which the pairwise correlation was mainly determined by the size of the PSF volume. In fact, a larger PSF would integrate signals coming from a greater volume comprising more nearby neurons, leading to a greater pairwise correlation.

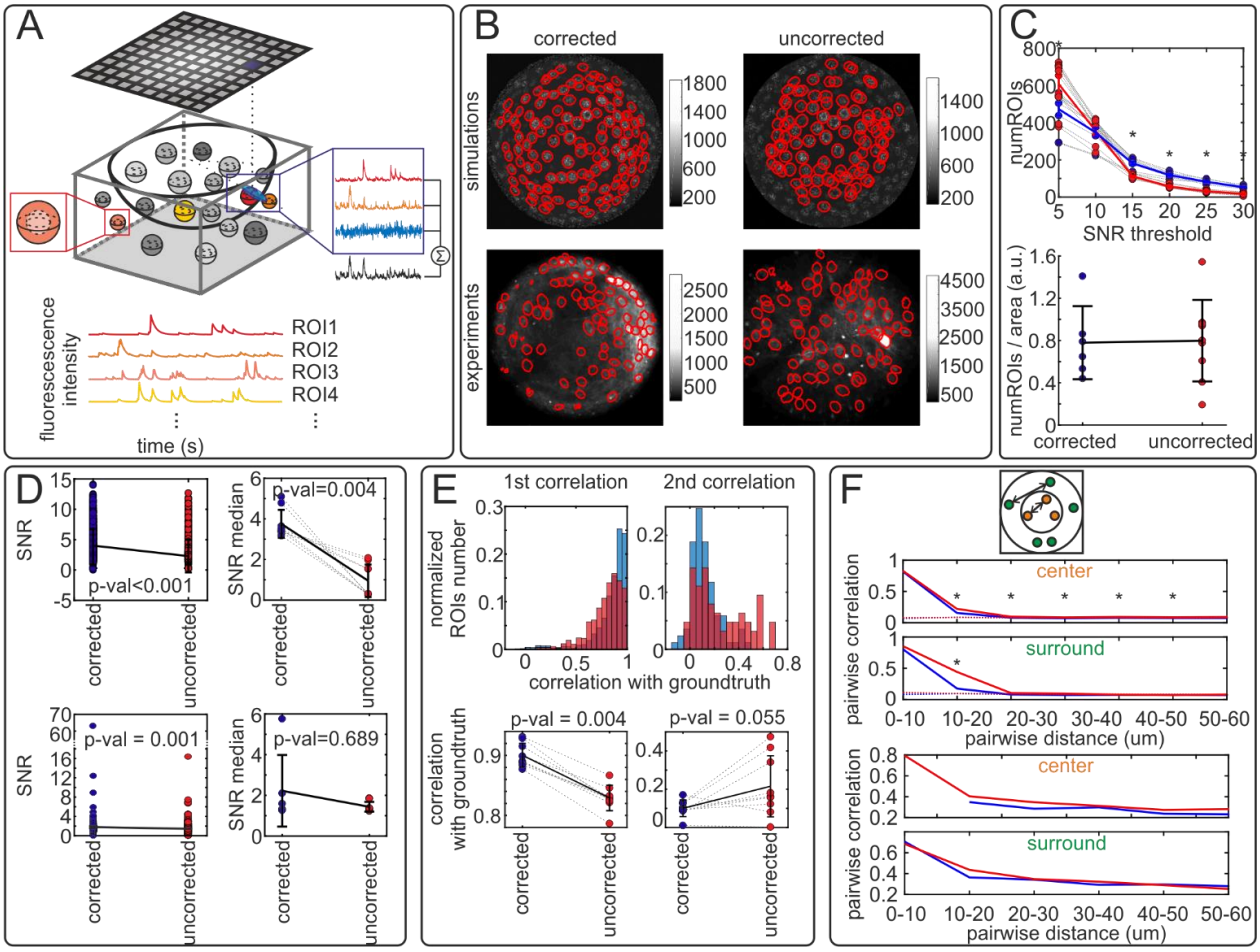

Fig. 40: eFOV microendoscopes allow more accurate evaluation of cellular activity and pairwise correlation

A) Representation of the procedure followed to simulate functional imaging data. Neurons were generated as spheres located in a 3D volume and each neuron had a simulated activity which resembled the measured one. For each position of the curved imaging surface, a volumetric elliptical PSF was generated. Only voxels of neurons falling within the PSF were contributing to the signal collected by imaging. Collected signals were projected on a 2D plane to generate frames and fluorescence dynamics were extracted from pixels corresponding to neurons, identified with an automatic segmentation approach. B) ROIs identified over FOVs for simulations (upper panels) and

experimental data (lower panels). C) Upper panel, number of ROIs identified for simulated data, plotted against the SNR threshold used for the automatic segmentation. Blue line, corrected endoscopes; red line, uncorrected endoscopes (this notation is valid also for D, E, and F). Lower panel, density of neurons identified for corrected and uncorrected endoscopes, experimental data. D) SNR of the fluorescence traces extracted from single neurons (left) and SNR median across ROIs belonging to the same experiments (right) for corrected and uncorrected probes. Upper panels refer to simulations, while bottom panels were obtained from experimental data. E) Correlation with the first or second component of the ground truth shown as histograms for all the traces (upper panels) or as column plots in which each point represents the average value across traces extracted from each simulated experiment. F) Pairwise correlations. Two regions were identified within the FOV, a central region (center) and a border region (surround) as schematized in the skematic on top of the panel. Pairwise correlation values were plotted against pairwise distance separately for the two identified portions of FOV, for simulated (upper graphs) and experimental (lower graphs) data.

We found the decreased pairwise correlation in eFOV-microendoscopes compared to non-corrected probes for both the FOV portions (center and surround), indicating that ROIs corresponding to individual neurons can be accurately segmented across the whole FOV in eFOV-microendoscopes. Preliminary experimental results using eFOV-microendoscopes before and after the removal of the corrective lens showed the same trend observed in simulations, although the results did not reach significance, most likely because of the low number of experiments performed.

Overall, the results of these simulated data show that correcting for optical aberration in eFOV-microendoscopes allows accurate evaluation of single-neuron activity and pairwise correlation over large population of neurons in deep brain regions.

5 Discussion

Major efforts in the development of technology for imaging neuronal activity in vivo are directed to access deep brain regions with minimal tissue damage, while maximizing the area over which imaging can be performed with single-cell resolution. GRIN lenses, alone or in combination with fiber-bundles, have been used to perform one- and two-photon imaging in deep brain areas, such as the hippocampus [257], [260], the striatum [124] and the hypothalamus [124], [261], [262]. GRIN microendoscopes have also been used to perform simultaneous functional imaging of two different brain regions [263], allowing concurrent monitoring of neuronal dynamics in areas otherwise not accessible with single FOV systems.

Even though the combination of GRIN lenses with two-photon imaging benefits of improved optical sectioning, most GRIN endoscopes have been operating with lower resolution, even in two-photon excitation mode, due to optical aberrations lying on and off the optical axis. These aberrations derive from the intrinsic non-aplanatic properties of GRIN rods [264] and limit the usable FOV [123], [134], [140], [265], [266]. Aberrations increase with the length and *NA* of the GRIN lens, making high-resolution imaging of large FOV in deep areas a challenging goal. Aberrations can be partially compensated for by adding additional optical elements, such as a coverglass [133], a single high refractive index plano-convex lens [123], or multiple plano-convex lenses combined with diffractive optical elements [140], [266]. By adding a single plano-convex ball lens to the distal end of a customized GRIN rod (rod diameter: 1 mm), Barretto et al. increased the *NA* up to 0.82 correcting on-axis aberrations, and imaged neuronal dendritic spines in GFP-expressing hippocampal pyramidal neurons in live mice [123]. To correct off-axis aberrations while maintaining high *NA*, at least a second plano-convex lens was needed [140], [266]. Fabrication of high performance multi-element optical systems for on-axis and off-axis aberration correction, however, requires respecting strict tolerances in assembly and requires the use of external metal cannulas to keep the various optical elements aligned and provide mechanical stability to the optical system. This, so far, has limited the applicability of aberration correction with built-in optical elements to GRIN lenses of diameter ≥ 1 mm and overall endoscopic probe diameter (GRIN + cannula) of ≥ 1.4 mm [123], [140], [266]. Since the insertion of the probe irreversibly damages the

tissue above the target area, reducing the size of the probe and consequently its invasiveness is of utmost importance when imaging deep brain regions. However, due to their small radial dimensions, improving optical performances in ultrathin (diameter ≤ 0.5 mm) microendoscopes with built-in optical elements is a major challenge.

Alternatively, aberration correction in GRIN microedoscopes can be achieved using adaptive optics (AO) [134], [136], [264], [265]. For example, using pupil-segmentation methods for AO, diffraction-limited performance across an enlarged FOV was obtained in GRIN-based endoscopes with a diameter of 1.4 mm [134], [265] and, in principle, this approach could be extended to probes with a smaller diameter. AO through pupil segmentation requires significant modification of the optical setup and the use of an active wavefront modulation system (e.g. deformable mirror device or liquid crystal spatial light modulator) which in turn requires the development of ad hoc software control. Moreover, AO through pupil segmentation may limit the temporal resolution of the system, since multiple AO corrective patterns must be applied to obtain an aberration-corrected extended FOV [134].

In this study, we devised a new approach to solve this problem and used TPP [149], [255] to microfabricate polymeric aspheric lenses that effectively corrected aberrations in ultrathin GRIN-based endoscopes. Corrective lenses were fabricated on glass coverslips which were aligned and assembled with the GRIN rod to form an aberration-corrected microendoscope. Importantly, this optical design resulted in improved axial resolution and extended FOV without increasing the lateral size of the probe and thus minimizes tissue damage in biological applications. Compared to AO approaches, the technique developed in this study does not necessitate modification of the optical path nor the development of heavy computational approaches. Moreover, it is easily coupled to standard two-photon set-ups, and does not introduce limitations in the temporal resolution of the imaging system, allowing fast endoscopic microscopy techniques, such as scanless imaging [267].

Despite these advantages, the approach presented in this study is limited to the correction of aberrations introduced by the GRIN lens and was not developed to correct aberrations introduced by other elements along the optical path or by the sample. Moreover, in contrast to AO, our approach does not correct for aberrations that may vary over time, such as those due to intrinsic properties of the biological sample that may dynamically change over the course of the experiment. AO approaches could, for example, be applied to eFOV-microendoscopes to address this limitation.

Using TPP, we fabricated small diameter corrective lenses which significantly enlarged the FOV of ultrathin GRIN microendoscopes. Corrective lenses were specifically designed for each type of GRIN rod used in the endoscope. The profile of aspheric lenses was optimized through optical simulations with the aim of reaching single-cell axial resolution over the largest possible FOV. Given that corrective microlenses had a diameter comparable to that of ultrathin GRIN rods (0.35-0.5 mm), it was not possible to manufacture them with polishing approaches, and we turned to TPP for fabrication. This technology allowed the accurate generation of arbitrary 3D structure over small dimensions (1-500 μm) with high resolution. This method is flexible and can be applied to the GRIN rods of different diameters and lengths that are required to access the numerous deep regions of the mammalian brain.

We characterized the enhanced imaging performance of eFOV-microendoscopes compared to uncorrected probes using a micrometric ruler to estimate the FOV distortion and using subresolved fluorescent beads or layers to evaluate the spatial resolution and the increased extension of FOV. Corrected endoscopes showed improved axial resolution and an up to 9-fold extended FOV, allowing efficient *in vivo* population imaging with minimally invasiveness. We then validated their use in two-photon functional imaging *in vivo*, simultaneously recording the neuronal activity of hundreds of hippocampal cells with minimal invasiveness. Moreover, eFOV-microendoscopes were applied for the study of neuronal spatio-temporal activity patterns across VPM thalamic populations in head-fixed animals. To study the encoding and processing of information in the VPM-wS1 loop under physiological conditions, it is of fundamental importance to preserve both VPM input and output connections. We efficiently applied our ultrathin probes with extended FOV to study the activity of large anatomically-identified neuronal populations in the VPM while preserving most of its connections with wS1. Indeed, we found that the small radial dimension of the eFOV-microendoscopes allowed the preservation of most of the thalamo-cortical and cortico-thalamic connectivity (Fig. 36). Under this imaging condition allowing minimal invasiveness, we examined how neuronal activation in the VPM was modulated by quiet or active animal behaviors and investigated the encoding of whisking information within identified ensembles of neurons. Although VPM is organized in anatomically identified structures, called barreloids, we did not find spatial clusters of neuronal activity. Rather, neuronal activity was distributed homogeneously across the FOV. This may be due to the fact that mice were not whisking on an object or texture but rather in air, and therefore most of the whiskers were undergoing the same movements. Future experiments will be needed to test this hypothesis. Aside from this consideration, the results presented in this work, show that corrected microendoscopic probes represent a powerful, minimally invasive and ready-to-use tool to perform high-resolution functional imaging of large, deep brain networks in awake, head-fixed mice.

Although eFOV-microendoscopes have been primarily applied for functional imaging in this study, we expect that their use can be extended to other applications. For example, eFOV-microendoscopes could be combined with optical systems for two-photon patterned optogenetic manipulations [268]–[270] and for simultaneous functional imaging and optogenetic perturbation [271]–[273]. Moreover, besides their applications in the neuroscience field, eFOV-microendoscopes could be used in a large variety of optical applications requiring minimally invasive probes, ranging from cellular imaging [118], [126] to tissue diagnostics [274], [275]. Importantly, applications of ultrathin eFOV-microendoscopes to other fields of research will be greatly facilitated by the built-in aberration correction method that we developed. This provides a unique degree of flexibility that allows ready-to-use devices to be applied to a large variety of existing optical systems with no major modifications of their optical path.

Regarding future developments of the work presented in this thesis, the aberration correction obtained with one microlens placed in the back aperture of a GRIN rod is just the first of a series of potential optical solutions to improve deep functional imaging in neuroscience. Future development of the method described in this study may include the realization of corrective elements composed of compound microfabricated lenses [131], [220]. This advance could extend the degrees of freedom in the correction design process and lead to improved performance of miniaturized optical probes obtained by the simultaneous compensation of more aberrations. The results presented in this thesis together with preliminary measurements of the shape of the wavefront (using SH sensors) emerging from the distal end of the probes showed that corrective microlenses reduce the amount of astigmatism, coma and spherical aberrations, but leave other types of aberrations unchanged. For example, for each type of eFOV-microendoscope, corrective microlenses were designed to compensate for aberrations at a single working distance. This means that the depth of focus in which aberrations are well-corrected spans a small axial range, which preliminary experiments suggest is about 40 μm. Therefore, when defocusing on different imaging planes at diverse axial positions (by changing the relative distance between the microscope objective and the endoscope), aberration correction will be achieved mostly only in one focal plane. Therefore, one major future direction will be to extend the effects of aberration correction in the axial direction. Such an improvement will be particularly meaningful for endoscopic probes that, once implanted in the tissue, cannot be moved.

Other examples of aberrations still present in eFOV-microendoscopes are field curvature and chromatic aberrations. In eFOV-microendoscopes, the imaging surface is curved rather than being a flat plane (Fig. 29). If the volume of the sample is large enough to completely contain the curved

imaging surface, as is the case in the VPM, field curvature is not a major issue under our experimental conditions, since it does not reduce the information content of images. In contrast, for thin samples such as the stratum piramidale of the hippocampus (Fig. 32), it would be useful to have a planar imaging surface, to have more neurons in the FOV. In principle, for field curvature correction, a specific corrective microlens placed directly on the distal end of the endoscope should work as field flattener. Indeed, auxiliary optical elements that compensate for field curvature are commonly placed near the focal plane and this was the approach used in astronomy with the Schmidt corrector plate (from which the design of the corrective lenses were deriver), that is known to suffer for field curvature.

eFOV-microendoscopes also suffer from chromatic aberrations and this leads illumination light of different wavelengths to be focused at different working distances. Moreover, collected fluorescence photons of different wavelengths emitted from the same focal plane, on their way back through the GRIN rod, will be focused at different positions because of this type of aberration. Under our experimental conditions, in which we used a single point detector, such as a PMT, and not a camera, axial chromatic aberration in the collection path did not particularly affect the performance of the imaging system. Rather, the major constraint of chromatic aberration was the z-shift of different wavelengths along the excitation path. Correcting chromatic aberrations will enable two important classes of experiments, namely dual color functional imaging and all-optical electrophysiology. In both cases, it is fundamental to illuminate the same focal plane simultaneously with two (or eventually more) different wavelengths.

Dual color imaging requires that two different fluorophores are expressed in the sample and that they are simultaneously imaged using two excitation wavelengths. Dual color imaging allows, for example, to investigate the coordinated activity of two different classes of neurons. These types of experiments would be particularly interesting in the VPM. This would require labeling VPM relay cells and axonal inputs coming from specific neuronal populations innervating VPM, such as PrV cells, RTN, or LVI CT neurons with different fluorophores in order to investigate how specific drivers or modulatory inputs affect the firing output activity of VPM relay cells.

Along similar lines, all-optical experiments are based on the expression of both a functional fluorophore (e.g., GCaMP6 or RCaMP) and an opsin with separated excitation spectra. Correction of chromatic aberration would allow the photostimulation of specific cells while simultaneously recording the neuronal activity of the entire population through imaging at a different wavelength. All-optical experiments will be required to causally test the functional role of specific neuronal activity motifs in driving behavior. Given the improved spatial resolution over an enlarged area provided by eFOV-microendoscopes, correction of chromatic aberration in eFOV-microendoscopes

will enable imaging and photostimulation with single-cell resolution over large neuronal populations located in deep brain regions.

The next step in this project is then to improve the imaging performance of eFOV-microendoscopes by designing and fabricating corrective compound microlenses to compensate for chromatic aberrations, defocus, and, potentially, field curvature. In future developments, besides TPP, we will also consider alternative approaches, such as the use of metalenses. Metalenses have become a breakthrough technology for the development of miniaturized optical systems. They are ultrathin, cost-effective and, in principle, a single metalens could be designed for the correction of different aberrations [276]. To this end, we are in contact with Dr. Federico Capasso's group at Harvard University to couple metalenses and GRIN rods [277] for endoscopic applications in neuroscience.

As a further direction in technical development, we have recently been in contact with Dr. Edvard Moser's group to couple eFOV-microendoscopes with the fast high-resolution, miniaturized two-photon microscope (FHIRM-TPM) [278] in freely moving mice.

Besides the technical developments, our goal is to use eFOV-microendoscopes to tackle important physiological questions regarding the processing of whisker movements along the somatosensory pathway. Specifically, we are interested in understanding how information is encoded across anatomically-identified neuronal populations, how the encoding of information is modulated by behavior, and how information is transferred between different neuronal populations. To investigate these open questions, more sophisticated experimental configurations and/or specific behavioral tests than the ones presented in this thesis will be needed.

For example, simultaneous functional imaging in two distant brain regions would be important to understand how information is transferred across synaptically connected networks. Simultaneous imaging through two implanted endoscopes [263] or through an endoscope and a cranial window is feasible, but according to the design reported in [263], requires a substantial modification of the optical set-up. Such an experimental design would make it possible to examine how spatio-temporal activity patterns are transferred between VPM and wS1 in both directions, in order to understand how information is passed from the VPM to cortical LIV and from LVI back to the VPM. In a more complex experimental design, all-optical recordings could be used to investigate how artificial perturbation of neuronal activity affects the activation of neuronal populations located in target brain region. This would enable the study of the transfer function between VPM and wS1 in both directions. Such experiments would require photostimulation and imaging to be performed

simultaneously in two distant regions, for example, coupling an achromatic eFOV-microendoscope and a cranial window.

Finally, to investigate the encoding of information in the VPM using functional fluorescence imaging, it will also be necessary to accurately characterize the relationship between the recorded neuronal fluorescence dynamics and the action potential firing patterns underlying calcium influxes. This is of utmost importance especially for thalamic nuclei, given the characteristic feature of relay cells to encode information in two different AP firing modalities, tonic or bursting [227]. Given the difficulty in performing simultaneous imaging and targeted electrophysiological recordings in vivo, because of the short working distance of GRIN lens-based microendoscopes ($\sim$ 150 μm), we are planning to perform this experiment in a brain slice preparation, in which the microendoscope approaches the sample from the bottom of the slice and the electrophysiological recording is performed from the top.

6 References

[1] E. R. Kandel, J. H. Schwartz, T. M. Jessell, S. A. Siegelbaum, and A. J. Hudspeth, *Principles of Neural Science*. 2014.

[2] M. F. Bear, B. W. Connors, and M. A. Paradiso, *Neuroscience: Exploring the Brain*. 2015.

[3] D. Purves, G. J. Augustine, D. Fitzpatrick, W. Hall, and A.-S. Lamantia, *Neuroscience*. Sinauer Associates Inc, 2011.

[4] R. Yuste, "From the neuron doctrine to neural networks," 2015.

[5] Z. F. Mainen and T. J. Seinowski, "Reliability of spike timing in neocortical neurons," *Science (80-.).*, vol. 268, no. 5216, pp. 1503–1506, 1995.

[6] M. R. Cohen and J. H. R. Maunsell, "Attention improves performance primarily by reducing interneuronal correlations," *Nat. Neurosci.*, vol. 12, no. 12, pp. 1594–1600, Dec. 2009.

[7] G. Buzsáki, *Rhythms of the Brain*. Oxford University Press, 2006.

[8] D. H. O'Connor, D. Huber, and K. Svoboda, "Reverse engineering the mouse brain," *Nature*, vol. 461, no. 7266. pp. 923–929, 15-Oct-2009.

[9] S. Bovetti and T. Fellin, "Optical dissection of brain circuits with patterned illumination through the phase modulation of light," *Journal of Neuroscience Methods*, vol. 241. Elsevier, pp. 66–77, 05-Feb-2015.

[10] G. Buzsáki, C. A. Anastassiou, and C. Koch, "The origin of extracellular fields and currents-EEG, ECoG, LFP and spikes," *Nature Reviews Neuroscience*, vol. 13, no. 6. pp. 407–420, Jun-2012.

[11] T. W. Margrie *et al.*, "Targeted whole-cell recordings in the mammalian brain in vivo," *Neuron*, vol. 39, no. 6, pp. 911–918, Sep. 2003.

[12] D. H. Hubel and T. N. Wiesel, "Receptive fields of single neurones in the cat's striate cortex," *J. Physiol.*, vol. 148, no. 3, pp. 574–591, Oct. 1959.

[13] D. A. Dombeck, C. D. Harvey, L. Tian, L. L. Looger, and D. W. Tank, "Functional imaging of hippocampal place cells at cellular resolution during virtual navigation," *Nat. Neurosci.*, vol. 13, no. 11, pp. 1433–1440, Nov. 2010.

[14] R. C. Craddock *et al.*, "Imaging human connectomes at the macroscale," *Nature Methods*, vol. 10, no. 6. pp. 524–539, Apr-2013.

[15] K. Uğurbil *et al.*, "Pushing spatial and temporal resolution for functional and diffusion MRI in the Human Connectome Project," *Neuroimage*, vol. 80, pp. 80–104, Oct. 2013.

[16] D. C. Van Essen, S. M. Smith, D. M. Barch, T. E. J. Behrens, E. Yacoub, and K. Ugurbil, "The WU-Minn Human Connectome Project: An overview," *Neuroimage*, vol. 80, pp. 62–79, Oct. 2013.

[17] K. Ohki, S. Chung, Y. H. Ch'ng, P. Kara, and R. C. Reid, "Functional imaging with cellular resolution reveals precise microarchitecture in visual cortex," *Nature*, vol. 433, no. 7026. pp. 597–603, 10-Feb-2005.

[18] D. Shoham *et al.*, "Imaging cortical dynamics at high spatial and temporal resolution with novel blue voltage-sensitive dyes," *Neuron*, vol. 24, no. 4, pp. 791–802, 1999.

[19] C. Grienberger and A. Konnerth, "Imaging Calcium in Neurons," *Neuron*, vol. 73, no. 5. pp. 862–885, 08-Mar-2012.

[20] S. Bovetti, C. Moretti, and T. Fellin, "Mapping brain circuit function in vivo using two-photon fluorescence microscopy.," *Microsc. Res. Tech.*, vol. 77, no. 7, pp. 492–501, Jul. 2014.

[21] W. Yang and R. Yuste, "In vivo imaging of neural activity," *Nat. Methods*, vol. 14, no. 4, pp. 349–359, 2017.

[22] J. E. Markus Sauer, Johan Hofkens, *Handbook of Fluorescence Spectroscopy and Imaging: From Single Molecules to Ensembles*. 2011.

[23] W. Gong *et al.*, "Redefining the photo-stability of common fluorophores with triplet state quenchers: mechanistic insights and recent updates," *Chem. Commun.*, vol. 55, no. 60, pp. 8695–8704, 2019.

[24] U. Kubitscheck, *Fluorescence Microscopy From Principles to Biological Applications*. 2013.

[25] A. Mondal, Partha Pratim Diaspro, *Fundamentals of Fluorescence Microscopy Exploring Life with Light*. 2014.

[26] M. Göppert-Mayer, "Über Elementarakte mit zwei Quantensprüngen," *Ann. Phys.*, vol. 401, no. 3, pp. 273–294, 1931.

[27] G. Kaiser and C. G. B. Garrett, "Two-photon excitation in CaF2: Eu2+," *Phys. Rev. Lett.*, vol. 7, no. 6, 1961.

[28] W. Denk, J. H. Strickler, and W. W. Webb, "Two-photon laser scanning fluorescence microscopy," *Science (80-.).*, vol. 248, no. 4951, pp. 73–76, 1990.

[29] M. Drobizhev, N. S. Makarov, S. E. Tillo, T. E. Hughes, and A. Rebane, "Two-photon absorption properties of fluorescent proteins," *Nature Methods*, vol. 8, no. 5. pp. 393–399,

May-2011.

[30] J. P. Zinter and M. J. Levene, “Maximizing fluorescence collection efficiency in multiphoton microscopy,” *Opt. Express*, vol. 19, no. 16, p. 15348, 2011.

[31] L.-C. Cheng *et al.*, “Measurements of multiphoton action cross sections for multiphoton microscopy References and links,” 2014.

[32] K. Isobe, W. Watanabe, and K. Itoh, *Functional Imaging by Controlled Nonlinear Optical Phenomena*. Hoboken, NJ, USA: John Wiley & Sons, Inc., 2013.

[33] S. Kalies, K. Kuetemeyer, and A. Heisterkamp, “Mechanisms of high-order photobleaching and its relationship to intracellular ablation,” *Biomed. Opt. Express*, vol. 2, no. 4, p. 805, Apr. 2011.

[34] G. H. Patterson and D. W. Piston, “Photobleaching in two-photon excitation microscopy,” *Biophys. J.*, vol. 78, no. 4, pp. 2159–2162, 2000.

[35] T. S. Chen, S. Q. Zeng, Q. M. Luo, Z. H. Zhang, and W. Zhou, “High-order photobleaching of Green fluorescent protein inside live cells in Two-photon excitation microscopy,” *Biochem. Biophys. Res. Commun.*, vol. 291, no. 5, pp. 1272–1275, 2002.

[36] G. Donnert, C. Eggeling, and S. W. Hell, “Major signal increase in fluorescence microscopy through dark-state relaxation,” *Nat. Methods*, vol. 4, no. 1, pp. 81–86, Jan. 2007.

[37] N. Ji, J. C. Magee, and E. Betzig, “High-speed, low-photodamage nonlinear imaging using passive pulse splitters,” *Nat. Methods*, vol. 5, no. 2, pp. 197–202, Feb. 2008.

[38] A. M. Larson, “Multiphoton microscopy,” *Nat. Photonics*, vol. 5, no. 1, pp. 1–1, Jan. 2011.

[39] W. R. Zipfel, R. M. Williams, and W. W. Webb, “Nonlinear magic: Multiphoton microscopy in the biosciences,” *Nat. Biotechnol.*, vol. 21, no. 11, pp. 1369–1377, 2003.

[40] N. Ji, J. Freeman, and S. L. Smith, “Technologies for imaging neural activity in large volumes,” *Nat. Neurosci.*, vol. 19, no. 9, pp. 1154–1164, 2016.

[41] P. T. C. So, “Two-photon Fluorescence Light Microscopy,” 2002.

[42] M. Y. Berezin and S. Achilefu, “Fluorescence Lifetime Measurements and Biological Imaging.”

[43] K. F. Wall and A. Sanchez, “Titanium sapphire lasers,” *Rev. Laser Eng.*, vol. 21, no. 1, pp. 73–76, 1993.

[44] A. N. Yaroslavsky, P. C. Schulze, I. V. Yaroslavsky, R. Schober, F. Ulrich, and H. J. Schwarzmaier, “Optical properties of selected native and coagulated human brain tissues in vitro in the visible and near infrared spectral range,” *Phys. Med. Biol.*, vol. 47, no. 12, pp. 2059–2073, Jun. 2002.

[45] F. Helmchen and W. Denk, “Deep tissue two-photon microscopy,” *Nat. Methods*, vol. 2, no. 12, pp. 932–940, 2005.

[46] P. Theer, M. T. Hasan, and W. Denk, “Two-photon imaging to a depth of 1000 μm in living brains by use of a Ti:Al_2O_3 regenerative amplifier,” *Opt. Lett.*, vol. 28, no. 12, p. 1022, 2003.

[47] D. Kobat, N. G. Horton, and C. Xu, “In vivo two-photon microscopy to 1.6-mm depth in mouse cortex,” *J. Biomed. Opt.*, vol. 16, no. 10, p. 106014, 2011.

[48] N. G. Horton *et al.*, “In vivo three-photon microscopy of subcortical structures within an intact mouse brain,” *Nat. Photonics*, vol. 7, no. 3, pp. 205–209, Mar. 2013.

[49] G. Katona *et al.*, “Fast two-photon in vivo imaging with three-dimensional random-access scanning in large tissue volumes.,” *Nat. Methods*, vol. 9, no. 2, pp. 201–8, Jan. 2012.

[50] T. Fernández-Alfonso *et al.*, “Monitoring synaptic and neuronal activity in 3D with synthetic and genetic indicators using a compact acousto-optic lens two-photon microscope.,” *J. Neurosci. Methods*, vol. 222, pp. 69–81, Jan. 2014.

[51] Y. Bando, C. Grimm, V. H. Cornejo, and R. Yuste, “Genetic voltage indicators,” *BMC Biol.*, vol. 17, no. 1, Dec. 2019.

[52] M. Kannan, G. Vasan, and V. A. Pieribone, “Optimizing strategies for developing genetically encoded voltage indicators,” *Frontiers in Cellular Neuroscience*, vol. 13. Frontiers Media S.A., pp. 1–17, 29-Jan-2019.

[53] M. Kannan *et al.*, “Fast, in vivo voltage imaging using a red fluorescent indicator,” *Nat. Methods*, vol. 15, no. 12, pp. 1108–1116, Dec. 2018.

[54] T. Knöpfel, “Genetically encoded optical indicators for the analysis of neuronal circuits.,” *Nat. Rev. Neurosci.*, vol. 13, no. 10, pp. 687–700, Oct. 2012.

[55] T. Terai and T. Nagano, “Small-molecule fluorophores and fluorescent probes for bioimaging.,” *Pflugers Arch.*, vol. 465, no. 3, pp. 347–59, Mar. 2013.

[56] V. Pérez Koldenkova and T. Nagai, “Genetically encoded Ca(2+) indicators: properties and evaluation.,” *Biochim. Biophys. Acta*, vol. 1833, no. 7, pp. 1787–97, Jul. 2013.

[57] P. G. Haydon, “Glia: Listening and talking to the synapse,” *Nat. Rev. Neurosci.*, vol. 2, no. 3, pp. 185–193, 2001.

[58] A. Volterra and J. Meldolesi, “Astrocytes, from brain glue to communication elements: the revolution continues.,” *Nat. Rev. Neurosci.*, vol. 6, no. 8, pp. 626–40, Aug. 2005.

[59] T. Fellin, “Communication between neurons and astrocytes: relevance to the modulation of synaptic and network activity.,” *J. Neurochem.*, vol. 108, no. 3, pp. 533–44, Feb. 2009.

[60] G. Losi *et al.*, “New Tools to Study Astrocyte Ca 2+ Signal Dynamics in Brain Networks In Vivo,” 2017.

[61] T. W. Chen *et al.*, “Ultrasensitive fluorescent proteins for imaging neuronal activity,” *Nature*, vol. 499, no. 7458, pp. 295–300, 2013.

[62] E. B. Ridgway and C. C. Ashley, “Calcium transients in single muscle fibers,” *Biochem. Biophys. Res. Commun.*, vol. 29, no. 2, pp. 229–234, Oct. 1967.

[63] O. Shimomura, F. H. Johnson, and Y. Saiga, “Extraction, purification and properties of aequorin, a bioluminescent,” *J. Cell. Comp. Physiol.*, vol. 59, pp. 223–239, 1962.

[64] R. Y. Tsien, “New Calcium Indicators and Buffers with High Selectivity Against Magnesium and Protons: Design, Synthesis, and Properties of Prototype Structures,” *Biochemistry*, vol. 19, no. 11, pp. 2396–2404, 1980.

[65] R. Y. Tsien, “A non-disruptive technique for loading calcium buffers and indicators into cells,” *Nature*, vol. 290, no. 5806, pp. 527–528, 1981.

[66] G. Grynkiewicz, M. Poenie, and R. Y. Tsien, “A new generation of Ca2+ indicators with greatly improved fluorescence properties,” *Journal of Biological Chemistry*, vol. 260, no. 6. pp. 3440–3450, 1985.

[67] C. Stosiek, O. Garaschuk, K. Holthoff, and A. Konnerth, “In vivo two-photon calcium imaging of neuronal networks,” 2003.

[68] G. Y. Wiederschain, “The Molecular Probes handbook. A guide to fluorescent probes and labeling technologies,” *Biochem.*, vol. 76, no. 11, pp. 1276–1276, Nov. 2011.

[69] F. Helmchen and J. Waters, “Ca2+ imaging in the mammalian brain in vivo,” *Eur. J. Pharmacol.*, vol. 447, no. 2–3, pp. 119–129, Jul. 2002.

[70] A. Miyawaki *et al.*, “Fluorescent indicators for Ca2+ based on green fluorescent proteins and calmodulin,” vol. 388, no. August, pp. 882–887, 1997.

[71] T. Knöpfel, J. Díez-García, and W. Akemann, “Optical probing of neuronal circuit dynamics: Genetically encoded versus classical fluorescent sensors,” *Trends in Neurosciences*, vol. 29, no. 3. pp. 160–166, Mar-2006.

[72] L. L. Looger and O. Griesbeck, “Genetically encoded neural activity indicators,” *Current Opinion in Neurobiology*, vol. 22, no. 1. pp. 18–23, Feb-2012.

[73] V. Pérez Koldenkova and T. Nagai, “Genetically encoded Ca2+ indicators: Properties and evaluation,” *Biochim. Biophys. Acta - Mol. Cell Res.*, vol. 1833, no. 7, pp. 1787–1797, Jul. 2013.

[74] M. Ohkura, M. Matsuzaki, H. Kasai, K. Imoto, and J. Nakai, “Genetically encoded bright Ca2+ probe applicable for dynamic Ca2+ imaging of dendritic spines.,” *Anal. Chem.*, vol. 77, no. 18, pp. 5861–9, Sep. 2005.

[75] Y. M. Tallini *et al.*, “Imaging cellular signals in the heart in vivo: Cardiac expression of the high-signal Ca2+ indicator GCaMP2,” *Proc. Natl. Acad. Sci. U. S. A.*, vol. 103, no. 12, pp. 4753–4758, Mar. 2006.

[76] L. Tian *et al.*, “Imaging neural activity in worms, flies and mice with improved GCaMP

calcium indicators," *Nat. Methods*, vol. 6, no. 12, pp. 875–881, 2009.

[77] K. Horikawa *et al.*, "Spontaneous network activity visualized by ultrasensitive Ca 2+ indicators, yellow Cameleon-Nano," *Nat. Methods*, vol. 7, no. 9, pp. 729–732, Sep. 2010.

[78] A. E. Palmer, Y. Qin, J. G. Park, and J. E. Mccombs, "Design and application of genetically encoded biosensors," *Trends Biotechnol.*, vol. 29, pp. 144–152, 2011.

[79] J. Akerboom *et al.*, "Optimization of a GCaMP calcium indicator for neural activity imaging," *J. Neurosci.*, vol. 32, no. 40, pp. 13819–13840, Oct. 2012.

[80] J. Akerboom *et al.*, "Genetically encoded calcium indicators for multi-color neural activity imaging and combination with optogenetics," *Front. Mol. Neurosci.*, no. FEB, Feb. 2013.

[81] G. S. Baird, D. A. Zacharias, and R. Y. Tsien, "Circular permutation and receptor insertion within green fluorescent proteins," *Proc. Natl. Acad. Sci. U. S. A.*, vol. 96, no. 20, pp. 11241–11246, Sep. 1999.

[82] J. Nakai, M. Ohkura, and K. Imoto, "A high signal-to-noise ca2+ probe composed of a single green fluorescent protein," *Nat. Biotechnol.*, vol. 19, no. 2, pp. 137–141, 2001.

[83] J. Akerboom *et al.*, "Crystal structures of the GCaMP calcium sensor reveal the mechanism of fluorescence signal change and aid rational design," *J. Biol. Chem.*, vol. 284, no. 10, pp. 6455–6464, Mar. 2009.

[84] Y. Zhao *et al.*, "An expanded palette of genetically encoded Ca2+ indicators," *Science (80-.).*, vol. 333, no. 6051, pp. 1888–1891, Sep. 2011.

[85] M. Ohkura, T. Sasaki, C. Kobayashi, Y. Ikegaya, and J. Nakai, "An improved genetically encoded red fluorescent Ca2+ indicator for detecting optically evoked action potentials," *PLoS One*, vol. 7, no. 7, Jul. 2012.

[86] K. Svoboda and R. Yasuda, "Principles of two-photon excitation microscopy and its applications to neuroscience.," *Neuron*, vol. 50, no. 6, pp. 823–39, Jun. 2006.

[87] K. Ohki, S. Chung, P. Kara, M. Hübener, T. Bonhoeffer, and R. C. Reid, "Highly ordered arrangement of single neurons in orientation pinwheels," *Nature*, vol. 442, no. 7105, pp. 925–928, Aug. 2006.

[88] H. Ko *et al.*, "The emergence of functional microcircuits in visual cortex," *Nature*, vol. 496, no. 7443, pp. 96–100, Apr. 2013.

[89] B. F. Grewe, D. Langer, H. Kasper, B. M. Kampa, and F. Helmchen, "High-speed in vivo calcium imaging reveals neuronal network activity with near-millisecond precision," *Nat. Methods*, vol. 7, no. 5, pp. 399–405, May 2010.

[90] X. Chen, N. L. Rochefort, B. Sakmann, and A. Konnerth, "Reactivation of the Same Synapses during Spontaneous Up States and Sensory Stimuli," *Cell Rep.*, vol. 4, no. 1, pp. 31–39, Jul. 2013.

[91] N. J. Sofroniew, D. Flickinger, J. King, and K. Svoboda, “A large field of view two-photon mesoscope with subcellular resolution for in vivo imaging,” pp. 1–20, 2016.

[92] M. Born and E. Wolf, *Principles of optics*. Cambridge University Press, 1999.

[93] W. J. Smith, *Modern Optical Engineering. The Design of Optical Systems*, Fourth edi. 2008.

[94] J. E. Greivenkamp, *Field Guide to Geometrical Optics*. 2004.

[95] J. Bentley and C. Olson, *Field Guide to Lens Design*. 2012.

[96] J. C. Wyant and K. Creath, “Basic Wavefront Aberration Theory for Optical Metrology,” 1992.

[97] K. Rahbar, K. Faez, and E. Attaran Kakhki, “Phase wavefront aberration modeling using Zernike and pseudo-Zernike polynomials,” *J. Opt. Soc. Am. A*, vol. 30, no. 10, p. 1988, 2013.

[98] J. Holtzman, “ASTRONOMY 535 OBSERVATIONAL TECHNIQUES CLASS NOTES Fall 2019.” [Online]. Available: http://ganymede.nmsu.edu/holtz/a535/ay535notes/.

[99] R. Garner and B. Dunbar, “Hubble’s Mirror Flaw,” 2017. [Online]. Available: https://www.nasa.gov/content/hubbles-mirror-flaw.

[100] N. Ji, “The practical and fundamental limits of optical imaging in mammalian brains,” *Neuron*, vol. 83, no. 6, pp. 1242–1245, 2014.

[101] N. Ji, D. E. Milkie, and E. Betzig, “Adaptive optics via pupil segmentation for high-resolution imaging in biological tissues,” *Nat. Methods*, vol. 7, no. 2, pp. 141–147, Feb. 2010.

[102] C. Wang *et al.*, “Multiplexed aberration measurement for deep tissue imaging in vivo,” *Nat. Methods*, vol. 11, no. 10, pp. 1037–1040, Jan. 2014.

[103] C. Rodríguez and N. Ji, “Adaptive optical microscopy for neurobiology,” *Curr. Opin. Neurobiol.*, vol. 50, pp. 83–91, 2018.

[104] N. Matsumoto, A. Konno, T. Inoue, and S. Okazaki, “Aberration correction considering curved sample surface shape for non-contact two-photon excitation microscopy with spatial light modulator,” *Sci. Rep.*, vol. 8, 2018.

[105] C. Tischbirek, A. Birkner, H. Jia, B. Sakmann, and A. Konnerth, “Deep two-photon brain imaging with a red-shifted fluorometric Ca $^{2+}$ indicator,” *Proc. Natl. Acad. Sci.*, vol. 112, no. 36, pp. 11377–11382, 2015.

[106] J. D. Wilson and T. H. Foster, “Mie theory interpretations of light scattering from intact cells,” *Opt. Lett.*, vol. 30, no. 18, p. 2442, Sep. 2005.

[107] H. F. Zhang, K. Maslov, G. Stoica, and L. V. Wang, “Functional photoacoustic microscopy for high-resolution and noninvasive in vivo imaging,” *Nat. Biotechnol.*, vol. 24, no. 7, pp. 848–851, Jul. 2006.

[108] K. Si, R. Fiolka, and M. Cui, “Fluorescence imaging beyond the ballistic regime by

ultrasound-pulse-guided digital phase conjugation," 2012.

[109] D. Vučinić, T. M. Bartol, and T. J. Sejnowski, "Hybrid reflecting objectives for functional multiphoton microscopy in turbid media," 2006.

[110] N. K. Logothetis, J. Pauls, M. Augath, T. Trinath, and A. Oeltermann, "Neurophysiological investigation of the basis of the fMRI signal," *Nature*, vol. 412, no. 6843, pp. 150–157, Jul. 2001.

[111] J. C. Jung and M. J. Schnitzer, "Multiphoton endoscopy," *Opt. Lett.*, vol. 28, no. 11, pp. 902–904, 2003.

[112] M. J. Levene *et al.*, "In Vivo Multiphoton Microscopy of Deep Brain Tissue," pp. 1908–1912, 2004.

[113] J. C. Jung, A. D. Mehta, E. Aksay, R. Stepnoski, and M. J. Schnitzer, "In Vivo Mammalian Brain Imaging Using One- and Two-Photon Fluorescence Microendoscopy," pp. 3121–3133, 2004.

[114] B. A. Flusberg, E. D. Cocker, W. Piyawattanametha, J. C. Jung, E. L. M. Cheung, and M. J. Schnitzer, "Fiber-optic fluorescence imaging," *Nature Methods*, vol. 2, no. 12. pp. 941–950, Dec-2005.

[115] B. A. Wilt, L. D. Burns, E. T. Wei Ho, K. K. Ghosh, E. A. Mukamel, and M. J. Schnitzer, "Advances in Light Microscopy for Neuroscience," *Annu. Rev. Neurosci.*, vol. 32, no. 1, pp. 435–506, Jun. 2009.

[116] R. P. J. Barretto and M. J. Schnitzer, "In vivo optical microendoscopy for imaging cells lying deep within live tissue," *Cold Spring Harb. Protoc.*, vol. 7, no. 10, pp. 1029–1034, 2012.

[117] B. A. Flusberg *et al.*, "High-speed, miniaturized fluorescence microscopy in freely moving mice," *Nat. Methods*, vol. 5, no. 11, pp. 935–938, 2008.

[118] J. K. Kim *et al.*, "Fabrication and operation of GRIN probes for in vivo fluorescence cellular imaging of internal organs in small animals," 2012.

[119] M. M. G. Velasco *et al.*, "In vivo two-photon microscopy of the hippocampus using glass plugs," *Biomed. Opt. Express*, vol. 5, no. 6, pp. 1700–1708, 2014.

[120] T. Chia and M. J. Levene, "Microprisms for in vivo multiphoton microscopy of mouse cortex," in *Biomedical Optics and 3-D Imaging*, 2010, p. BMC7.

[121] I. Riemann *et al.*, "Two-photon imaging using a flexible endoscope," in *Endoscopic Microscopy III*, 2008, vol. 6851, p. 68510B.

[122] S. Sivankutty, E. R. Andresen, R. Cossart, G. Bouwmans, S. Monneret, and H. Rigneault, "Ultra-thin rigid endoscope: two-photon imaging through a graded-index multi-mode fiber," *Opt. Express*, vol. 24, no. 2, p. 825, Jan. 2016.

[123] R. P. J. Barretto, B. Messerschmidt, M. J. Schnitzer, and N. America, "In vivo fluorescence

imaging with high-resolution microlenses," *Nat. Methods*, vol. 6, no. 7, pp. 511–512, 2009.

[124] M. E. Bocarsly, W. Jiang, C. Wang, J. T. Dudman, N. Ji, and Y. Aponte, "Minimally invasive microendoscopy system for in vivo functional imaging of deep nuclei in the mouse brain," *Biomed. Opt. Express*, vol. 6, no. 11, pp. 223–228, 2015.

[125] Y. Wu and X. Li, "Two-photon Fluorescence Endomicroscopy," in *Advances in Lasers and Electro Optics*, InTech, 2010.

[126] K. K. Ghosh *et al.*, "Miniaturized integration of a fluorescence microscope," vol. 8, no. 10, 2011.

[127] D. Aharoni, B. S. Khakh, A. J. Silva, and P. Golshani, "All the light that we can see: a new era in miniaturized microscopy," *Nature Methods*, vol. 16, no. 1. Nature Publishing Group, pp. 11–13, 01-Jan-2019.

[128] F. Bociort, "Imaging properties of gradient-index lenses," 1994.

[129] GRINTech GmbH, "Gradient Index (GRIN) Lenses."

[130] www.grintech.de, "GRINTECH GmbH product information." .

[131] R. P. J. Barretto *et al.*, "Time-lapse imaging of disease progression in deep brain areas using fluorescence microendoscopy," *Nat. Med.*, vol. 17, no. 2, pp. 223–229, 2011.

[132] R. P. J. Barretto, "Optical microendoscopy for imaging cells deep within live tissue," 2010.

[133] T. A. Murray and M. J. Levene, "Singlet gradient index lens for deep in vivo multiphoton microscopy," *J. Biomed. Opt.*, vol. 17, no. 2, p. 021106, 2012.

[134] C. Wang and N. Ji, "Characterization and improvement of three-dimensional imaging performance of GRIN-lens-based two-photon fluorescence endomicroscopes with adaptive optics," *Opt. Express*, vol. 21, no. 22, pp. 27142–27154, 2013.

[135] C. Wang and N. Ji, "Pupil-segmentation-based adaptive optical correction of a high-numerical-aperture gradient refractive index lens for two-photon fluorescence endoscopy," *Opt. Lett.*, vol. 37, no. 11, 2012.

[136] F. Bortoletto, C. Bonoli, P. Panizzolo, C. D. Ciubotaru, and F. Mammano, "Multiphoton Fluorescence Microscopy with GRIN Objective Aberration Correction by Low Order Adaptive Optics," *PLoS One*, vol. 6, no. 7, pp. 1–8, 2011.

[137] W. M. Lee and S. H. Yun, "Adaptive aberration correction of GRIN lenses for confocal endomicroscopy," *Opt. Lett.*, vol. 36, no. 23, p. 4608, Dec. 2011.

[138] B. Messerschmidt *et al.*, "Novel concept of GRIN optical systems for high resolution microendoscopy: Part 1. Physical aspects," *Endosc. Microsc. II*, vol. 6432, p. 643202, 2007.

[139] D. C. Leiner and R. Prescott, "Correction of chromatic aberrations in GRIN endoscopes," *Appl. Opt.*, vol. 22, no. 3, p. 383, 1983.

[140] G. Matz, B. Messerschmidt, and H. Gross, "Design and evaluation of new color-corrected

rigid endomicroscopic high NA GRIN-objectives with a sub-micron resolution and large field of view," *Opt. Express*, vol. 24, no. 10, p. 10987, 2016.

[141] P. Zirak *et al.*, "A rigid coherent anti-Stokes Raman scattering endoscope with high resolution and a large field of view," *APL Photonics*, vol. 3, no. 9, 2018.

[142] S. Maruo, O. Nakamura, and S. Kawata, "Three-dimensional microfabrication with two-photon-absorbed photopolymerization," *Opt. Lett.*, vol. 22, no. 2, p. 132, Jan. 1997.

[143] H. B. Sun and S. Kawata, "Two-photon photopolymerization and 3D lithographic microfabrication," *Adv. Polym. Sci.*, vol. 170, pp. 169–273, 2004.

[144] X. Zhou, Y. Hou, and J. Lin, "A review on the processing accuracy of two-photon polymerization," *AIP Adv.*, vol. 5, no. 3, 2015.

[145] H. Sun, T. Tanaka, and S. Kawata, "Three-dimensional focal spots related to two-photon excitation," vol. 80, no. 20, pp. 3673–3676, 2002.

[146] K. Sugioka and Y. Cheng, "Ultrafast lasers — reliable tools for advanced materials processing," *Light Sci. Appl.*, vol. 3, 2014.

[147] A. Ovsianikov, *Investigation of Two-Photon Polymerization Technique for Applications in Photonics and Biomedicine*. 2009.

[148] R. Guo, S. Xiao, X. Zhai, J. Li, and A. Xia, "Micro lens fabrication by means of femtosecond two photon photopolymerization," vol. 14, no. 2, pp. 810–816, 2006.

[149] C. Liberale *et al.*, "Micro-optics fabrication on top of optical fibers using two-photon lithography," *IEEE Photonics Technol. Lett.*, vol. 22, no. 7, pp. 474–476, 2010.

[150] Q. Geng, D. Wang, P. Chen, and S. C. Chen, "Ultrafast multi-focus 3-D nano-fabrication based on two-photon polymerization," *Nat. Commun.*, vol. 10, no. 1, pp. 1–7, 2019.

[151] S. Panzeri, C. D. Harvey, E. Piasini, P. E. Latham, and T. Fellin, "Cracking the Neural Code for Sensory Perception by Combining Statistics, Intervention, and Behavior," *Neuron*, vol. 93, pp. 491–507, 2017.

[152] K. Deisseroth, "Optogenetics," *Nat. Methods*, vol. 8, pp. 26–29, 2011.

[153] E. S. Boyden, F. Zhang, E. Bamberg, G. Nagel, and K. Deisseroth, "Millisecond-timescale, genetically targeted optical control of neural activity," *Nat. Neurosci.*, vol. 8, no. 9, pp. 1263–1268, 2005.

[154] E. S. Boyden, "A history of optogenetics: the development of tools for controlling brain circuits with light," *F1000 Biol. Rep.*, vol. 3, p. 11, 2011.

[155] C. Cosentino *et al.*, "Engineering of a light-gated potassium channel," *Science (80-.).*, vol. 348, no. 6235, pp. 707–710, May 2015.

[156] V. Gradinaru, K. R. Thompson, and K. Deisseroth, "eNpHR: A Natronomonas halorhodopsin enhanced for optogenetic applications," *Brain Cell Biol.*, vol. 36, no. 1–4,

pp. 129–139, Aug. 2008.

[157] J. Y. Lin, P. M. Knutsen, A. Muller, D. Kleinfeld, and R. Y. Tsien, "ReaChR: A red-shifted variant of channelrhodopsin enables deep transcranial optogenetic excitation," *Nat. Neurosci.*, vol. 16, no. 10, pp. 1499–1508, Oct. 2013.

[158] F. Zhang *et al.*, "Red-shifted optogenetic excitation: a tool for fast neural control derived from Volvox carteri," *Nat. Neurosci.*, vol. 11, no. 6, pp. 631–633, 2008.

[159] C. N. Bedbrook, K. K. Yang, J. E. Robinson, E. D. Mackey, V. Gradinaru, and F. H. Arnold, "Machine learning-guided channelrhodopsin engineering enables minimally invasive optogenetics," *Nat. Methods*, vol. 16, no. 11, pp. 1176–1184, Nov. 2019.

[160] O. Yizhar, L. E. Fenno, T. J. Davidson, M. Mogri, and K. Deisseroth, "Optogenetics in Neural Systems," *Neuron*, vol. 71, pp. 9–34, 2011.

[161] G. Nagel *et al.*, "Channelrhodopsin-2, a directly light-gated cation-selective membrane channel," *Proc. Natl. Acad. Sci. U. S. A.*, vol. 100, no. SUPPL. 2, pp. 13940–13945, Nov. 2003.

[162] A. Berndt, S. Y. Lee, C. Ramakrishnan, and K. Deisseroth, "Structure-guided transformation of channelrhodopsin into a light-activated chloride channel," *Science (80-.).*, vol. 344, no. 6182, pp. 420–424, 2014.

[163] J. Wietek *et al.*, "Conversion of channelrhodopsin into a light-gated chloride channel," *Science (80-.).*, vol. 344, no. 6182, pp. 409–412, 2014.

[164] E. G. Govorunova, O. A. Sineshchekov, R. Janz, X. Liu, and J. L. Spudich, "Natural light-gated anion channels: A family of microbial rhodopsins for advanced optogenetics," *Science (80-.).*, vol. 349, no. 6248, pp. 647–650, 2015.

[165] A. Forli *et al.*, "Two-Photon Bidirectional Control and Imaging of Neuronal Excitability with High Spatial Resolution In Vivo," *Cell Rep.*, vol. 22, no. 11, pp. 2809–2817, 2018.

[166] A. R. Mardinly *et al.*, "Precise multimodal optical control of neural ensemble activity," *Nat. Neurosci.*, vol. 21, no. 6, pp. 881–893, Jun. 2018.

[167] F. Zhang *et al.*, "Multimodal fast optical interrogation of neural circuitry," *Nature*, vol. 446, no. 7136, pp. 633–639, Apr. 2007.

[168] B. Y. Chow *et al.*, "High-performance genetically targetable optical neural silencing by light-driven proton pumps," *Nature*, vol. 463, no. 7277, pp. 98–102, Jan. 2010.

[169] X. Han *et al.*, "A High-Light Sensitivity Optical Neural Silencer: Development and Application to Optogenetic Control of Non-Human Primate Cortex," *Front. Syst. Neurosci.*, vol. 5, 2011.

[170] K. Deisseroth, "Optogenetics: 10 years of microbial opsins in neuroscience," *Nature Neuroscience*, vol. 18, no. 9. Nature Publishing Group, pp. 1213–1225, 26-Aug-2015.

[171] C. K. Kim, A. Adhikari, and K. Deisseroth, "Integration of optogenetics with

complementary methodologies in systems neuroscience," *Nature Reviews Neuroscience*, vol. 18, no. 4. Nature Publishing Group, pp. 222–235, 01-Apr-2017.

[172] P. Zhu, O. Fajardo, J. Shum, Y. P. Zhang Schärer, and R. W. Friedrich, "High-resolution optical control of spatiotemporal neuronal activity patterns in zebrafish using a digital micromirror device.," *Nat. Protoc.*, vol. 7, no. 7, pp. 1410–1425, 2012.

[173] A. W. Lohmann and D. P. Paris, "Binary Fraunhofer Holograms, Generated by Computer," *Appl. Opt.*, vol. 6, no. 10, p. 1739, Oct. 1967.

[174] V. Emiliani, A. E. Cohen, K. Deisseroth, and M. Häusser, "All-optical interrogation of neural circuits," *Journal of Neuroscience*, vol. 35, no. 41. Society for Neuroscience, pp. 13917–13926, 14-Oct-2015.

[175] E. Ronzitti, C. Ventalon, M. Canepari, B. C. Forget, E. Papagiakoumou, and V. Emiliani, "Recent advances in patterned photostimulation for optogenetics," *Journal of Optics (United Kingdom)*, vol. 19, no. 11. Institute of Physics Publishing, 12-Oct-2017.

[176] N. C. Pégard, A. R. Mardinly, I. A. Oldenburg, S. Sridharan, L. Waller, and H. Adesnik, "Three-dimensional scanless holographic optogenetics with temporal focusing (3D-SHOT)," *Nat. Commun.*, vol. 8, no. 1, Dec. 2017.

[177] L. Carrillo-reid *et al.*, "Controlling Visually Guided Behavior by Holographic Recalling of Cortical Ensembles Article Controlling Visually Guided Behavior by Holographic Recalling of Cortical Ensembles," *Cell*, pp. 1–11, 2019.

[178] Y. El-Shamayleh, A. M. Ni, and G. D. Horwitz, "Strategies for targeting primate neural circuits with viral vectors," *J. Neurophysiol.*, vol. 116, no. 1, pp. 122–134, Jul. 2016.

[179] C. S. Branda and S. M. Dymecki, "Talking about a revolution: The impact of site-specific recombinases on genetic analyses in mice," *Developmental Cell*, vol. 6, no. 1. pp. 7–28, Jan-2004.

[180] C. R. Gerfen, R. Paletzki, and N. Heintz, "GENSAT BAC cre-recombinase driver lines to study the functional organization of cerebral cortical and basal ganglia circuits," *Neuron*, vol. 80, no. 6, pp. 1368–1383, Dec. 2013.

[181] S. Gong *et al.*, "Targeting Cre recombinase to specific neuron populations with bacterial artificial chromosome constructs," *Journal of Neuroscience*, vol. 27, no. 37. pp. 9817–9823, 12-Sep-2007.

[182] J. A. Harris *et al.*, "Anatomical characterization of Cre driver mice for neural circuit mapping and manipulation," *Front. Neural Circuits*, vol. 8, Jul. 2014.

[183] L. Madisen *et al.*, "A robust and high-throughput Cre reporting and characterization system for the whole mouse brain," *Nat. Neurosci.*, vol. 13, no. 1, pp. 133–140, Jan. 2010.

[184] H. Taniguchi *et al.*, "A Resource of Cre Driver Lines for Genetic Targeting of GABAergic

Neurons in Cerebral Cortex," *Neuron*, vol. 71, no. 6, pp. 995–1013, Sep. 2011.

[185] J. A. Harris *et al.*, "Hierarchical organization of cortical and thalamic connectivity.," *Nature*, no. April 2018, 2019.

[186] L. M. Carey, G. Lamp, and M. Turville, "The State-of-the-Science on Somatosensory Function and Its Impact on Daily Life in Adults and Older Adults, and Following Stroke," *OTJR Occup. Particip. Heal.*, vol. 36, no. 2_suppl, pp. 27S-41S, Apr. 2016.

[187] E. A. Lumpkin and D. M. Bautista, "Feeling the pressure in mammalian somatosensation," *Current Opinion in Neurobiology*, vol. 15, no. 4. pp. 382–388, Aug-2005.

[188] E. G. Reed-Geaghan and S. M. Maricich, "Peripheral somatosensation: A touch of genetics," *Current Opinion in Genetics and Development*, vol. 21, no. 3. pp. 240–248, Jun-2011.

[189] S. Taylor *et al.*, "Does somatosensation change with age in children and adolescents? A systematic review," *Child: Care, Health and Development*, vol. 42, no. 6. Blackwell Publishing Ltd, pp. 809–824, 01-Nov-2016.

[190] A. L. Oaklander and S. M. Siegel, "Cutaneous innervation: Form and function," *Journal of the American Academy of Dermatology*, vol. 53, no. 6. pp. 1027–1037, Dec-2005.

[191] P. Delmas, J. Hao, and L. Rodat-Despoix, "Molecular mechanisms of mechanotransduction in mammalian sensory neurons," *Nature Reviews Neuroscience*, vol. 12, no. 3. pp. 139–153, Mar-2011.

[192] E. A. Lumpkin, K. L. Marshall, and A. M. Nelson, "The cell biology of touch," *Journal of Cell Biology*, vol. 191, no. 2. pp. 237–248, 18-Oct-2010.

[193] M. E. Diamond, M. Von Heimendahl, P. M. Knutsen, D. Kleinfeld, and E. Ahissar, "'Where' and 'what' in the whisker sensorimotor system," *Nat. Rev. Neurosci.*, vol. 9, no. 8, pp. 601–612, 2008.

[194] R. V. Rikhye, R. D. Wimmer, and M. M. Halassa, "Toward an Integrative Theory of Thalamic Function," *Annu. Rev. Neurosci.*, vol. 41, no. 1, pp. 163–183, Jul. 2018.

[195] D. Feldmeyer *et al.*, "Barrel cortex function," *Progress in Neurobiology*, vol. 103. pp. 3–27, Apr-2013.

[196] E. Welker and H. Van der Loos, "Quantitative correlation between barrel-field size and the sensory innervation of the whiskerpad: A comparative study in six strains of mice bred for different patterns of mystacial vibrissae," *J. Neurosci.*, vol. 6, no. 11, pp. 3355–3373, 1986.

[197] P. M. Knutsen and E. Ahissar, "Orthogonal coding of object location," *Trends in Neurosciences*, vol. 32, no. 2. Elsevier Ltd, pp. 101–109, 2009.

[198] N. Nikbakht, A. Tafreshiha, D. Zoccolan, and M. E. Diamond, "Supralinear and Supramodal Integration of Visual and Tactile Signals in Rats: Psychophysics and Neuronal

Mechanisms," *Neuron*, vol. 97, no. 3, pp. 626-639.e8, Feb. 2018.

[199] R. M. Bruno, V. Khatri, P. W. Land, and D. J. Simons, "Thalamocortical Angular Tuning Domains within Individual Barrels of Rat Somatosensory Cortex," *J. Neurosci.*, vol. 23, no. 29, pp. 9565–9574, Oct. 2003.

[200] C. C. H. Petersen, "The functional organization of the barrel cortex," *Neuron*, vol. 56, no. 2. pp. 339–355, 2007.

[201] M. T. Shipley, "Response characteristics of single units in the rat's trigeminal nuclei to vibrissa displacements," *J. Neurophysiol.*, vol. 37, no. 1, pp. 73–90, 1974.

[202] M. C. Stüttgen, J. Rüter, and C. Schwarz, "Two psychophysical channels of whisker deflection in rats align with two neuronal classes of primary afferents," *J. Neurosci.*, vol. 26, no. 30, pp. 7933–7941, Jul. 2006.

[203] S. Temereanca and D. J. Simons, "Local Field Potentials and the Encoding of Whisker Deflections by Population Firing Synchrony in Thalamic Barreloids," *J. Neurophysiol.*, vol. 89, no. 4, pp. 2137–2145, Apr. 2003.

[204] E. Zucker and W. I. Welker, "Coding of somatic sensory input by vibrissae neurons in the rat's trigeminal ganglion," *Brain Res.*, vol. 12, no. 1, pp. 138–156, 1969.

[205] M. E. Diamond and E. Arabzadeh, "Whisker sensory system - From receptor to decision," *Progress in Neurobiology*, vol. 103. pp. 28–40, Apr-2013.

[206] M. R. Bale and R. S. Petersen, "Transformation in the Neural Code for Whisker Deflection Direction Along the Lemniscal Pathway," *J. Neurophysiol.*, vol. 102, no. 5, pp. 2771–2780, Nov. 2009.

[207] C. C. H. Petersen, "The barrel cortex - Integrating molecular, cellular and systems physiology," *Pflugers Archiv European Journal of Physiology*, vol. 447, no. 2. pp. 126–134, Nov-2003.

[208] P. M. Ma, "The barrelettes?architectonic vibrissal representations in the brainstem trigeminal complex of the mouse. Normal structural organization," *J. Comp. Neurol.*, vol. 309, no. 2, pp. 161–199, Jul. 1991.

[209] R. S. Petersen, S. Panzeri, and M. Maravall, "Neural coding and contextual influences in the whisker system," *Biological Cybernetics*, vol. 100, no. 6. pp. 427–446, Jun-2009.

[210] J. Fernández-Montoya, C. Avendaño, and P. Negredo, "The Glutamatergic System in Primary Somatosensory Neurons and Its Involvement in Sensory Input-Dependent Plasticity," *Int. J. Mol. Sci.*, vol. 19, no. 69, 2018.

[211] K. Sehara and H. Kawasaki, "Neuronal circuits with whisker-related patterns," *Mol. Neurobiol.*, vol. 43, no. 3, pp. 155–162, 2011.

[212] S. Haidarliu and E. Ahissar, "Size Gradients of Barreloids," *J. Comp. Neurol.*, vol. 387, no.

September 2000, pp. 372–387, 2001.

[213] S. M. Sherman, “The thalamus is more than just a relay,” *Current Opinion in Neurobiology*, vol. 17, no. 4. pp. 417–422, Aug-2007.

[214] H. Van Der Loos, “Barreloids in mouse somatosensory thalamus,” *Neurosci. Lett.*, vol. 2, no. 1, pp. 1–6, 1976.

[215] M. Ito, “Response properties and topography of vibrissa-sensitive VPM neurons in the rat,” *J. Neurophysiol.*, vol. 60, no. 4, pp. 1181–1197, 1988.

[216] E. Timofeeva, C. Mérette, C. Émond, P. Lavallée, and M. Deschênes, “A Map of Angular Tuning Preference in Thalamic Barreloids,” *J. Neurosci.*, vol. 23, no. 33, pp. 10717–10723, Nov. 2003.

[217] T. Pierret, P. Lavallee, and M. Deschenes, “Parallel streams for the relay of vibrissal information through thalamic barreloids,” *J. Neurosci.*, vol. 20, no. 19, pp. 7455–7462, Oct. 2000.

[218] J. A. Lü bke Dirk Feldmeyer, “Excitatory signal flow and connectivity in a cortical column: focus on barrel cortex,” *Brain Struct. Funct.*, vol. 212, no. 1, pp. 3–17, 2007.

[219] T. Mao, D. Kusefoglu, B. M. Hooks, D. Huber, L. Petreanu, and K. Svoboda, “Long-Range Neuronal Circuits Underlying the Interaction between Sensory and Motor Cortex,” *Neuron*, vol. 72, no. 1, pp. 111–123, Oct. 2011.

[220] C. Watson, G. Paxinos, and L. Puelles, *The Mouse Nervous System*. 2011.

[221] D. Pinault, *The thalamic reticular nucleus : structure , function and concept*, vol. 46. 2004.

[222] F. Crick, “Function of the thalamic reticular complex : The searchlight hypothesis Neurobiology : Crick,” vol. 81, no. July, pp. 4586–4590, 1984.

[223] S. M. Sherman and R. W. Guillery, “On the actions that one nerve cell can have on another: Distinguishing ‘“drivers”’ from ‘ “modulators,”’” 1998.

[224] M. E. Bickford, W. Martin Usrey, L. Acsady, and H. Joseph Alitto, “Thalamic Circuit Diversity: Modulation of the Driver/Modulator Framework,” *Front. Neural Circuits*, vol. 9, 2016.

[225] S. R. Crandall, S. J. Cruikshank, and B. W. Connors, “A Corticothalamic Switch: Controlling the Thalamus with Dynamic Synapses,” *Neuron*, vol. 86, no. 3, pp. 768–782, 2015.

[226] C. Varela, “Thalamic neuromodulation and its implications for executive networks,” *Front. Neural Circuits*, vol. 8, no. June, pp. 1–22, 2014.

[227] S. M. Sherman, “Tonic and burst firing: dual modes of thalamocortical relay.,” *Trends Neurosci.*, vol. 24, no. 2, pp. 122–6, 2001.

[228] M. Steriade, D. A. Mccormick, and T. J. Sejnowski, “Thalamocortical Oscillations in the Sleeping and Aroused Brain,” *Science (80-.).*, vol. 262, 1993.

[229] S. Murray Sherman, “Tonic and burst firing: Dual modes of thalamocortical relay,” *Trends in Neurosciences*, vol. 24, no. 2. Elsevier Ltd, pp. 122–126, 01-Feb-2001.

[230] N. A. Lesica and G. B. Stanley, “Encoding of Natural Scene Movies by Tonic and Burst Spikes in the Lateral Geniculate Nucleus,” 2004.

[231] S. M. Sherman and R. W. Guillery, *Functional Connections of Cortical Areas*. 2013.

[232] C. Varga, A. Sík, P. Lavallé, and M. Deschê, “Dendroarchitecture of Relay Cells in Thalamic Barreloids: A Substrate for Cross-Whisker Modulation,” *J. Neurosci.*, vol. 22, no. 14, pp. 6186–6194, 2002.

[233] B. Lé, D. Desıˆlets-Roy, C. Varga, P. Lavallé, and M. Deschê, “Substrate for Cross-Talk Inhibition between Thalamic Barreloids,” *J. Neurosci.*, vol. 22, 2002.

[234] T. Furuta, T. Kaneko, and M. Deschenes, “Septal Neurons in Barrel Cortex Derive Their Receptive Field Input from the Lemniscal Pathway,” *J. Neurosci.*, vol. 29, no. 13, pp. 4089–4095, 2009.

[235] J. F. A. Poulet, L. M. J. Fernandez, S. Crochet, and C. C. H. Petersen, “Thalamic control of cortical states,” *Nat. Neurosci.*, vol. 15, no. 3, pp. 370–372, 2012.

[236] S. Temereanca and D. J. Simons, “Functional Topography of Corticothalamic Feedback Enhances Thalamic Spatial Response Tuning in the Somatosensory Whisker/Barrel System,” *Neuron*, vol. 41, no. 4, pp. 639–651, Feb. 2004.

[237] L. Li and F. F. Ebner, “Cortical Modulation of Spatial and Angular Tuning Maps in the Rat Thalamus,” *J. Neurosci.*, vol. 27, no. 1, pp. 167–179, 2007.

[238] N. Urbain, P. A. Salin, P. A. Libourel, J. C. Comte, L. J. Gentet, and C. C. H. Petersen, “Whisking-Related Changes in Neuronal Firing and Membrane Potential Dynamics in the Somatosensory Thalamus of Awake Mice,” *Cell Rep.*, vol. 13, no. 4, pp. 647–656, 2015.

[239] C. Yu, D. Derdikman, S. Haidarliu, and E. Ahissar, “Parallel Thalamic Pathways for Whisking and Touch Signals in the Rat,” *PLoS Biol.*, vol. 4, no. 5, 2006.

[240] J. D. Moore, N. M. Lindsay, M. Deschênes, and D. Kleinfeld, “Vibrissa Self-Motion and Touch Are Reliably Encoded along the Same Somatosensory Pathway from Brainstem through Thalamus,” *PLoS Biol.*, vol. 13, no. 9, 2015.

[241] N. Urbain and M. Deschenes, “A New Thalamic Pathway of Vibrissal Information Modulated by the Motor Cortex,” *J. Neurosci.*, vol. 27, no. 45, pp. 12407–12412, 2007.

[242] B. Sakmann and R. M. Bruno, “Cortex Is Driven by Weak but Synchronously Active Thalamocortical Synapses,” *Science (80-.).*, vol. 312, no. 5780, pp. 1622–1627, 2006.

[243] R. S. Petersen *et al.*, “Diverse and Temporally Precise Kinetic Feature Selectivity in the VPm Thalamic Nucleus,” *Neuron*, vol. 60, no. 5, pp. 890–903, 2008.

[244] M. R. Bale, R. A. A. Ince, G. Santagata, and R. S. Petersen, “Efficient population coding of

naturalistic whisker motion in the ventro-posterior medial thalamus based on precise spike timing," *Front. Neural Circuits*, vol. 9, no. September, pp. 1–14, 2015.

[245] *Optics Studio Manual*. 2017.

[246] A. Schaap and Y. Bellouard, "Molding topologically-complex 3D polymer microstructures from femtosecond laser machined glass," *Opt. Mater. Express*, vol. 3, no. 9, pp. 1428–1437, 2013.

[247] A. Antonini, C. Liberale, and T. Fellin, "Fluorescent layers for characterization of sectioning microscopy with coverslip- uncorrected and water immersion objectives," vol. 22, no. 12, pp. 14293–14304, 2014.

[248] E. A. Mukamel, A. Nimmerjahn, and M. J. Schnitzer, "Automated Analysis of Cellular Signals from Large-Scale Calcium Imaging Data," *Neuron*, vol. 63, no. 6, pp. 747–760, Sep. 2009.

[249] E. A. Pnevmatikakis and A. Giovannucci, "NoRMCorre: An online algorithm for piecewise rigid motion correction of calcium imaging data," *J. Neurosci. Methods*, vol. 291, pp. 83–94, Nov. 2017.

[250] E. A. Pnevmatikakis *et al.*, "Simultaneous Denoising, Deconvolution, and Demixing of Calcium Imaging Data," *Neuron*, vol. 89, no. 2, p. 285, 2016.

[251] J. M. P. Pakan *et al.*, "Behavioral-state modulation of inhibition is context-dependent and cell type specific in mouse visual cortex," *Elife*, vol. 5, no. AUGUST, Aug. 2016.

[252] C. Magri, K. Whittingstall, V. Singh, N. K. Logothetis, and S. Panzeri, "A toolbox for the fast information analysis of multiple-site LFP, EEG and spike train recordings," *BMC Neurosci.*, vol. 10, no. 1, p. 81, 2009.

[253] D. Keller, C. Erö, and H. Markram, "Cell Densities in the Mouse Brain: A Systematic Review," *Front. Neuroanat.*, vol. 12, no. October, 2018.

[254] J. Friedrich, P. Zhou, and L. Paninski, "Fast online deconvolution of calcium imaging data," pp. 1–26, 2017.

[255] T. Gissibl, S. Thiele, A. Herkommer, and H. Giessen, "Two-photon direct laser writing of ultracompact multi-lens objectives," *Nat. Photonics*, vol. 10, pp. 554–560, 2016.

[256] A. Antonini, C. Liberale, and T. Fellin, "Fluorescent layers for characterization of sectioning microscopy with coverslip-uncorrected and water immersion objectives," *Opt. Express*, vol. 22, no. 12, pp. 14293–14304, 2014.

[257] R. P. J. Barretto and M. J. Schnitzer, "In vivo microendoscopy of the hippocampus," *Cold Spring Harb. Protoc.*, vol. 7, no. 10, pp. 1092–1099, 2012.

[258] J. H. Marshel, A. P. Kaye, I. Nauhaus, and E. M. Callaway, "Anterior-Posterior Direction Opponency in the Superficial Mouse Lateral Geniculate Nucleus," *Neuron*, vol. 76, no. 4,

pp. 713–720, 2012.

[259] V. Martin, B.-B. Renata, K. Ulf, and C. Jessica A, “Arousal and locomotion make distinct contributions to cortical activity patterns and visual encoding,” *Neuron*, vol. 86, no. 3, pp. 740–754, 2015.

[260] Y. Ziv *et al.*, “Long-term dynamics of CA1 hippocampal place codes,” *Nat. Neurosci.*, vol. 16, no. 3, pp. 264–266, Mar. 2013.

[261] S. L. Resendez *et al.*, “Visualization of cortical , subcortical and deep brain neural circuit dynamics during naturalistic mammalian behavior with head-mounted microscopes and chronically implanted lenses,” *Nat. Protoc.*, vol. 11, no. 3, pp. 566–597, 2016.

[262] J. Nicholas Betley *et al.*, “Neurons for hunger and thirst transmit a negative-valence teaching signal.”

[263] J. Lecoq *et al.*, “Visualizing mammalian brain area interactions by dual-axis two-photon calcium imaging,” *Nat. Publ. Gr.*, 2014.

[264] W. M. Lee and S. H. Yun, “Adaptive aberration correction of GRIN lenses for confocal endomicroscopy,” *Opt. Lett.*, vol. 36, no. 23, p. 4608, 2011.

[265] C. Wang and N. Ji, “Pupil-segmentation-based adaptive optical correction of a high-numerical-aperture gradient refractive index lens for two-photon fluorescence endoscopy,” *Opt. Lett.*, vol. 37, no. 11, p. 2001, 2012.

[266] G. Matz, H. Messerschmidt, and H. Gross, “Improved chromatical and field correction of high-NA GRIN-based endomicroscopic imaging systems for new biophotonics applications,” *Proc. SPIE*, vol. 9304, p. 93041E, 2015.

[267] C. Moretti, A. Antonini, S. Bovetti, C. Liberale, and T. Fellin, “Scanless functional imaging of hippocampal networks using patterned two-photon illumination through GRIN lenses,” *Biomed. Opt. Express*, vol. 7, no. 10, pp. 3958–3967, 2016.

[268] J. P. Rickgauer and D. W. Tank, “Two-photon excitation of channelrhodopsin-2 at saturation,” *Proc. Natl. Acad. Sci. U. S. A.*, vol. 106, no. 35, pp. 15025–15030, Sep. 2009.

[269] E. Papagiakoumou *et al.*, “Scanless two-photon excitation of channelrhodopsin-2,” *Nat. Methods*, vol. 7, no. 10, pp. 848–854, Oct. 2010.

[270] A. M. Packer, D. S. Peterka, J. J. Hirtz, R. Prakash, K. Deisseroth, and R. Yuste, “Two-photon optogenetics of dendritic spines and neural circuits,” *Nat. Methods*, vol. 9, no. 12, pp. 1202–1205, Dec. 2012.

[271] A. M. Packer, L. E. Russell, H. W. P. Dalgleish, and M. Häusser, “Simultaneous all-optical manipulation and recording of neural circuit activity with cellular resolution in vivo,” *Nat. Methods*, vol. 12, no. 2, pp. 140–146, 2015.

[272] J. P. Rickgauer, K. Deisseroth, and D. W. Tank, “Simultaneous cellular-resolution optical

perturbation and imaging of place cell firing fields," *Nat. Neurosci.*, vol. 17, no. 12, pp. 1816–1824, Jan. 2014.

[273] L. Carrillo-Reid, W. Yang, Y. Bando, D. S. Peterka, and R. Yuste, "Imprinting and recalling cortical ensembles," *Science (80-.).*, vol. 353, no. 6300, pp. 691–694, Aug. 2016.

[274] D. M. Huland *et al.*, "In vivo imaging of unstained tissues using long gradient index lens multiphoton endoscopic systems," *Biomed. Opt. Express*, vol. 3, no. 5, p. 1077, May 2012.

[275] D. M. Huland *et al.*, "Multiphoton gradient index endoscopy for evaluation of diseased human prostatic tissue ex vivo," *J. Biomed. Opt.*, vol. 19, no. 11, p. 116011, Nov. 2014.

[276] B. Li, W. Piyawattanametha, and Z. Qiu, "Metalens-based miniaturized optical systems," *Micromachines*, vol. 10, no. 5, 2019.

[277] H. Pahlevaninezhad *et al.*, "Nano-optic endoscope for high-resolution optical coherence tomography in vivo," *Nat. Photonics*, vol. 12, pp. 540–547, 2018.

[278] W. Zong *et al.*, "Fast high-resolution miniature two-photon microscopy for brain imaging in freely behaving mice," *Nat. Publ. Gr.*, vol. 14, no. 7, 2017.

Author contribution

This thesis is the result of a joint effort from a team of scientists, including: Andrea Antonini, Vijayakumar P. Rajamanickam, Andrea Bertoncini, Carlo Liberale for corrective lens design and fabrication; Serena Bovetti and Claudio Moretti for hippocampal imaging experiments and analysis; Francesca Succol for surgeries and analysis of confocal images; Monica Moroni and Stefano Panzeri for analysis of thalamic recording and simulation of calcium data. My personal contribution in this project regarded the fabrication of eFOV microendoscopes, their optical characterization, their validation for in vivo functional imaging, and their application to study the physiology of VPM neurons in awake mice.

Acknowledgements

I would like to express my gratitude to my supervisor Tommaso Fellin, who showed to be a true example in the field of academic research. He had the right answers and words in every situation. Thank Tom for giving me the chance of growing, both personally and scientifically, with productive discussions and fruitful suggestions.

Also, I would like to thank all the past and present laboratory members, for their extremely cooperative attitude, their helpful teachings and constructive talks. They were able to create a highly interdisciplinary, competent and intellectually sparkling atmosphere.

Of course, I thank all the people who collaborated with me on the eFOV-microendoscopes project, and in particular Serena, who introduced me to mice, Monica, Claudio, Andrea, Francesca, Angelo and Carlo.

Thank to the IIT for providing researchers with good structures and creating a scientifically variegated environment, thus giving the opportunity to work efficiently and to know many people with different backgrounds. Thank to my Venetian roommate Zambo for bearing with me and last but not least, many thanks to my family, who always supported me throughout these years.